ABSTRACT

Title of dissertation: Development and Application of Mach 10 PIV in a Large Scale Wind Tunnel

Jonathan Brooks, Doctor of Philosophy, 2018

Dissertation directed by: Professor Ashwani K. Gupta
Department of Mechanical Engineering

This dissertation presents the development of particle image velocimetry (PIV) for use in a large-scale hypersonic wind tunnel to measure the turbulent boundary layer (TBL) and shock turbulent boundary layer interaction (STBLI) on a large hollow cylinder flare (HCF) test article. The main feature of this application of PIV is the novel local injector which injects seeding particles into the high-speed section of the flow. Development work began sub-scale in a Mach 3 wind tunnel where the seeding particle response was characterized and the local injectors were demonstrated. Once the measurement technique was refined, it was scaled up to hypersonic flow.

The particle response was characterized through PIV measurements of Mach 3 TBLs under low Reynolds number conditions, $Re_\tau = 200{-}1,000$. Effects of Reynolds number, particle response and boundary layer thickness were evaluated separately from facility specific experimental apparatus or methods. Prior to the

current study, no detailed experimental study characterizing the effect of Stokes number on attenuating wall normal fluctuating velocities has been performed. Also, particle lag and spatial resolution are shown to act as low pass filters on the fluctuating velocity power spectral densities which limit the measurable energy content.

High-speed local seeding particle injection has been demonstrated successfully for the first time. Prior to these measurements, PIV applications have employed global seeding or local seeding in the subsonic portion of the nozzle. The high-speed local seeding injectors accelerate the particle aerosol through a converging/diverging supersonic nozzle which exits tangentially to the wall. Two methods are used to measure the particle concentration which shows good agreement to the CFD particle tracking codes used to design the injector nozzle profiles. Based on the particle concentration distribution in the boundary layer a new phenomenon of particle biasing has been identified and characterized.

PIV measurements of a Mach 10 TBL and STBLI have been performed on a large (2.4-m long, 0.23-m dia.) HCF at a freestream unit Reynolds number of 16 million per meter. These are the highest Mach number PIV measurements reported in the literature. Particles are locally injected from the leading edge of the test article and turbulent mixing dispersed the particles for a relatively uniform high concentration of particles at the measurement section 1.83-m downstream of the leading edge. The van Driest transformed mean velocity in the TBL agrees well with incompressible zero pressure gradient log law theory. Morkovin-scaled streamwise velocity fluctuations agree well with the literature for the majority of the boundary layer.

Development and Application of Mach 10 PIV in a Large Scale Wind Tunnel

by

Jonathan Brooks

Dissertation submitted to the Faculty of the Graduate School of the
University of Maryland, College Park in partial fulfillment
of the requirements for the degree of
Doctor of Philosophy
2018

Advisory Committee:
Professor Ashwani K. Gupta, Advisor
Professor Kenneth Yu, Dean Representative
Dr. Eric Marineau, Office of Naval Research
Professor Mark Lewis
Professor M. Pino Martin
Professor Bao Yang

Dedicated to the women in my life

The unwavering and unconditional love of

my mom, Rita,

my aunt, Becky,

my sister, Michelle,

and my fiancé, Camilla

has carried me.

Acknowledgments

This dissertation would not have been possible without the help and assistance of many people. First, I would like to acknowledge Dr. Michael Kendra who managed the Air Force Office of Scientific Research grant which funded this research. Dr. Kendra not only provided financial support but also great personal interest in my research.

Of course, I must thank my advisors Prof. Ashwani Gupta and Dr. Eric Marineau. Although Dr. Marineau may officially be considered as the sponsor, he quickly became an irreplaceable technical advisor. I have heavily relied upon his insights, suggestions and experience throughout my PhD research.

The professors involved in the Center of Testing Excellence (CoTE) collaboration between the University of Maryland and Arnold Engineering Development Complex (AEDC) White Oak have given excellent insights and questions which have strengthened my research. In particular, Prof. Pino Martin and her PhD student, Clara Helm, have provided me with wonderful discussions on theory, much appreciated comparison data from her DNS and LES, and design recommendations on the hollow cylinder flare test article (HCF). Likewise, Prof. Stuart Laurence and his PhD student William Starshak have also provided design recommendations for the HCF. Prof. Kenneth Yu is the foundation of the CoTE program and as such has given me incredible support and has shown great interest in my research.

Michael Smith has helped me with every optical system I used in the course of my research. Beyond advice, he was often the physical force to make the optical

setups possible. He has also provided well-appreciated advice on racing and ballroom dancing.

Dr. Ahmed Khalil has been a rock in my journey through gradate school. A service too immense to repay or thank him enough for.

I would like to acknowledge everyone at AEDC White Oak. I believe every single employee has helped me along the way and without hesitation when asked. I would like to especially acknowledge Dan Marren, John Lafferty and Joe Coblish for all the technical advice and discussions, Will Vodra for mechanical support in the HCF design as well as convincing the manufacture to build the test article correctly, and Inna Kurits for volunteering as the project engineer for the unblemished HCF test entry in Tunnel 9.

The AEDC White Oak operations team have gone above and beyond in order to get the Mach 10 test to happen for the HCF. Rob Hale in particular has made many things reality which I was beginning to assume to be impossible.

I also acknowledge Prof. Nick Parziale who has provided brilliant insight into my experiments.

Finally, I would like to acknowledge Jack Draper. His friendship and advice with Matlab and LaTeX has prevented me from throwing my computer out of the non-existent window in our basement office.

Table of Contents

List of Tables vii

List of Figures viii

Nomenclature x

1 Introduction 1

2 Background and Theory 10
2.1 Hypersonic and Local Seeding Literature Review . . . 10
2.2 Analysis Theory . . . 13
2.2.1 Turbulent Boundary Layer Theory . . . 14
2.2.2 Boundary Layer Thickness . . . 17
2.2.3 Skin friction velocity . . . 20
2.2.4 Morkovin's Hypothesis . . . 22
2.2.5 Large Scale Turbulent Structures . . . 23
2.2.6 Power Spectral Density . . . 24
2.2.7 Measurement Uncertainties . . . 24

3 Experimental Setup 27
3.1 Mach 3 Wind Tunnel Facility (M3CT) . . . 27
3.2 M3CT Additions . . . 30
3.2.1 Pitot Probe . . . 32
3.2.2 Pitot Rake . . . 33
3.2.3 Oblique Shock Diffuser . . . 37
3.3 Tunnel 9 . . . 41
3.4 Hollow Cylinder Flare Test Article . . . 43
3.5 PIV setup . . . 46
3.5.1 Optics, Laser and Post Processing . . . 46
3.5.2 M3CT . . . 48
3.5.3 Tunnel 9 . . . 50
3.6 Wall Reflection Mitigation . . . 50

4 PIV Particles and Injection Methods 53
4.1 Particle Material and Generation . . . 53
4.2 High-Speed Local Injectors . . . 55
4.2.1 M3CT . . . 57
4.2.2 Tunnel 9 . . . 60
4.3 Particle Response . . . 64
4.4 Particle Concentration . . . 72

5 Mach 3 Reduced Reynolds Number Experiments 79
5.1 Mean Velocity . . . 79
5.2 Spatial Resolution . . . 82
5.2.1 Vector Processing . . . 83
5.2.2 Magnification . . . 84
5.3 Velocity Fluctuations and Reynolds Shear Stress . . . 85
5.3.1 Streamwise Fluctuating Velocity . . . 86
5.3.2 Wall Normal Fluctuating Velocity . . . 90
5.3.3 Reynolds Shear Stress . . . 93
5.4 Spectral Density and Analysis of Large Scale Motion Structures . . . 96

6 Characterization of Local Injection 102
6.1 Concentration . . . 102
6.2 Mean Velocity and Turbulence Statistics . . . 104
6.2.1 Mean Velocity . . . 104
6.2.2 Turbulence Statistics . . . 108
6.3 Impact of Local Injection . . . 112
6.4 Particle Biasing . . . 114

7 Mach 10 PIV 121
7.1 Injector Modifications . . . 121
7.2 HCF Movement . . . 124
7.3 Particle Concentration . . . 127
7.4 Turbulent Boundary Layer . . . 128
7.4.1 Mean Streamwise Fluctuating Velocity . . . 129
7.4.2 Large Scale Motion Structure Angle . . . 130
7.5 Shock Turbulent Boundary Layer Interaction . . . 131

8 Conclusions 135

9 Recommended Future Studies 139

10 Publications 145
10.1 Journal Articles . . . 145
10.2 Conference Papers . . . 145

Bibliography 147

List of Tables

2.1 PIV uncertainty for at $y/\delta = 0.5$ 26

3.1 Orifice plate reservoir conditions 29
3.2 M3CT reduced Reynolds number flow conditions 31
3.3 Oblique shock diffuser dimensions 40
3.4 AEDC tunnel 9 nominal flow conditions 42

5.1 M3CT literature comparison 87

6.1 Local injection PIV flow conditions 103
6.2 Key parameters from comparison literature data 109

7.1 Tunnel 9 literature comparison 130

List of Figures

1.1 Literature differences in u' profile 7

3.1 Schematic of M3CT test section 28
3.2 Single Pitot probe installed in Station 2 34
3.3 Single Pitot probe Mach number profiles, M3CT 34
3.4 Pitot probe inner scaled van Driest transformed velocity 35
3.5 Pitot rake CAD representation 35
3.6 Pitot rake analysis GUI 36
3.7 Oblique shock diffuser model 39
3.8 Matlab schematic of oblique shock diffuser 41
3.9 Photograph and Schematic of Tunnel 9 Test Facility 43
3.10 Photograph of HCF in Tunnel 9 Test Section 44
3.11 Morkovin scaled turbulence statistics comparing cameras 48
3.12 M3CT PIV setup 49
3.13 Tunnel 9 PIV setup 51

4.1 Clausius-Clapeyron plot for seeding oils 54
4.2 M3CT local seeding injector 57
4.3 Initial Global Non-Uniform Seeding 58
4.4 M3CT global seeder 60
4.5 Mach 10 local seeding injector 61
4.6 Tunnel 9 protruding seeding housing 62
4.7 Seeding plumbing pressure rise 64
4.8 M3CT ramp model 67
4.9 Velocity decay showing particle response 68
4.10 Particle relaxation on rotated shock-normal velocity 68
4.11 Simulated particle response 72
4.12 Quasi-steady parameter progression with time 73
4.13 Sample interrogation window concentration method comparison . . . 75
4.14 Gaussian elimination process 77

5.1 Fit to Cole's Law of the Wake 80
5.2 Inner scaled van Driest transformed velocity 81

5.3 Comparison vector processing spatial resolution . . . 84
5.4 Comparison camera magnification spatial resolution . . . 85
5.5 Morkovin scaled streamwise fluctuating velocity . . . 88
5.6 Morkovin scaled streamwise fluctuating velocity comparison to literature . . . 89
5.7 Morkovin scaled streamwise fluctuating velocity, inner scaled . . . 90
5.8 Morkovin scaled wall-normal fluctuating velocity . . . 91
5.9 Stokes number effect on wall-normal fluctuating velocity magnitude . 92
5.10 Morkovin scaled wall-normal fluctuating velocity comparison to literature . . . 94
5.11 Morkovin scaled Reynolds shear stress . . . 95
5.12 Stokes number effect on Reynolds shear stress . . . 96
5.13 Morkovin scaled Reynolds shear stress comparison to literature . . . 97
5.14 Wavenumber cutoff on the fluctuating velocity power spectral density 100
5.15 Large scale motion structures with comparison to literature . . . 101

6.1 Particle concentration comparisons . . . 105
6.2 Inner scaled van Driest transformed velocity . . . 106
6.3 Streamwise velocity comparison between local and global . . . 107
6.4 Morkovin scaled turublence statistics . . . 110
6.5 Relative error between local injection and global seeding . . . 113
6.6 Normalized conentration comparing local injection to global seeding . 114
6.7 Local injection valid vector percentages . . . 115
6.8 Particle baising shown in the velocity probability distribution function 117
6.9 Intermittency of the boundary layer in a PIV frame . . . 118
6.10 Intermittency factor distribution in the boundary layer . . . 119
6.11 Skewness distribution in the boundary layer . . . 120

7.1 Modifications to the HCF Seeding Injector . . . 122
7.2 Tunnel 9 Injector Modifications . . . 123
7.3 HCF leading edge injector housing . . . 125
7.4 HCF image correction GUIs . . . 126
7.5 Dimensional particle concentration compared to CFD . . . 127
7.6 Inner scaled van Driest transformed velocity . . . 129
7.7 Morkovin scaled streamwise flcutuating velcoity . . . 130
7.8 Large scale motion strucure . . . 131
7.9 STBLI mean velocity contour plot . . . 132
7.10 STBLI wall-tangent velocity profiles . . . 133
7.11 STBLI mean wall-tangent velocity profiles at several x/δ locations downstream of the compression corner. . . . 133
7.12 Morkovin scaled upstream wall-tangent fluctuating velocity profiles . 134
7.13 Morkovin scaled downstream wall-tangent fluctuating velocity profiles 134

Nomenclature

A^*	Injector throat area
C	Log law intercept
C	Particle concentration
C_f	Coefficient of friction
D_I	Interrogation window size
d_p	Particle diameter
d_s	Particle image diameter
f	Focal length
f_{Kn}	Knudsen number correction factor
H	Shape factor
H_p	Particle response function
h	Particle pixel intensity (Adrian and Yao [1] nomenclature)
I	Particle pixel intensity
Kn_p	Knudsen number, particle
k	Wavenumber
$k_{cutoff,p}$	Particle response wavenumber limit
$k_{cutoff,w}$	Interrogation window wavenumber limit
k	Kinetic stress
M	Mach number
M_0	Camera magnification
M_p	Particle slip Mach number

$\dot{m}$	Mass flow rate
$\overline{P_{u_i}}$	Precision uncertainty on velocity
Pr	Prandtl number
p	Pressure
p_2	Post-shock pressure
Q	Heat transfer
R	Gas constant
R^2_{adj}	Coefficient of determination, adjusted by number of fitted points
R_{uu}	Streamwise spatial correlation coefficient
Re	Reynolds number
Re_m	Unit Reynolds number
Re_p	Particle slip Reynolds number
Re_τ	Skin friction Reynolds number
Re_θ	Momentum thickness Reynolds number
r	Recovery factor
SR	Spatial resolution
St	Stokes number
S_u	Skewness
s	Distance from particle center
T	Temperature
u	Streamwise velocity
u_{vd}	van Driest transformed velocity
u_τ	Skin friction velocity
v	Wall-normal velocity
$var(\ldots)$	Variance
x	Streamwise dimension
y	Wall-normal dimension

β	Clauser equilibium parameter
δ	Boundary layer thickness (Coles Fit)
δ_{99}	Boundary layer thickness, 99% of U_e
ϵ	Dissipation rate
ϵ	Relative error
ϵ	Stokes number, without Kn correction
γ	Ratio of specific heats
γ	Intermittency factor
κ	Log law slope
μ	Mean
ν	Kinematic viscosity
ω	Circular frequency
Π	Wake strength parameter
ϕ	Particle slip Reynolds number factor
ϕ	Large scale motion structure angle
ρ	Density
σ	Standard deviation
τ	Shear stress
τ_f	Fluid response time
τ_p	Particle response time
θ	Momentum thickness
ξ_p	Particle relaxation distance

Superscript

**	van Driest general velocity (cold wall)
*	van Driest general velocity
*	Morkovin scaling

$^+$	Inner scaling
$'$	Fluctuating velocity component

Subscript

$_0$	Reservoir condition
$_e$	Boundary layer edge condition
$_g$	Global seeding parameter
$_i$	Streamwise distance to particle center
$_j$	Wall-normal distance to particle center
$_n$	Shock-normal component
$_r$	Reservoir condition
$_w$	Wall condition
$_\infty$	Freestream condition

Chapter 1: Introduction

The importance of hypersonic aerodynamic research is ever increasing. New hypersonic system applications require adequate testing to reduce risk during development. Numerical techniques, such as direct numerical simulation (DNS) and large eddy stimulation (LES) greatly reduce development risks by shifting some of the development cost away from physical testing. However, the importance of ground testing is as critical as ever since these methods must be validated. Particle image velocimetry (PIV) provides the quantified instantaneous spatially correlated velocity measurements necessary to validate the flow physics used in these models.

Tunnel 9 has three unique aspects that makes it an ideal facility for the validation of CFD codes. The 1.5 m nozzle exit diameter allows for the testing of large models that produce a thick boundary layer. This increases the turbulent scales which decreases measurement errors due to particle lag and spatial resolution. Tunnel 9 can produce high unit Reynolds numbers above 30×10^6/m at Mach 10. This allows the generation of a fully turbulent boundary layer free of transitional effects. Finally, long test times (compared to impulse facilities) on the order of one second yield a large amount of data without the necessity of a long test program. This is particularly necessary for the use of relatively low repetition rate ($\mathcal{O}(100)$ Hz)

Nd:YAG lasers typically used for supersonic and hypersonic PIV. Current measurement techniques at large scale hypersonic facilities such as the AEDC Hypervelocity Wind Tunnel 9 (Tunnel 9) include force and moment, conventional and novel surface measurements, and several optical measurements outlined by Lafferty et al. [2].

The objective of this research program is to demonstrate hypersonic PIV in Tunnel 9. This objective was satisfied by measuring velocity in the turbulent boundary layer (TBL) and shock turbulent boundary layer interaction (STBLI) generated by a large hollow cylinder flare (HCF) test article at Mach 10 with a freestream Reynolds number of 16.0×10^6/m.

PIV has become a mature measurement technique in subsonic and supersonic conditions but remains an emerging technology at the hypersonic flow regime. PIV has been successfully implemented by numerous small scale hypersonic facilities, notably Delft Mach 7 Ludwieg tube [3], the Mach 8 Hypersonic Boundary Layer Facility at Princeton, [4, 5, 6, 7] the Mach 4.89 tunnel at the National Aerotherochemistry laboratory at Texas A&M university, [8, 9] and the Mach 5 blow down tunnel at University of Texas at Austin [10].

The large majority of supersonic and hypersonic PIV experiments use what is referred to here as global seeding. This approach involves the injection and mixing of particles into the settling tank upstream of the supersonic nozzle. As a result, the entirety of the working fluid contains particles. Global seeding is impractical to use in Tunnel 9 for multiple reasons. The large volume of working fluid necessary per run is a significant consideration which makes the cost of global seeding prohibitive. In addition, global seeding would create a health hazard due to the

large amount of sub-micron particles introduced into the facility. Also, the high reservoir temperature (up to 2000 K) and pressures (up to 125 MPa) would most likely degrade the particles if introduced into the settling tank. Furthermore, the globally seeded particles would interfere with other measurement techniques such as schlieren, temperature sensitive paint, krypton tagging velocimetry, etc.

To overcome the limitations of global seeding, a local seeding technique was developed and demonstrated in Tunnel 9. With local seeding, particles are injected near the wall so that only a narrow spanwise band centered on the measurement location contains particles. I am aware of four other researchers who have employed local seeding, further outlined in Section 2.1. Of these researchers, the successful PIV applications introduce seeding in the subsonic portion of the nozzle. Most of these applications inject seeding particles at the wall, with the exception of Ghaemi et al. [11]. One unpublished study (by Allen and described in Sahoo et al. [6]) attempted local seeding in the high-speed section of the flow. However, this effort was abandoned because of disturbances in the flow field due to the injection.

Unlike the previously published local seeding experiments, locally seeding the subsonic portion of the nozzle is not viable. The measurements are conducted on a sting-supported model in the core flow of the test section which precludes subsonic nozzle wall injection. Local seeding in the supersonic region would require seeding injection through a supply tube terminating along the nozzle centerline, similar to the approached used by Ghaemi et al. [11]. Due to the small throat diameter, and large nozzle area ratio, the particles would greatly disperse during expansion if a relatively large supply tube is used. A smaller supply tube would most likely not

be able to supply enough particles. Furthermore, significant facility modifications would be necessary to adapt a local injector in the subsonic portion of the nozzle. These modifications would require mandatory facility risk analyses. Hypersonic PIV is not yet a mature enough technology to allow a full scale T&E facility such as Tunnel 9 to commit to such modification.

As a result, local injection in Tunnel 9 must take place in the high-speed test section. The injector is located in the leading edge of the HCF test article. To mitigate flowfield disturbances, the local injector is designed as a supersonic nozzle which exits tangentially along the outer mold line (OML) instead of a slot injector. Accelerating the seeding aerosol reduces the difference in momentum between the external and injected flows which reduces the impact of the mass injection on the flowfield. The geometry of the injector nozzle profiles were developed using CFD. The particle tracking codes allowed us to iterate the nozzle profiles to get the desired particle concentration and distribution throughout the boundary layer and minimize the impact to the flow.

The tight test schedule and cost of operating Tunnel 9 limits tunnel availability for long development programs. Therefore, development of the local injectors began in the Mach 3 Calibration wind Tunnel facility (M3CT) where the high-speed local seeding injector was first tested. The greater availability of the M3CT and longer run times facilitated development because a large number of samples can be quickly generated.

The flowfield of study in the M3CT is a canonical supersonic turbulent boundary layer. Good agreement between the PIV measurements, theory and literature

provides confidence in the design of the injector and the ability of the particles to follow turbulent eddies in the flow. Using the M3CT design operating conditions, the maximum achievable Stokes numbers are between $\sim 0.26 - 0.60$. In order to generate Stokes numbers comparable to that achieved in Tunnel 9, orifice plates were used to reduce the Reynolds number in the M3CT. In addition, reducing the Reynolds number brings the flow conditions closer to those achieved in direct numerical simulation (DNS), with the exception of a few high Reynolds number studies such as those completed by Pirozzoli et al. [12, 13]. A wide range of reservoir pressures, measurement locations, and camera magnifications create an overlap in the parameter space in one research facility. This allows us to assess the effect of the flow conditions and PIV parameters on the measurements.

Flat plate turbulent boundary layers are well studied canonical flows [14, 15, 16, 17]. The most well known experimental data is the hot wire anemometry (HWA) measurements conducted by Klebanoff [18]. However, there exist large variations between supersonic turbulent fluctuating velocity profiles reported in literature which remain largely unresolved. These data not only include particle based techniques, such as particle image velocimetry (PIV) [19, 20, 21] and laser Doppler velocimetry (LDV) [22], but also HWA [22, 23, 24] and krypton tagging velocimetry (KTV) [25, 26]. Therefore, effects from the particle response are not the sole mechanism for the variations between experiments. Williams et al. [27] presented a detailed analysis of uncertainties that could contribute to these variations. These authors cite frequency response and spatial resolution as contributing factors to HWA uncertainty and spatial resolution and particle response as contributing factors to PIV

uncertainty. However, these effects to not completely explain the variations in data from the literature. For example, there is good agreement between HWA and LDV data from Eléna and LaCharme [22].

Figure 1.1, partially reproduced from Eléna and LaCharme [22], gives a representation of the extent of the variations. Eléna and LaCharme established limits for these variations from published HWA data, under a range of Mach numbers from 1.7−4.7 with outer limits from Smits et al. [23] and Kistler [24]. Eléna and LaCharme noted that the reason for the spread remains unexplained. LDV data from Eléna and LaCharme showed very good agreement with incompressible HWA data from Klebanoff. Eléna and LaCharme noted that the better agreement than other LDV published data was due to improvements with LDV seeding.

This dissertation is divided into multiple parts. The first provides information on the experimental facilities, PIV setup, and methods used for analyzing the PIV velocity. This includes detailed descriptions of Tunnel 9 and the M3CT facilities and capabilities. Then, I further expand on the facilities to include components and layout of the equipment used in PIV. The determination of flow parameters with consideration of turbulent boundary layer theory is presented. Finally, I provide an explanation of recurring presented data such as Morkovin scaled fluctuating velocity, spatial correlation coefficients for the determination of large-scale turbulent structure size and angles, and power spectra densities.

The second is dedicated to the studies conducted at the M3CT. This part presents PIV measurements in a Mach 2.7 turbulent boundary layer. Nine reservoir pressures are tested to characterize the effect of the Reynolds number and Stokes number on

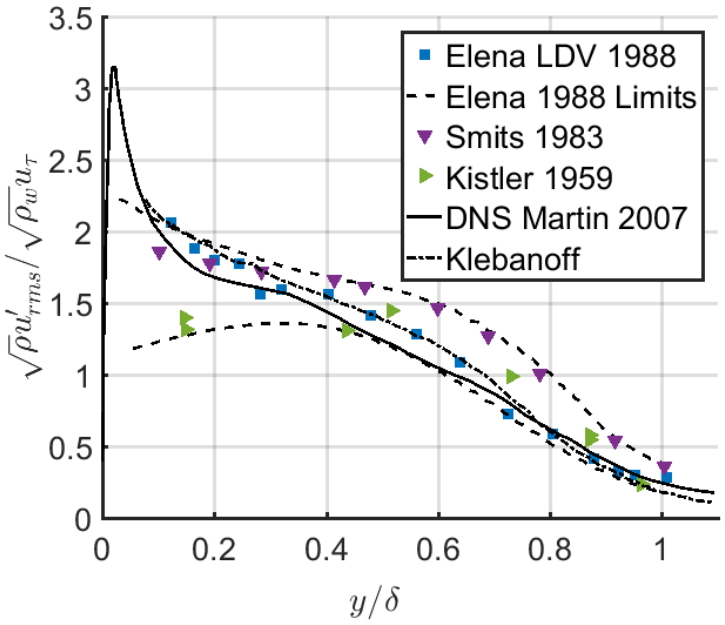

Figure 1.1: Morkovin scaled streamwise fluctuating velocity profile, reproduced from Eléna and LaCharme 1988 [22], to show the spread of data in literature. M=2.32 LDV data and 1.7 < M < 4.7 HWA data limits from Elena and LaCharme 1988 [22], M=2.9 HWA from Smits et al. 1983 [23], M=3.56 HWA from Kistler 1959 [24], M=2.32 DNS from Martin 2007 [28], incompressible HWA data from Klebanoff 1955 [18].

the measurements. Test conditions are repeated with various camera magnifications to characterize the effect of spatial resolution. I present the effect of spatial resolution on fluctuating velocity magnitudes by independently varying the camera magnification and the interrogation window size. Mean streamwise velocity profiles are compared to boundary layer theory using inner scaling. Fluctuating streamwise and wall-normal velocity profiles as well as Reynolds shear stress profiles are also presented. Also, the effect of the Stokes number on the wall-normal fluctuating velocity magnitude is assessed. The measurements are compared against DNS for supersonic turbulent boundary layers from Pirozzoli and Bernardini [12] and Duan, Beekman and Martin [29] as well as PIV [19, 20, 21], LDV [22], HWA [18],

and krypton tagging velocimetry (KTV) [25]. Power spectra densities (PSD) of the streamwise and wall-normal fluctuating velocities are shown to illustrate the effect of particle response and window resolution on the resolved energy content. Contours of streamwise correlation coefficients are presented to determine the angle and scale of the large scale motion (LSM) turbulent structures.

The third part expands on the design, development and application of high-speed local PIV seeding injectors to measure Mach 3 and Mach 10 turbulent boundary layers. Data presented in this section are from TBL measurements at two streamwise locations in the M3CT and one location in Tunnel 9. The measurements in the M3CT were repeated using global seeding to characterize the effect of particle injection on the flow. Two methods are presented to calculate particle concentration from PIV images, thresholding and a newly developed Gaussian elimination method. The particle concentration distribution and magnitude in the boundary layer is compared to CFD solutions used to develop the injector nozzle profiles. Local seeding mean streamwise velocity profiles are compared to global seeding and boundary layer theory using inner scaling. Effects of seeding method on fluctuating streamwise and wall normal velocity profiles as well as Reynolds shear stress profiles are also presented. Finally, concepts of local seeding particle biasing are developed and used to explain discrepancies between local and global seeding mean velocity and turbulent statistics profiles.

The final part presents the application of PIV in the large scale Hypervelocity Wind Tunnel No. 9 at AEDC White Oak. The main results focus on quantified mean and fluctuating streamwise velocity in a turbulent boundary layer (TBL) and sev-

eral streamwise locations in a shock turbulent boundary layer interaction (STBLI) region. These results are normalized to compare with DNS and experiments in literature. Also included are the identification of large scale structures through spatially correlated streamwise velocity fluctuations.

Chapter 2: Background and Theory

2.1 Hypersonic and Local Seeding Literature Review

Some of the first PIV studies in hypersonic flows were performed at Delft by Schijer et al. in a Ludwieg tube facility on a double ramp configuration at Mach 7 [30]. Seeding was achieved with 400 nm agglomerates of TiO_2 particles introduced in the supply tube at a stagnation temperature of approximately 800 K. Good agreement was achieved between the PIV measurements and theory for the velocity ratios and flow deflections across the shocks. The limited spatial resolution and scattering form the solid wall prevented near wall measurements. It was concluded that PIV is a suitable quantitative measurement technique for hypersonic flows.

At Princeton, Sahoo et al. [6, 7], Schreyer et al. [31] and Williams and Smits [4] used TiO_2 particles produced using a fluidized bed seeder in a 9 in diameter Mach 7.4 blowdown wind tunnel. The particles were introduced in the settling chamber upstream of the throat where the stagnation temperature reached 870 K. Successful measurements of the streamwise velocity fluctuation on a flat plate turbulent boundary layer and good agreement with DNS of Priebe and Martin [32] were achieved. Velocity fluctuations in the wall-normal direction were significantly less than DNS. This disagreement could be due to the insufficient response time of

the TiO_2 particles. Inconclusive data in an early study by Sahoo et al. [6] caused the authors to emphasize the importance of seeding quality in PIV results. Schreyer et al. [31] used PIV to measure the amplification of wall-normal velocity fluctuations and Reynolds stresses after a STBLI of a Mach 7.2 compression corner.

At Texas A&M, Tichenor et al. [8, 33] used dioctyl phthalate (DOP) particles in a Mach 5 blowdown wind tunnel with a 3×3 in^2 test section and a stagnation temperature of 380 K and freestream Reynolds number of about 50×10^6/m. A TSI Model 9306 six-jet atomizer was housed in a pressurized vessel allowing the generation of 250 nm particles at a pressure greater than that of the settling chamber. Measurements were performed in a zero pressure gradient turbulent boundary layer as well as for favorable pressure gradients of various strengths. For the zero pressure gradient boundary layer, good agreement was obtained between the measurements and DNS for streamwise and wall-normal velocity fluctuations. The PIV measurements were also successful in characterizing the stabilizing trends in the Reynolds stresses in the case of a strong favorable pressure gradient. In the same tunnel, Peltier et al. [34] using TiO_2 particles, achieved good agreement with the previous results of Tichenor et al. [8, 33]. The increase in Stokes numbers from $\sim$0.07 (for DOP) to $\sim$0.17 for (for TiO_2) did not significantly impact the streamwise and wall-normal velocity fluctuations.

Wagner et al. [10] used PIV to investigate unstart of scramjet engines at the University of Texas at Austin. The PIV measurements were performed in a Mach 5 blowdown wind tunnel using 260 nm TiO_2 agglomerates produced with a two stage fluidized bed seeder upstream of the stagnation chamber. It was concluded that

the flow structure occurring during the unstart can be successfully characterized by PIV. The PIV data were consistent with both shock expansion theory and previous schlieren measurements. Moreover, PIV provided new insights on the three dimensional nature of unstart and aspects of supersonic entrance flow.

Particle response and seeding are key aspects for successful PIV measurements. Crosswy [35] presented a thorough comparison of a number of different types of seeding materials and seeding methods. It was found that a mixture of ethanol and DOP generated with a vaporization/condensation seeder produced particles closest to monodispersity while still producing quality PIV images. This seeder had the additional benefit of controlling the particle size and production rate. Tobacco and incense smoke produced monodisperse particles, however, they were found to be too small for PIV diagnosis. All the solid particles tested had the tendency to agglomerate causing the formation of large polydisperse particles. Solid particles tested included MgO, Al_2O_3 and TiO_2 produced using a fluidized bed.

Ragni et al [36] compared the particle response for a number of seeding materials. They found that TiO_2 with a 50 nm crystal size gave the shortest response times. However, they encountered challenges with keeping the solid seeding particles dehydrated. Also, the particles needed to be filtered to maintain a small size, which greatly reduced the number of particles to a level most likely below Tunnel 9 requirements. Ragni found that oil seeding had a larger response time than certain solid seeding materials. However, the Laskin nozzle atomizer used produced 1 μm droplets, which is significantly larger than the 0.250 μm droplets obtained by Tichenor et al. [8, 33] using a TSI Model 9306 six-jet atomizer [8].

There are four researchers of note who implemented local seeding instead of global seeding for supersonic or hypersonic PIV. Dupont et al. [37] performed PIV measurements on a shock-wave-induced separation on the wall of a Mach 2.3 wind tunnel. The authors injected incense smoke in the subsonic region upstream of the nozzle through three holes in the wall. Lowe et al. [38] investigated particle lag in a Mach 2.0 turbulent boundary layer generated on the tunnel wall. They used dioctyl phthalate (DOP) oil particles injected in the subsonic portion upstream of the nozzle throat. To confine the particles to the boundary layer, a seeding block that consisted of a 1 in. national pipe thread (NPT) supply hole with a baffle plate was installed into the wall. Ghaemi et al. [11] characterized the particle lag of aluminum oxide nanoparticles through an oblique shock generated by a wedge at Mach 2. The particles were locally injected on the nozzle centerline using a downstream facing supply tube terminating in the subsonic portion of the nozzle. Sahoo et al. [6] explained the local seeding setup used by Allen in an unpublished Mach 7.2 hypersonic PIV experiment. Allen introduced TiO2 particles in a hypersonic boundary layer using a slot injector located downstream of a trip wire near a flat-plate leading edge. However, the injected seeding mass resulted in a disturbed flowfield at the measurement section and the author switched to global seeding.

2.2 Analysis Theory

Several concepts and parameters are recurring throughout the sections of this dissertation. The theory used to determine these values presented in subsequent chapters

are described in the following subsections.

2.2.1 Turbulent Boundary Layer Theory

Inner and outer scaling are generally used to analyze turbulent boundary layers. Inner scaling is used near the wall where viscosity is important and has a length scale equal to ν/u_τ. Outer scaling is applicable in the region where turbulent kinetic stresses dominate and has a length scale equal to δ. Both scalings use u_τ as the velocity scale. For incompressible ZPG turbulent boundary layers, Millikan [39] proposed a region where both inner and outer scales are simultaneously valid. This region is known as the log layer because dimensional analysis based on inner and outer scaling reveals that the velocity profile has a logarithmic relationship, where

$$u^+ = \frac{u}{u_\tau} = \frac{1}{\kappa} \log\left(\frac{u_\tau y}{\nu_w}\right) + C. \tag{2.1}$$

The constants in Eq. 2.1 are nearly universal for incompressible turbulent boundary layers. For this study we adopt the generally accepted values of $\kappa = 0.40$ and $C = 5.1$. Although, there exists some ambiguity regarding their exact values in the literature (see Fernholz and Finley [14]).

Incompressible theory is extended to compressible flows by modifying the dimensional analysis to account for changes in density using the van Driest effective velocity [16], defined as

$$u^* = \int_{u_1}^{u} \sqrt{\frac{\rho}{\rho_w}} du, \tag{2.2}$$

where u_1 is the streamwise velocity at the lower edge of the log layer. The mean density profile (including ρ_w) is found using temperature determined from the Walz equation [40] and the perfect gas law assuming constant pressure throughout the boundary layer. The Walz equation is substituted into Eq. 2.2 in order to obtain the closed-form equation

$$u^* = \frac{u_e}{b} \sin^{-1}\left(\frac{2b^2(u/u_e) - a}{\sqrt{a^2 + 4b^2}}\right), \tag{2.3}$$

where

$$a = \left(1 + r\frac{\gamma - 1}{2} M_e^2\right) \frac{T_e}{T_w} - 1, \tag{2.4}$$

$$b^2 = r\frac{\gamma - 1}{2} M_e^2 \left(\frac{T_e}{T_w}\right), \tag{2.5}$$

and $r = \sqrt[3]{Pr}$ is the recovery factor. For the case of an adiabatic ZPG flat-plate compressible turbulent boundary layer, the recovery temperature is equal to the wall temperature making the term $a = 0$. And, the velocity profile in the log layer is defined as

$$u_{vd}^+ = \frac{u^*}{u_\tau} = \frac{1}{\kappa} \log\left(\frac{u_\tau y}{\nu_w}\right) + C. \tag{2.6}$$

where κ and C are the same as defined in Eq. 2.1.

Spalding [41] developed an empirical velocity profile equation for the entire inner scaling region of a turbulent boundary layer. The equation valid for the velocity in

the viscous sub-layer, log layer and intermediate overlap region is defined as

$$y^+ = u^+_{vd} + e^{-\kappa C}\left[e^{\kappa u^+_{vd}} - 1 - \kappa u^+_{vd} - \frac{1}{2}(\kappa u^+_{vd})^2 - \frac{1}{6}(\kappa u^+_{vd})^3\right].$$

Coles [15] extended the log law into the outer scaling region by adding a wake function to describe the departure from the log layer. The derived law of the wake,

$$u^+_{vd} = \frac{1}{\kappa}\log\left(\frac{u_\tau y}{\nu_w}\right) + C + \frac{2\Pi}{\kappa}\sin^2\left(\frac{\pi}{2}\frac{y}{\delta_c}\right), \tag{2.7}$$

is valid from the log layer through to the outer region including the intermediate overlap.

The wall is no longer adiabatic in Tunnel 9 which has a wall temperature ratio of $T_w/T_r \approx 0.3$. The log layer slope is assumed to be the same as the incompressible value of $\kappa = 0.4$. But the intercept is not assumed to be $C = 5.1$ due to the cold wall. For Tunnel 9, the van Driest general velocity takes the form

$$u^{**} = \frac{u_e}{b}\sin^{-1}\left(\frac{2b^2(u/u_e) - a}{\sqrt{a^2 + 4b^2}}\right) + \frac{u_e}{b}\sin^{-1}\left(\frac{a}{\sqrt{a^2 + 4b^2}}\right). \tag{2.8}$$

For Tunnel 9, the law of the wake (Eq. 2.7) is expressed as the velocity defect from

the freestream such that

$$\frac{(u_e^{**} - u^{**})}{u_\tau} = -\frac{1}{\kappa}\log\left(\frac{y}{\delta}\right) \tag{2.9}$$

$$+ \frac{2\Pi}{\kappa}\left(1 - \sin^2\left(\frac{\pi}{2}\frac{y}{\delta_c}\right)\right), \tag{2.10}$$

where u_e^{**} is Eq. 2.8 evaluated at the boundary layer edge. Using the velocity defect causes C in Eq. 2.7 and the second term of the RHS of Eq. 2.8 to cancel. Now, no assumption must be made on the cold wall effects on C.

The skin friction velocity (u_τ), boundary layer thickness (δ), and the wake strength parameter (Π) are simultaneously calculated by fitting Eq. 2.7 to the M3CT data and Eq. 2.9 to Tunnel 9 data. Following the work of Lewis et al. [42], the fitting region for the PIV data is limited to $y^+ = u_\tau y/\nu_w > 50$ to avoid points with increased measurement uncertainty near the wall, and $u/ue < 0.98$ as Eq. 2.7 is not valid at $y = \delta$.

2.2.2 Boundary Layer Thickness

The boundary layer thickness is used in this study and numerous others as a significant scaling parameter. Although simple in concept, during the analysis of these data it became apparent that certain methods to quantify this parameter do not accurately determine the boundary layer edge ubiquitously. Moreover, multiple formulations of the boundary thickness are used in the literature. It is important to compare data using the same length scale as to not artificially distort comparison of data profiles which rely on this parameter or parameters determined by the bound-

ary layer thickness. As such, I considered four definitions of the boundary layer thickness, Equations 2.11. The selection of the calculation method depended on literature comparisons and seeding methodology.

Two of the most straight forward methods of calculating the boundary layer thickness are to determine the wall normal location when the measured velocity is within a certain percentage of the freestream velocity, 99% and 99.9% for δ_{99} and δ_{999}, respectively.

$$u\left(\delta_{99}\right) = 0.99u_e \tag{2.11}$$

$$u\left(\delta_{999}\right) = 0.999u_e \tag{2.12}$$

The freestream velocity u_e is calculated as the average of data points well into the freestream, determined by inspection of the mean velocity profile. Linear interpolation between the interrogation point and the preceding point determines the final location of the boundary layer thickness. These definitions are used for low Reynolds number experiments at the M3CT using global seeding in Chapter 5.

Higher accuracy is hoped to be achieved by using an integral approach rather than simply a percentage of an average. The contributions to the integral $\int y(u)\,du$ diminish as u is increased to the freestream velocity, i.e. as y approaches the boundary layer thickness. Therefore, the boundary layer thickness can the be determined as the value for y corresponding to the velocity point when the integral changes by less

than a certain tolerance, e.g. 0.5%:

$$\frac{\int_u^{u+\Delta u} y(u)\,du}{\int_0^u y(u)\,du} <= 0.005 \tag{2.13}$$

Again linear interpolation is used to find the sub-interrogation window spaced boundary layer thickness. This method did not produce accurate representation of the boundary layer thickness for all conditions. The previous definitions of δ_{99} and δ_{999} are preferred over the integral fit.

Coles law of the wake (Eqs. 2.7 and 2.9) is used to determine the boundary layer thickness by calculating a nonlinear least squares fit to the PIV data. Eqs. 2.6 and 2.7 may also be used to determine the boundary layer thickness. However, Coles's law of the wake is preferred because there were more PIV data points over the region where Eq. 2.7 is valid compared to Eqs. 2.6 and 2.7. Also, the location and extent of the log layer varies with Reynolds number, and diminishes at low Reynolds numbers. This would introduce subjectivity in the selection of PIV data used for a fit of Eqs. 2.6 and 2.7. Eq. 2.7 is used for the M3CT data and Eq. 2.9 for the Tunnel 9 data.

Following the work of Lewis et al. [42], the fitting region for the PIV data is limited to $y^+ = u_\tau y/\nu_w > 50$ to avoid points with increased measurement uncertainty near the wall, and $u/ue < 0.98$ as Eq. 2.7 is not valid at $y = \delta$. The fit to Eq. 2.7 simultaneously calculates the skin friction velocity u_τ the Coles boundary layer thickness δ_c, and the wake strength parameter Π. Agreement between the PIV data and Eq. 2.7 gives confidence in the measurements. The adjusted coefficient

of determination is used to assess the quality of the fit. The adjusted coefficient of determination takes into account the number of data points used for the fit and the number of parameters determined by the fit.

2.2.3 Skin friction velocity

Along with the Coles law of the wake, the skin friction velocity is also determined by the Kármán-Schoenherr formulation of the incompressible friction coefficient. This method is recommended by Hopkins and Inouye [43] to determine the supersonic and hypersonic skin friction velocity. The skin friction velocity is determined classically by

$$u_\tau = \sqrt{\frac{\tau_w}{\rho_w}} = \sqrt{\frac{0.5 C_f \rho_\infty u_\infty^2}{\rho_w}}. \tag{2.14}$$

The friction coefficient can be found from the Kármán-Schoenherr equation:

$$\bar{C}_f = \left[17.08 \left(\log_{10} \bar{R}e_\theta\right)^2 + 25.11 \log_{10} \bar{R}e_\theta + 6.012\right]^{-1}. \tag{2.15}$$

The barred terms are transformations from compressible to incompressible, such that

$$\bar{C}_f = F_c C_f \tag{2.16}$$

and

$$\bar{R}e_\theta = F_\theta Re_\theta. \tag{2.17}$$

The terms F_c and F_θ are calculated from the van Driest II transformation which defines these terms as

$$F_c = rm/\left(\sin^{-1}\alpha + \sin^{-1}\beta\right)^2 \tag{2.18}$$

and

$$F_\theta = \mu_e/\mu_w \tag{2.19}$$

where

$$\alpha = \left(2A_{VD}^2 - B_{VD}\right)/\left(4A_{VD}^2 + B_{VD}^2\right)^{1/2}, \tag{2.20}$$

$$\beta = B_{VD}/\left(4A_{VD}^2 + B_{VD}^2\right)^{1/2}, \tag{2.21}$$

$$A_{VD} = \left(rm/F\right)^{1/2}, \tag{2.22}$$

and

$$B_{VD} = \left(1 + rm - F\right)/F. \tag{2.23}$$

The Reynolds number based on the momentum thickness is defined as

$$Re_\theta = \frac{\rho_\infty u_\infty \theta}{\mu_\infty}, \tag{2.24}$$

where

$$\frac{\theta}{\delta} = \int_0^1 \frac{\rho u}{\rho_\infty u_\infty}\left(1 - \frac{u}{u_\infty} d\left(\frac{y}{\delta}\right)\right). \tag{2.25}$$

The density profile, ρ, is calculated using the ideal gas equation assuming a constant freestream pressure, p_∞, through the boundary layer and the temperature distribution determined from the velocity profile using the Walz equation

$$\frac{T}{T_\infty} = \frac{T_w}{T_\infty} + \frac{T_r - T_w}{T_\infty}\left(\frac{u}{u_\infty}\right) + \frac{T_\infty - T_r}{T_\infty}\left(\frac{u}{u_\infty}\right)^2. \tag{2.26}$$

The recovery temperature is defined as

$$\frac{T_r}{T_\infty} = 1 + r\frac{\gamma - 1}{2}M_\infty^2. \tag{2.27}$$

2.2.4 Morkovin's Hypothesis

The majority of compressible boundary layer studies from the literature use Morkovin scaling to report turbulence statistics. Morkovin [44] developed a density weighted scaling to collapse compressible data onto incompressible under the observation that "the essential dynamics of these shear flows will follow the incompressible data." Morkovin followed a similar analysis used to develop the turbulent boundary layer theory. However, Morkovin posed a dimensional analysis on the local fluid stresses rather than the velocity. He related the turbulent time scale based on fluid properties to the commonly defined ratio of kinetic stress and dissipation rate

$$t_t = \frac{k}{\epsilon}. \tag{2.28}$$

To evaluate the dissipation rate, Morkovin assumed that the shear stress is constant in the viscous sublayer and equal to the wall shear stress

$$-\overline{\rho u' v'} \approx -\bar{\rho}\overline{u' v'} = \rho_w u_\tau^2, \tag{2.29}$$

where

$$-\overline{u' v'} \propto k. \tag{2.30}$$

Assuming the production term is equal to the dissipation and imposing an inner or outer scaling length term, Morkovin showed that the velocity scale is now $u_\tau \sqrt{\rho_w/\rho}$ instead of u_τ in the constant stress region. This scaling was extended through the boundary layer by assuming a constant length scale in the supersonic regime.

Some questions on the efficacy of this scaling remain in the literature. Particularly, there is debate on the accuracy of Kistler HWA experiments used to validate Morkovin's hypothesis [24]. However, the scaling is still widely used and for the context of this dissertation I assume the scaling is valid.

2.2.5 Large Scale Turbulent Structures

Large scale motion (LSM) of coherent turbulent structures were identified through PIV using two-point spatial correlations of streamwise velocity fluctuations for the entire field of view (FOV). The spatial correlation coefficient was calculated as

$$R_{uu} = \frac{u'(x,y)u'(x+\Delta x, y+\Delta y)}{\sqrt{\overline{[u'(x,y)]^2}}\sqrt{\overline{[u'(x+\Delta x, y+\Delta y)]^2}}}. \tag{2.31}$$

The reference streamwise location was taken as the middle of the FOV and wall-normal location chosen as desired. The structure angle describes the upstream lean of the coherent hairpin turbulence packets as described by Perry and Chong [45] at the given y/δ location. The angle was calculated from the rotation of ellipses that were fitted to the isocontours of the correlation coefficient. The rotation angles were averaged for ellipses that fit well to the data. Contour levels above $R_{uu} = 0.7$ were generally avoided because the reduced number of points near the correlation peak center increases uncertainty in the angle.

2.2.6 Power Spectral Density

The power spectral density (PSD) of the velocity fluctuations shows the distribution of turbulent kinetic energy in relation to turbulence scales size. The PSD was calculated using a periodogram with hamming windows. The signal for the periodogram was the PIV fluctuating velocity spatially correlated along the streamwise direction at a single y/δ row. This transforms the spatial distribution of velocity fluctuations directly to frequency in wavenumber space without assuming a convection velocity. A PSD was calculated for each image pair and averaged.

2.2.7 Measurement Uncertainties

The measurement uncertainty analysis investigated both bias and precision uncertainty. Precision uncertainty was determined statistically and incorporates random errors associated with PIV technique such as camera noise, particle out-of-plane

motion, inhomogeneous particle density, etc. The precision uncertainty on mean velocities and mean fluctuating velocities was calculated using the equation

$$\overline{P_{u_i}} = 1.96\sqrt{var(u_i)}. \tag{2.32}$$

The velocity variance, $var(u_i)$ was found using the formulae in Benedict and Gould [46]. Bias uncertainties, systematic errors due to calibration and vector calculation, were estimated at 1%.

The uncertainty was propagated through the data reduction equations as outlined by Coleman and Steele [47]. Uncertainty on the boundary layer, momentum and displacement thicknesses was estimated using the 1/7th power law [48] since these quantities depend on correlated velocity points in the profile. The uncertainty analysis assumes that the particles accurately follow the flow. Flow parameter uncertainties, and velocity and position uncertainties at $y/\delta = 0.5$ for three PIV experiments from Chapter 6 are presented in Table 2.1. The starred terms in Table 2.1 indicate Morkovin scaled quantities defined as

$$u'^* = \sqrt{\frac{\rho}{\rho_w}}\frac{\sqrt{\overline{u'^2}}}{u_\tau},$$
$$v'^* = \sqrt{\frac{\rho}{\rho_w}}\frac{\sqrt{\overline{v'^2}}}{u_\tau},$$

and

$$(u'v')^* = \frac{\rho\overline{u'v'}}{\tau_w}.$$

Table 2.1: PIV uncertainty for at $y/\delta = 0.5$

	Uncertainty (%)				
Variable	M3CT 2 Global	M3CT 2 Local	M3CT 3 Global	M3CT 3 Local	Tunnel 9 Local
y, y/δ, y^+	0.3, 7.2, 8.9	0.4, 7.3, 8.9	0.4, 7.2, 8.9	0.6, 11.4, 9.4	0.3, 13.6, 5.6
u, u^+_{vd}	1.1, 11.9	1.1, 11.7	1.1, 11.9	1.2, 12.6	1.1, 13.0
u', u'^*	5.8, 10.8	5.4, 10.5	4.7, 10.3	6.9, 11.8	16.9, 19.5
v', v'^*	7.0, 11.5	5.9, 10.8	5.8, 10.8	9.0, 13.1	—
$u'v'$, $(u'v')^*$	16.9, 20.2	14.9, 19.6	15.6, 19.6	21.0, 22.1	—
δ	7.2	7.3	7.2	11.4	13.6
u_e	1.0	1.0	1.0	1.6	1.8
u_τ	8.6	8.6	8.6	9.1	5.1

Chapter 3: Experimental Setup

3.1 Mach 3 Aero Calibration Laboratory Wind Tunnel Facility

The Mach 3 Aero Calibration Laboratory wind tunnel facility (M3CT) at AEDC White Oak is an indraft supersonic wind tunnel with measured freestream Mach numbers ranging from 2.7−2.8 and Reynolds number ranging from 7.8−8.7×10^6/m depending on the measurement location. The M3CT is used to develop and demonstrate novel measurement techniques (including the local injection seeding methodology for PIV) prior to deployment in Tunnel 9. Under nominal conditions, a large vacuum tank downstream of the 63.5 × 63.5 mm^2 test section accelerates ambient room air through a 2-D converging diverging nozzle to provide a test time of approximately 10 seconds. The test section, schematically shown in Figure 3.1, has three measurement locations with modular top/bottom and side inserts located 304, 533, and 762 mm downstream of the throat. Originally designed for solid aluminum blank and aluminum framed glass window inserts, the modular design allows additional tunnel components such as clear polycarbonate or acrylic inserts, seeding injector blocks, single Pitot probe and Pitot rake (see Section 3.2 and also Brooks et al. [49, 50]). The operation of the pneumatic valves and vacuum pump for the M3CT are controlled using a LabVIEW program.

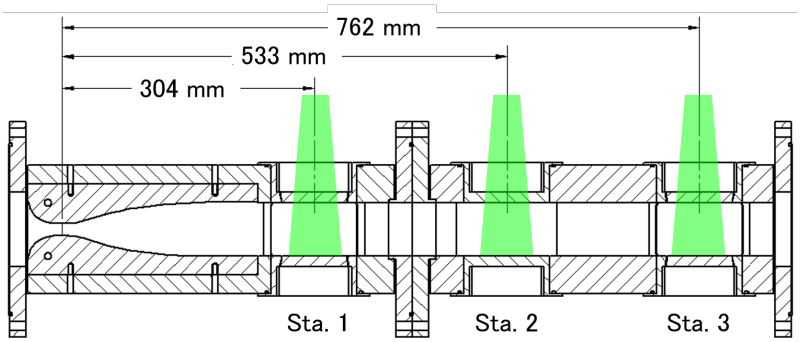

Figure 3.1: Schematic of M3CT test section (mid-spanwise cross-section) showing distance to the three measurement locations relative to the nozzle throat.

The flow field measured in the M3CT study is the zero pressure gradient (ZPG) turbulent boundary layer that develops on the tunnel wall downstream of the nozzle expansion. The recovery temperature is very close to the wall temperature; therefore, the wall is assumed to be adiabatic. The extended length of the test section allows for the growth of a thick turbulent boundary layer, on the order of 10 mm. The flow was determined to transition to turbulence naturally under nominal conditions (without orifice plate) in a previous study by Brooks et al. [50]. The transition location was determined using laminar and turbulent solutions of the Virgina Tech Boundary Layer Applet [51, 52]. The streamwise starting location of the turbulent solution was adjusted to match the boundary layer thickness to the PIV data at the measurement section. This analysis revealed that the flow transitioned in the diverging portion of the nozzle.

Although the M3CT operates at relatively low Reynolds number, the Reynolds number was further reduced in order to more closely compare the particle response time to that estimated for Tunnel 9. The Reynolds number was reduced using orifice plates upstream of the nozzle, as outlined by Zahradka et al. [25]. The orifice

plates limit the flow rate, which reduces the reservoir pressure. A series of screens connected by large diameter (152 mm) piping break up the turbulence induced from the jet at the orifice. Two orifice plates were used to generate three reservoir pressure conditions including use without orifice plate. The reservoir conditions are shown in Table 3.1.

Table 3.1: Orifice plate reservoir conditions

Orifice Plate Diameter (mm)	p_r (kPa)	T_r (K)
—	101.3	307
25.4	50.1	308
19.1	29.5	306

When using an orifice plate, the reduced Reynolds number pushes the transition point further downstream. In certain cases the flow transitioned at the measurement location. To ensure a fully turbulent boundary layer, trips were installed in the subsonic section of the nozzle. The trips were designed to minimize flow disturbances, while still generating the desired well developed turbulent flowfield at the first measurement station. For the 1 inch orifice, a distributed roughness strip was made from 120 grit sandpaper. The 12.7×60.3 mm^2 strip was attached with double sided tape. For the 19.1 mm orifice, two 1.65 mm thick Teflon tape trips measuring 9.5×60.3 mm^2 were installed. Trip sizes were determined experimentally by PIV through the verification of a turbulent boundary layer profile.

The flow conditions for all nine configurations of the M3CT are presented in Table 3.2. The multiple measurement locations and orifice diameters set up an overlapping parameter space in terms of Reynolds number, boundary layer thickness and PIV

particle Stokes number. Mean velocities were ensemble averaged over all image pairs and over a streamwise distance on the order of 1-2δ for a total of about $10,000-50,000$ realizations (approximately 620 frames) at each y/δ location over 0.07. The reservoir and freestream conditions, in Tables 3.1 and 3.2 respectively, are calculated from the PIV and Pitot-static pressure measurements. The Mach number was obtained using a Pitot probe in the freestream and a wall static pressure tap. The freestream temperature was calculated with the definition for the speed of sound, the freestream Mach number and PIV calculated freestream velocity. Finally, assuming an isentropic expansion process, the reservoir pressure and temperature were obtained.

3.2 M3CT Additions

At the start of my research, the M3CT was re-designed for PIV measurements. The prior test cell only had side optical access available. The new design of the test cell retained the Mach 3 nozzle plates of the previous tunnel and added modular windows for top/bottom and side optical access. One of my first tasks was to assemble the M3CT test cell. Particular attention was given to ensure smooth transition between test cell sections including hand blending to remove steps between mating components. I designed several additional components for the M3CT in order to aid my research.

Table 3.2: M3CT reduced Reynolds number flow conditions

Experiment		Station	Position	Orifice	M_e	u_e	Re_m	δ	θ	Re_θ	Re_τ	St	Π
Ref. Code	No.	No.	(mm)	(mm)		(m/s)	(1/m)	(mm)	(mm)				
1A	143	1	300	19.1	2.8	621	2.3×10^6	8.2	0.52	1167	202	1.09	0.54
1B	146	1	300	25.4	2.8	620	3.9×10^6	6.6	0.41	1603	273	0.87	0.42
1C	153	1	300	—	2.8	623	7.7×10^6	5.8	0.34	2631	446	0.60	0.49
2A	162	2	530	19.1	2.8	610	2.4×10^6	12.4	0.82	1963	304	0.67	0.57
2B	161	2	530	25.4	2.8	607	4.2×10^6	10.3	0.67	2811	420	0.51	0.50
2C	154	2	530	—	2.8	605	8.4×10^6	8.6	0.57	4767	657	0.37	0.54
3A	169	3	760	19.1	2.7	598	2.6×10^6	16.3	1.12	2862	420	0.45	0.68
3B	170	3	760	25.4	2.7	600	4.4×10^6	13.3	0.89	3915	571	0.36	0.59
3C	177	3	760	—	2.7	601	8.6×10^6	11.4	0.80	6945	916	0.26	0.65

3.2.1 Pitot Probe

A Pitot probe was desired initially to determine the freestream Mach number at the three measurement locations. The freestream Mach number was used to verify correct assembly and operation of the M3CT a well as characterize the deviation in Mach number with streamwise distance. The implemented design also allowed for boundary layer measurements. These measurements were used to verify turbulent boundary layer behavior as the PIV system was developed and to provide comparison data for the PIV. The Mach number is calculated from the Pitot and static pressures using the Rayleigh supersonic Pitot tube equation

$$\frac{p}{p_{02}} = \frac{\left(\frac{2\gamma}{\gamma+1}M_1^2 - \frac{\gamma-1}{\gamma+1}\right)^{\frac{1}{\gamma-1}}}{\left(\frac{\gamma+1}{2}M_1^2\right)^{\frac{\gamma}{\gamma-1}}}. \tag{3.1}$$

The velocity is also calculated by using the definition of the Mach number

$$M = \frac{u}{\sqrt{\gamma RT}}, \tag{3.2}$$

where the temperature is calculated from freestream conditions or from the Walz equation, Eq. 2.26. When using the Pitot probe, the freestream temperature is found from reservoir conditions assuming isentropic expansion through the nozzle. One of the top/bottom blanks of the test section was modified to accept a Pitot probe and static pressure tap as shown in Figure 3.2. The probe was fabricated from 1.6 mm diameter hypodermic tubing in order to minimize flow disturbances,

while achieving a response time of 52 Hz; sufficient to measure mean pressures. The probe design features a double bend to obtain near wall measurement down to half the probe diameter and a flattened tip reduces the wall normal probe dimension to 0.8 mm to limit spatial averaging an effects of centerline displacement as outlined by Grosser [53]. It is constrained using a compression fitting, allowing for wall normal repositioning. The static pressure tap was positioned flush with the tunnel floor, constrained using thread locker, and located directly below the Pitot probe inlet to measure static pressure at the same streamwise location as the Pitot pressure. Pressures were measured using 0-775 mmHg range Micro Switch (a Honeywell Division) 130PC series pressure sensors. The pressure sensors were calibrated using the vacuum tank of the M3CT. A separate LabVIEW program pulls the vacuum tank down to 3 mmHg in multiple steps. The output voltage of the pressure sensors are correlated to a calibrated tunnel pressure sensor (Baratron) to generate the calibration slope and intercept.

Figures 3.3 and 3.4 show the results from the initial Pitot probe survey of the M3CT turbulent boundary layer at Stations 2 and 3. Figure 3.3

3.2.2 Pitot Rake

The single Pitot tube insert was not traversed during the run. As a result, a large number of runs is necessary to produce a survey of the boundary layer. I designed a Pitot rake, depicted in Figure 3.5, in order to expedite the characterization of a boundary layer, particularly in new tunnel conditions. The rake is designed to

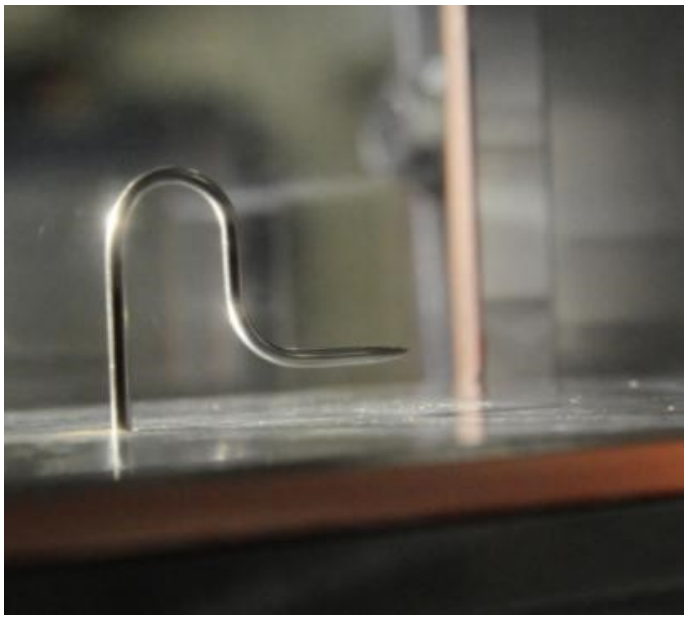

Figure 3.2: Single Pitot probe installed in Station 2

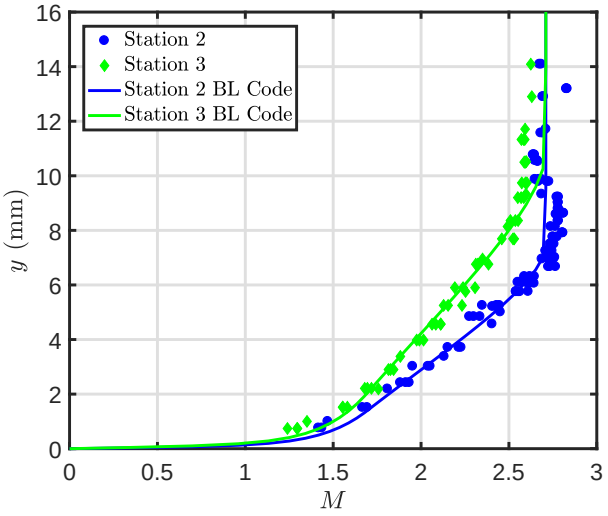

Figure 3.3: Mach number profiles measured using single Pitot probe insert. The VT boundary layer applet [51, 52] used to determine the transition location is also shown for comparison.

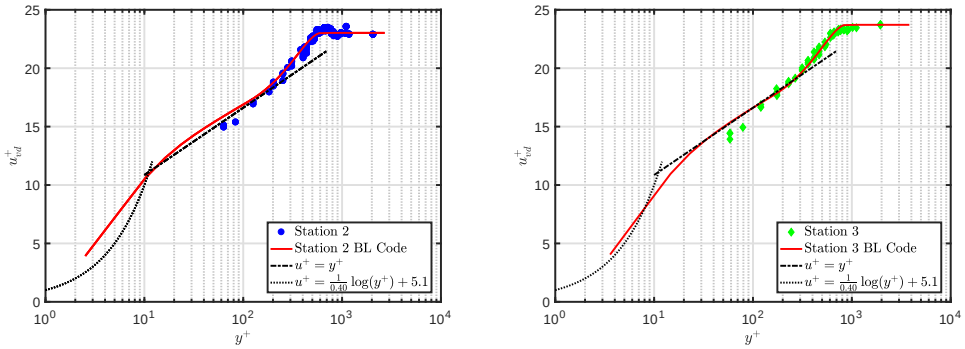

(a) Station 2 (b) Station 3

Figure 3.4: Inner scaled van Driest transformed velocity profiles measured using the single Pitot probe insert. The measured Mach number is compared to Turbulent boundary layer log law theory with $\kappa = 0.40$ and $C = 5.1$. The VT boundary layer applet [51, 52] used to determine the transition location is also shown for comparison.

attach to a blank window insert which can be installed into any station.

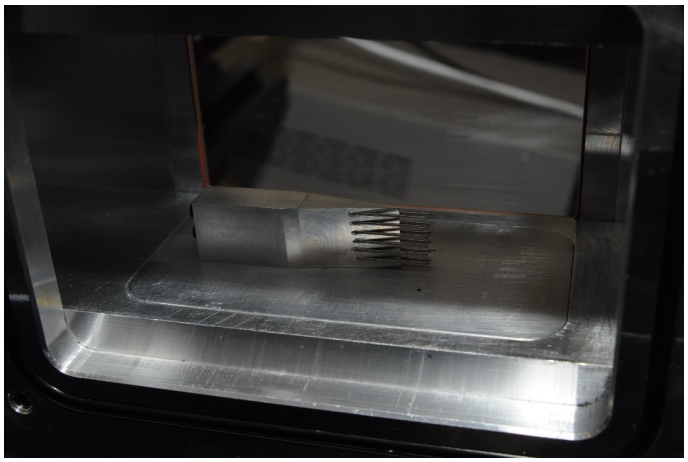

Figure 3.5: Pitot rake CAD representation

The probe diameter was determined to be 0.8 mm in order to obtain a frequency response of 85-Hz ($\sim 1/d$) and minimize the size of the detached shock at the probe. To avoid sonic communication between probes across the detached shocks, the minimum spacing between probes was determined to be $3d$ (2.4 mm). The staggered design allows for 12 pressure measurements with a spatial resolution of

1.2 mm in the wall normal direction. The 10° wedge of the rake guarantees an attached shock for the free stream and the majority of the boundary layer. Due to the decrease in Mach number near the wall ($M < 1.45$), a cutout in the wedge prevents the detached shock from interfering with measurements.

A GUI (depicted in Figure 3.6) was developed in order to expedite the analysis of data from the Pitot rake. The GUI requires an input of two comma separated variable files, the pressure sensor calibration and sensor output from the run. As seen in the left axis of Figure 3.6, the tunnel startup and unstart are visible in the data. The good flow portion of the run was determined automatically by identifying the point where the standard deviation drops below a certain threshold. For this case, the location was chosen when the standard deviation of 200 consecutive points is below 2.5% of the mean output.

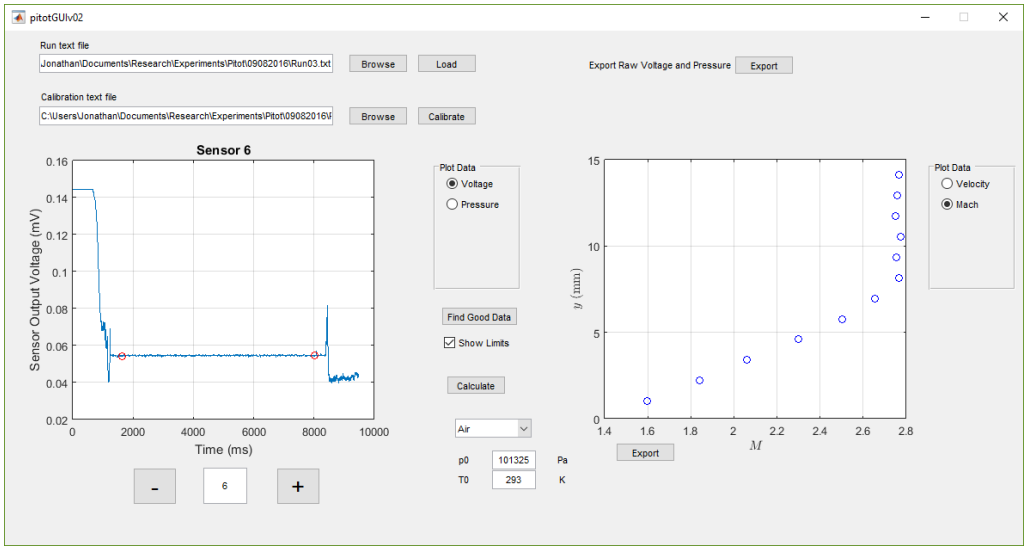

Figure 3.6: Pitot rake analysis GUI

3.2.3 Oblique Shock Diffuser

The 10-s run time quoted in Section 3.2 is in reference to Station 1. The run times at Station 2 and 3 are approximately 7 s and 3 s, respectively. As designed, the test section exhausts as a supersonic jet into the vacuum tank, generating a system of expansion fans which effectively reduces the test section pressure. Therefore, a greater pressure differential between the upstream reservoir and the vacuum tank must be generated to overcome this effect. For the indraft wind tunnel of the M3CT the upstream pressure is fixed at atmospheric conditions and there is a finite amount of volume in the vacuum tank. The tunnel will unstart when the pressure in the tank is not enough to satisfy the conservation of mass, including the pressure drop through the expansion fan. The overall result is a reduction in the started flow test time, most notably in the furthest downstream station, Station 3. I designed an oblique shock diffuser alleviate the pressure drop of the supersonic jet. An ideal oblique shock diffuser will isentropically decelerate the flow to sonic conditions in the second throat. Afterwards, another isentropic subsonic diffuser sends the flow into the vacuum tank maintaining full stagnation pressure of the test cell. Due to the effects of friction, leading to the presence of the boundary layer, this ideal case is not possible. A realistic oblique shock diffuser will produce a series of oblique shock waves terminating in a weak normal shock in the second throat. This process will increase the static pressure while maintaining more stagnation pressure than a normal shock diffuser or the free jet, increasing the started run time.

The actual flow through an oblique shock diffuser is a complex pattern of oblique

shock, expansion wave and boundary layer interactions. For this design, a simplified inviscid flow is used to develop diffuser geometry. The first oblique shock wave intersects the opposite diffuser plate without interacting with another oblique shock wave or the boundary layer. The design developed using this assumption will be verified through testing and the assumption revisited pending testing results. The two main design constraints restrict the minimum second throat height to allow the diffuser to shallow the initial normal shock and restrict the deflection angle so that the first oblique shock intersects the surface of the diffuser throat. When the tunnel starts a normal shock traverses the length of the test section as the flow becomes supersonic, as outlined in Article 5.5 of Anderson [54], Articles 5.5 5.7 of Liepmann and Roshko [55] and Articles 1.4 1.5 of Pope and Goin [56]. The minimum dimension of the second throat is found as a function of the upstream Mach number by assuming sonic flow exists in both the first and second throats. From the conservation of mass, normal shock relations and assuming a perfect gas, it can be shown that ratio of throat areas is given by

$$\frac{A_{t2}}{A_{t1}} = \frac{p_{01}}{p_{02}} = \frac{1+\gamma M_2^2}{1+\gamma M_1^2}\left(\frac{1+\frac{\gamma-1}{2}M_1^2}{1+\frac{\gamma-1}{2}M_2^2}\right)^{\frac{\gamma}{\gamma-1}}. \tag{3.3}$$

The second throat must be larger than the nozzle throat since the stagnation pressure decreases due to the increase in entropy. The Mach number downstream of the normal shock can be found as a function of the upstream Mach number by the equation

$$M_2^2 = \frac{1+\frac{\gamma-1}{2}M_1^2}{\gamma M_1^2 - \frac{\gamma-1}{2}}. \tag{3.4}$$

The area of the first throat can be found using the equation

$$\left(\frac{A}{A_{t1}}\right)^2 = \frac{1}{M_1^2}\left[\frac{2}{\gamma+1}\left(1+\frac{\gamma-1}{2}M_1^2\right)\right]^{\frac{\gamma+1}{\gamma-1}}. \tag{3.5}$$

Using Equations 3.3-3.5 along with known upstream Mach number and test section cross sectional area, the minimum area of the second throat can be determined such that the normal shock can pass through the test section without choking the flow. A safety factory of 1.1 is applied to the minimum area to give a designed height of 52.6 mm with the constant width of 63.5 mm.

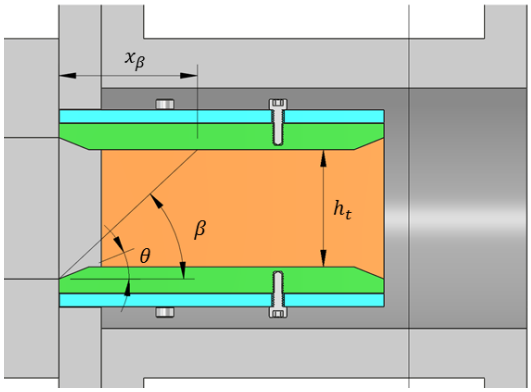

Figure 3.7: Oblique shock diffuser model, flow is from left to right

The minimum deflection angle must be chosen such that the oblique shock intersects the surface of the second throat, using the simplified geometry scenario. The streamwise length of the diffuser is constrained to 146mm to allow for clearance of the butterfly valve which starts the tunnel, as noted by the vertical line in Figure 3.7. The minimum deflection angle can be found as a function of the shock angle using geometry of the constrained length, the calculated second throat height and assuming that the turning angles upstream and downstream of the nozzle are

Table 3.3: Oblique shock diffuser dimensions. Dimension definitions shown in Figure 3.7.

M_1	h_t (mm)	x (mm)	θ (deg)	β (deg)	x_β (mm)
2.7	52.6	146	22	43	62.2

equivalent. The angles are resolved using the $\beta-\theta-M$ relationship. The resulting two equations, Eqs. 3.6 and 3.7, were solved iteratively to determine the minimum deflection angle and associated shock angle.

$$\frac{h+h_t}{2\tan\beta} = x - \frac{h-h_t}{2\tan\theta} \tag{3.6}$$

$$\tan\theta = 2\cot\beta\left[\frac{M_1^2\sin^2\beta - 1}{M_1^2\left(\gamma+\cos 2\beta\right)+2}\right] \tag{3.7}$$

The maximum turning angle is given by Eq. 3.7. It is simply the maximum turning angle for a give Mach number such that an attached shock exists. The initial diffuser turning angle is chosen so that the inviscid oblique shock hits halfway downstream of the diffuser throat. This is a conservative measure to guarantee the oblique shock intersects the top of the throat when interactions are considered. The final dimensions of the diffuser are found in Table 3.2.3. For the initial design the upstream and downstream angles are equivalent and the upper and lower diffuser plates are identical. The diffuser geometry and shock angle is shown schematically in Figure 3.8

The design of the 2-D oblique shock diffuser is depicted in Figure 3.7. The design features a chassis with interchangeable diffuser plates. The diffuser was designed to be installed in existing tunnel hardware with minimal modification. The assembly is

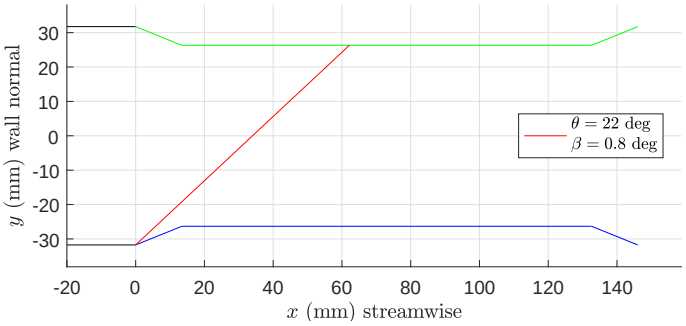

Figure 3.8: Matlab schematic of oblique shock diffuser with inviscid shock solution

housed in the vacuum tank butterfly valve at the end of the test section. The chassis mounts to the last test cell flange by four additional threaded holes machined. The maximum length of the diffuser was determined by the position of the butterfly valve. The vertical line in Figure 3.7 represents the end of the butterfly plate in the vacuum valve when the valve is fully open and shows an 11 mm clearance. Interchangeable diffuser plates on top and bottom to facilitate design iterations of second throat dimensions and diffuser angles. Installation of shims ensures smooth transition from the test cell duct.

3.3 Tunnel 9

The AEDC Hypervelocity Wind Tunnel No. 9 (Tunnel 9) is a large scale nitrogen gas blowdown hypersonic wind tunnel located in Silver Spring, MD and is depicted in Figure 3.9. Tunnel 9 is unique in its capacity to generate high Reynolds number hypersonic flows for a long duration due to high reservoir pressure and temperature, P_0 up to 1,400 atm and T_0 up to 1900 K. The 1.52 m diameter, 3.66 m long test section enables testing of large-scale models. Optical access for measurement

techniques is available at four streamwise locations on the top and sides of the test section. The experiments performed for this dissertation were conducted with the tunnel in the Mach 10 configuration with a Reynolds number of 15.7×10^6/m yielding a good flow run time of 0.9 seconds. A detailed description of the facility, measurement capabilities and run conditions can be found in Lafferty et al.[2]. Table 3.4 shows the nominal freestream parameters for this condition as calculated from tunnel sensors.

Table 3.4: AEDC tunnel 9 nominal flow conditions

M	$Re_{1/m}$ $(1/m)$	u_∞ (m/s)	p_∞ (kPa)	T_∞ (K)	ρ_∞ (kg/m^3)
9.87	15.7×10^6	1467	0.62	53	0.040

Mean velocities were ensemble averaged over all image pairs and over a streamwise distance on the order of 0.5δ for a total of about $7,500$ realizations at each y/δ. Wall conditions, p_w, T_w, and Q_w, are measured using pressure taps and coaxial thermocouples located at the same streamwise location. An iterative process is used to calculate the freestream conditions from the reservoir pressure, temperature, and Pitot pressure. Using this method, the calculated freestream pressure was approximately 20-40% less than the measured wall pressure instead of roughly 6% which is expected for hypersonic turbulent boundary layers. The decrease in calculated freestream pressure is attributed to a reduction in the freestream Mach number due to an isentropic compression or weak oblique shock wave. Calculating the resultant Mach number for both interactions leads to almost identical results. Assuming the wall pressure is accurate and 6% higher than the freestream ($p_2 = 0.94p_w$), the

(a) Photograph of Tunnel 9 nozzle and test cell, man at the optical viewing system shown for size comparison.

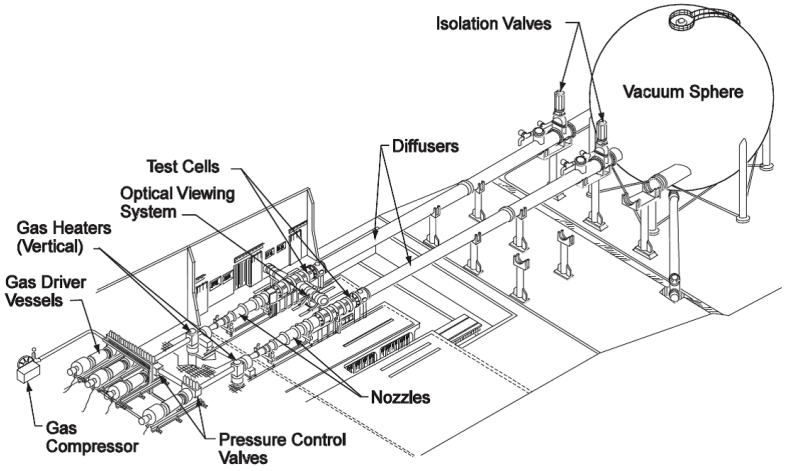

(b) Schematic of showing the relative size of the test cell to the Tunnel 9 Facility.

Figure 3.9: Photograph and Schematic of Tunnel 9 Test Facility

Mach number was recalculated as $M = 9.42$ after the interaction. The remaining freestream conditions calculated based on this adjustment are listed in Table 6.1.

3.4 Hollow Cylinder Flare Test Article

PIV was demonstrated in Tunnel 9 on a large hollow cylinder flare (HCF) test article. Figure 3.10 shows the HCF installed in the Tunnel 9 test section. I designed

the HCF to establish the flow regions for this study and to provide the required infrastructure for the application of PIV. The cylinder body has a 229 mm outer diameter and a 172 mm inner diameter. It extends 1.98 m from the leading edge to a 34° compression corner, then flares out to a diameter of 381 mm. The long length was designed to generate a thick ∼25 mm turbulent boundary layer along the cylinder body at the measurement location located 1.82 m downstream of the leading edge.

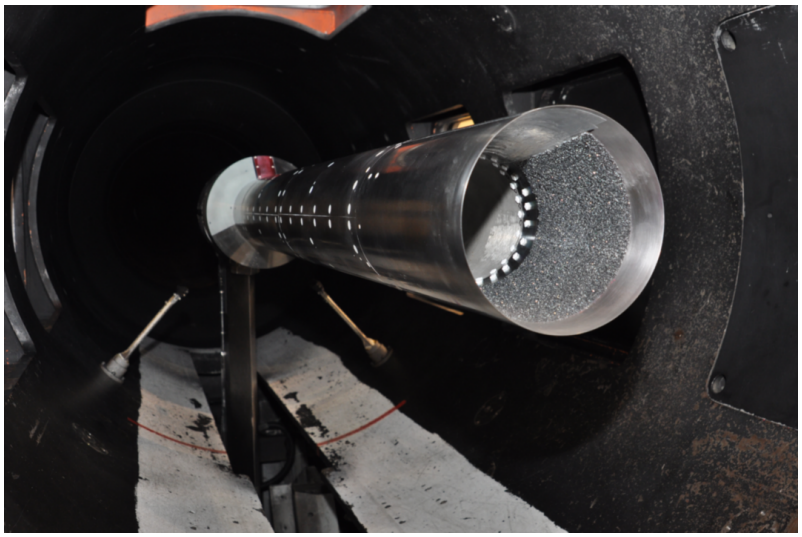

Figure 3.10: Photograph of HCF in Tunnel 9 Test Section

The real intricacies of the HCF design lie under the outer mold line (OML) surface. The main difficulty is delivering seeding particles to the local injector located at the leading edge of the model. All of this hardware must be packaged within the 28.7 mm wall thickness between the inner and outer mold lines. After many construction concepts I decided on a body on frame style support system. The main structure of the HCF is a standard pipe with a 171 mm inner diameter and a 197 outer diameter. The inner surface of the pipe (and therefore HCF) was left as the stock

finish. Precision surfaces were cut into the inner pipe to constrain support ribs for the OML panels. The cylinder surface consisted of two sets of half round 6.35 mm thick stainless steel panels. These panels overlapped 38 mm to form a metal on metal seal to protect the panels against a pressure differential. The flare was machined as a single piece due to the complexity of joining two halves. The leading edge was similarly machined as a single piece with a cutout for the seeding hardware.

This design only left 9.5 mm raceway between the inner support pipe and the OML panels through which to route all the seeding supply tubing and sensor wires. The main seeding supply tubing consisted of four 10 mm stainless steel pipe which ran along the top of the HCF. A flat cutout along the top surface of the inner support tube allowed a larger pipe diameter to reduce diffusional loss of particles to the supply tubing wall. These tubes supplied seeding particles to the injector plenum (reservoir) located in the leading edge.

The skin panels allowed for flexibility in locating the 212 surface pressure and temperature sensor installed into the HCF. A line of pressure taps and a line thermocouples were installed streamwise along the HCF body. These were used by other researchers in order to characterize the flow along the HCF including transition and behavior of the STBLI. The bottom side of the flare featured a configurable sensor panel able to be installed in four positions while maintaining a smooth OML. The position is adjustable in order to tune the placement of the high density array of high frequency pressure sensors to the shock separation location. Much consideration went into the feasibility of placing these sensors. The tight clearance between the inner support pipe and the OML panels complicate the implementation of sen-

sors in two ways. First, short sensors were required so that the sensor body and the minimum wire bend radius would clear the inner pipe. Second, the number of communication wires required considerable volume. Ample clearance was added in the raceway by making cutouts in the ribs and flare support.

3.5 PIV setup

3.5.1 Optics, Laser and Post Processing

An Integrated Design Tools (IDT) Os-10 high-speed complementary metal-oxide-semiconductor (CMOS) camera was used for particle imaging. The camera was selected due to the fast interframe time of 200 ns required for Tunnel 9 conditions. This camera also has notable benefits for PIV, namely the small $4.67 \times 4.67\,\mu\text{m}^2$ pixels, 12 bit pixel depth, and high 3840×2400 px^2 (9.2 Mpx) resolution [57].

The light sheet was produced with a Litron LPY 703-200 PIV laser, outputting a pair of 50 mJ, 10-12 ns pulses at 200 Hz [58]. This laser has a built-in attenuator which was used to reduce the laser energy to a level necessary for PIV. The Os-10 internal clock controlled the 200 Hz timing between laser pair events. A sync-out pulse from the camera triggered a Stanford Research Systems Inc. Model DG 535 pulse generator, which controlled the laser pulse separation timing. The pulse separation time was verified using a photo diode.

The M3CT Station 3 local seeding data was acquired early in the PIV development at AEDC using a former camera and laser. The camera was an Integrated Design Tools (IDT) Y-7 PIV Edition High-Speed Camera. This camera has a 1920 x 1080

px^2 (2.0 Mpx) image array of $7.24 \times 7.24\,\mu m^2$ pixels, 8 bit pixel depth, and a 300 ns minimum interframe time [59]. The laser was a New Wave Research Gemini 200-15 Nd-YAG laser, capable of outputting a pair of 200 mJ, 3-5 ns pulses at 15 Hz [60]. Initially, the laser power was attenuated down to 16 mJ by decreasing the Q-switch delay time. However, this was found to increase laser jitter and subsequently increase the uncertainty in the pulse separation time. Similar findings were reported by Williams [61]. Instead, for the experiments presented in this dissertation, the laser power was attenuated by using a polarizing plate and beam splitter. The internal synchronization of the IDT camera controlled laser and camera timing.

The comparisons between cameras are considered valid as the camera has been shown to not appreciably affect the measurements. Figure 3.11 compares the effect of the camera on the turbulence statistics for the M3CT at Station 2 using global seeding. The starred terms in Figure 3.11 are defined the same was as in Section 2.2.7

There is negligible differences in the profiles except for $y/\delta < 0.2$. Near the wall, the differences in the profiles may be attributed to the development of improved laser reflection mitigation coinciding with the time the camera was switched to the Os-10 rather than an effect of the cameras. In addition, there are large velocity gradients in the near wall region. There may be increased measurement error near the wall due to the lower resolution of the Y-7 compared to the Os-10. For a better comparison between local and global injection, the global data for Station 3 of the M3CT was also acquired using the Y-7 camera, although the higher repetition rate Litron laser was used.

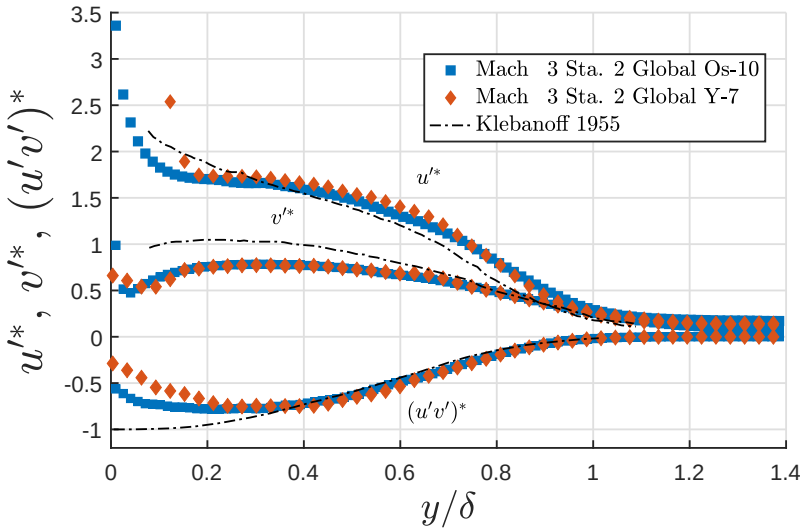

Figure 3.11: Morkovin scaled turbulence statistics comparing camera effects for the M3CT Station 2 using global seeding. There is little effect on the profiles except near the wall which is attributed to improved reflection mitigation rather than an effect of the camera.

DaVis 8 was used as the image correlation software. A two pass method was used, starting with a large interrogation window size on the first pass and reducing the window size to increase resolution for the second pass. A weight biasing of 4:1 was applied in the streamwise direction since this component is dominant in a turbulent boundary layer. A four pass 3×3 px^2 median and minimum peak ratio post processing filters were used to identify and eliminate erroneous vectors.

3.5.2 M3CT

The PIV layout for the M3CT is shown in Figure 3.12. For the M3CT, the laser sheet propagated vertically from the top of the test section through a window insert. Boundary layer measurements were taken off the bottom wall at Stations 2 and 3. The laser energy was attenuated down to ~16 mJ. The sheet thickness was 0.9 mm at the test section, measured by using a burn pattern. A pulse separation time

of 400 ns was used for the M3CT to allow for larger wall normal displacements. The camera was placed just outside the test section window and was fitted with a Nikon AF Nikkor 24-85 mm f/2.8-4 D macro lens. The lens was used in macro mode with $f = 85$ mm giving a magnification of $M_0 = 0.6{-}0.9$ for Station 2 and $M_0 = 0.4{-}0.5$ for Station 3. Prior to the velocity calculation, the location of the wall was determined within one pixel by visual inspection of the laser reflection. The wall position in the image did not vary perceptibly throughout the run. The velocity correlation started with 256×256 px^2 windows and reduced to 96×96 px^2 windows with 75% overlap on the second pass. For Exp. 2C, the particles displace 17% of the first pass windows and 46% of the second pass at this pulse separation time. The PIV frames yielded over 90% valid vectors for y/δ>0.05.

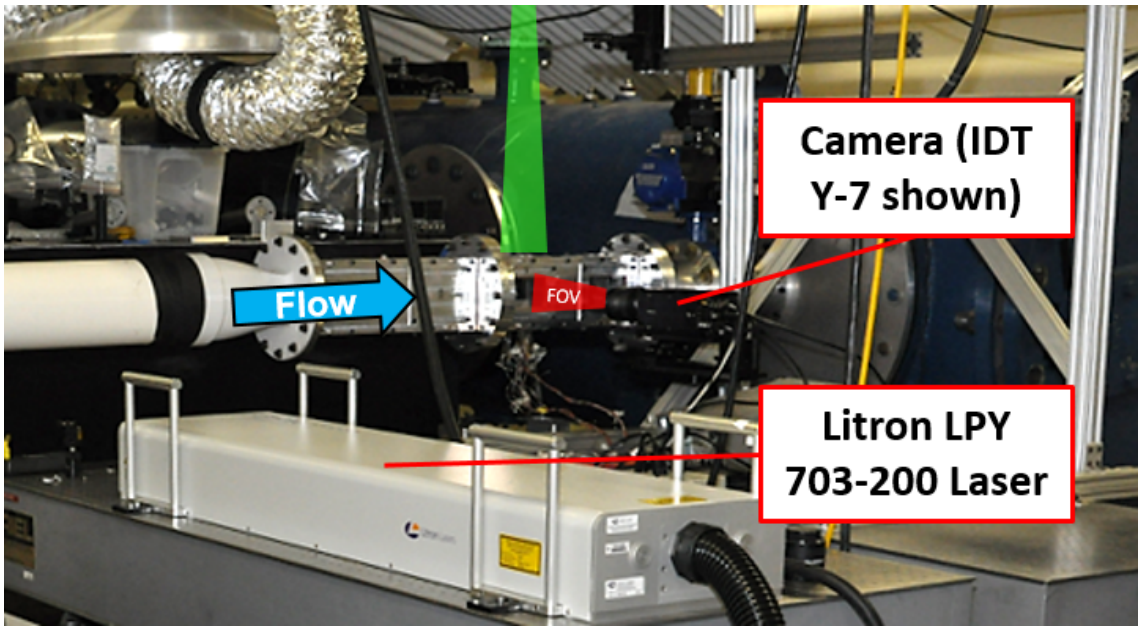

Figure 3.12: PIV setup for the M3CT, with the Y-7 shown at measurement Station 3. The laser enters the test section from the top through a series of turning mirrors and sheet forming optics. The camera is position perpendicular to the sheet.

3.5.3 Tunnel 9

The PIV setup for Tunnel 9 is schematically shown in Figure 3.13. The laser is positioned on top of the test cell and propagated vertically from the top of the test section and was imaged from the side window. The camera is mounted to the side of the test cell and images the flow through a turning mirror. The camera is positioned parallel to the flow in order to avoid collision with other optical measurement systems. The distance from the model to the outside of the test section is approximately 1.5 m. As such, the camera and laser entrance are much further away than for the M3CT. The focusing lens for the laser has a longer focal length causing a wider spread and a slightly thicker sheet of 1.2 mm. The camera was fitted with a Nikon AF Nikkor 200-400 mm f/4 G lens. The focal length of $f = 300$ was necessary for the standoff distance and a 35 mm extension tube was used to increase the magnification to $M_0 = 0.25$. Because of the larger standoff distance and thicker light sheet, the laser was not attenuated. The velocity correlation started with 256×256 px^2 windows and reduced to 64×64 px^2 windows with 50% overlap on the second pass. In the freestream, particles displace approximately 0.3 mm which correlates to 16 pixels for the TBL magnification, $M_0 = 0.25$.

3.6 Wall Reflection Mitigation

Two methods were employed to reduce wall reflections from laser glare in order to obtain near wall measurements. The first method simply uses a clear polycarbonate of acrylic insert. This increases light transmission and therefore decreases surface

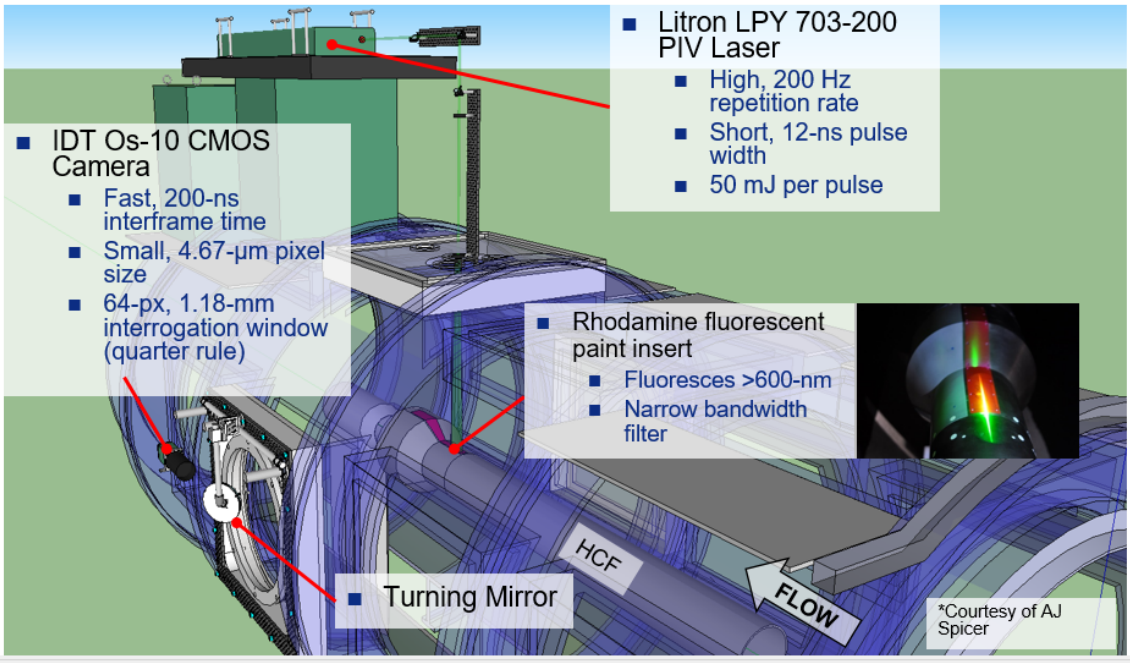

Figure 3.13: Schematic of PIV setup for Tunnel 9. The laser is positioned on top of the test cell and enters top. The camera is mounted to the side of the test cell and images the flow through a turning mirror.

reflections. This method is not applicable in Tunnel 9 because polycarbonate would overheat due to it's low thermal conductivity and the large heath transfer rates from the Mach 10 flow. Also, the laser would still reflect off components below the surface such as the internal frame structure or sensors hardware.

The second method consists in applying a thin layer of clear rhodamine doped paint on the model surface. The paint formulation was similar to that of Cadel et al. [62]. The rhodamine paint absorbs the 532 nm laser light and fluoresces at a higher wavelength, > 550 nm. Reflection noise was significantly reduced by using a 532 ± 1.5 nm narrow band pass filter in front of the image array. For the M3CT, this method was not practical since the laser ablated the paint off the aluminum or polycarbonate blank insert over the duration of 2 or 3 runs. However, this paint was applied to

the sides of the polycarbonate insert to remove internal reflections from the tunnel wall (seen through the clear insert). The maximum extent of noise was reduced to 0.05δ, with a few experiment showing no laser reflection noise. The remaining noise was faint and indistinguishable after applying a sliding average subtraction pre-processing filter in DaVis.

The HCF surface impacted by the laser was designed as a removable insert to avoid downtime between runs from repainting the ablated surfaces. This insert can be seen as the purple surface at the top dead center location of the flare in Figure 3.10. Three of these inserts were manufactured so that one could be installed in the model, one could be painted and ready to be installed and the third could be in the process of painting or drying. In practice, one insert could be used in multiple runs before the paint became detrimentally ablated. This longer life could be attributed to the shorter run time of Tunnel 9 compared to the M3CT and the longer focal length lenses reducing the energy density.

Chapter 4: PIV Particles and Injection Methods

4.1 Particle Material and Generation

Polyalphaolefins (PAO 4) oil particles with a viscosity of 4 cSt were used to seed the flow using a TSI Model 9306 six-jet atomizer. Tichenor et al. [8, 33] reported a mean diameter of 0.25 μm for this atomizer. The atomizer output concentration is 4.3×10^6 particles/cc with a maximum flow rate of 72 L/min. Oil droplets were chosen to take advantage of the low density compared to agglomerates of solid particles such as TiO_2 which are typically used for PIV supersonic and hypersonic wind tunnel applications, see Section 2.1. Oil particles are generally avoided due to the risk of evaporation or thermal degradation because of the high stagnation temperatures. This is not an issue for the applications presented here. The stagnation temperature of the M3CT is ambient. Tunnel 9 has very high stagnation temperatures. However, the particles are never exposed to these temperatures due to the local injection and cold wall boundary conditions.

The maximum temperature the particles are exposed to is the maximum temperature in the boundary layer. Figure 4.1 presents the Clausius-Clapeyron plot for dioctyl phthalate (DOP) and PAO 4 including the maximum temperature in the boundary layer for a flat plate, a 7° cone and a 30° cone for Tunnel 9 at Mach 10

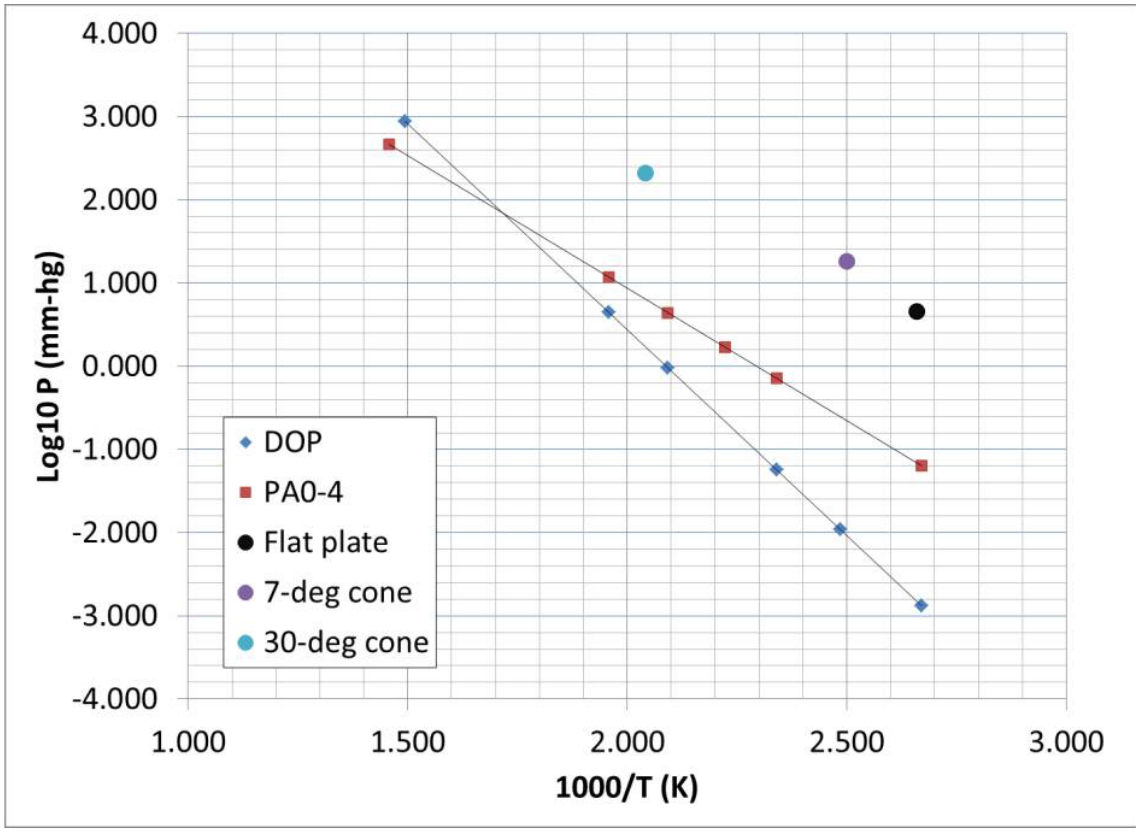

Figure 4.1: Clausius-Clapeyron plot for seeding oils and boundary layer conditions

and a Reynolds number of 15.7×10^6. For all cases, the experimental conditions are significantly above the Clausius-Clapeyron data points such that particle evaporation should not be a problem. PAO 4 will be used as it possesses similar fluid dynamic properties as DOP while not posing a risk as a carcinogen [63]. PAO 4 (also known as oil Emery 3004) has been successfully used in a Mach 6 Ludwieg Tube with seeding injected into the storage tube where the temperature reaches 418 K. [64]

4.2 High-Speed Local Injectors

The design objective of the local seeding injectors is to inject a particle aerosol into a supersonic/hypersonic boundary layer in order to provide an adequate particle density in the downstream measurement section with minimal impact to the flowfield. To achieve this objective, the injectors are designed as converging/diverging supersonic nozzles exiting tangentially to the wall in the direction of flow. Increasing the momentum of the injected aerosol minimizes the effect of the mass injection. The injectors are located far enough upstream of the measurement location that turbulent mixing dampens induced disturbances and distributes particles throughout the boundary layer. The working fluid for the injectors is the aerosol output from the atomizer mentioned in Section 4.1. The mass flow rate required from the atomizer is a function of the throat area of the injectors.

The initial designs were refined using computational fluid dynamics (CFD) solutions performed by the Arnold Engineering Development (AEDC) Aerospace Testing Alliance (ATA) CFD group using the Multiphase Application Program Interface (MAPI). The MAPI is a library of functions that encompass all aspects of a Lagrangian particle tracking simulation including interaction with the gas phase of a computational fluid dynamics (CFD) simulation. MAPI consists of an initialization phase where user input is read and data is initialized, an injection phase where solid or liquid particles are created at injection locations or due to condensation, a physics phase where the particles are influenced by the gas phase to change velocity, temperature, size, etc., and a post-processing phase where the particle state is com-

municated back to the calling program including source terms which can influence the gas phase. Much of the physics phase of the process is based on the KIVA [65] code with modifications implemented in the Wind-US code [66] by Kearsey [67], and Loth and Lee. [68]. MAPI has been incorporated into multiple CFD codes including a Quasi-1D (q1D) solver [69] and the CREATE-AVTM Kestrel framework [70]. For one-way coupling where the particles have minimal influence on the gas phase, the MUltiphase Post-Processing Extraction Tool (MUPPET) is available. MUPPET imports CFD data from choice of several supported CFD codes including Wind-US, Kestrel, and q1D. The gas flow is held fixed based on the final CFD solution and influences the particle through momentum and energy transfer. In the simulations reported here, Wind-US CFD solutions are used within MUPPET to model the oil droplet trajectories from an upstream injection plane into the high speed flow, exiting at the downstream boundary.

The particle mass flow rate was varied to match the atomizer particle concentration in the plenum. These solutions predicted minor flow disturbances, and satisfactory particle uniformity and concentration into the boundary layer.

After designing a nozzle profile to meet the design objectives, one of most challenging aspects of the design is then compressing the profile into the tight spatial envelopes. For the M3CT, the nozzle is housed in a seeding block which takes the place of one of the top/bottom inserts. Figure 4.2 shows the seeding block installed in Station 1 with a computer aided design (CAD) rendered cross-section showing the nozzle profile. For Tunnel 9, the injector block was constrained within the 7° leading edge of the HCF. Figure 4.5 shows a CAD cross-section of the HCF leading edge with

arrows indicating the aerosol flow-path to and through the injector.

4.2.1 M3CT

The M3CT injector is designed to facilitate iterative designs. The entire injector is made from polycarbonate and housed in a custom polycarbonate tunnel insert. The nozzle is a two part assembly of the upper and lower surfaces which are computer numeric controlled (CNC) milled separately (shown as the green and dark blue components in Figure 4.2, respectively). During assembly, a shim is installed into the throat which acts as a stop in order to achieve the tight tolerances without expensive machining capabilities such as electrical discharge machining (EDM). Epoxy was used to seal and join the two halves.

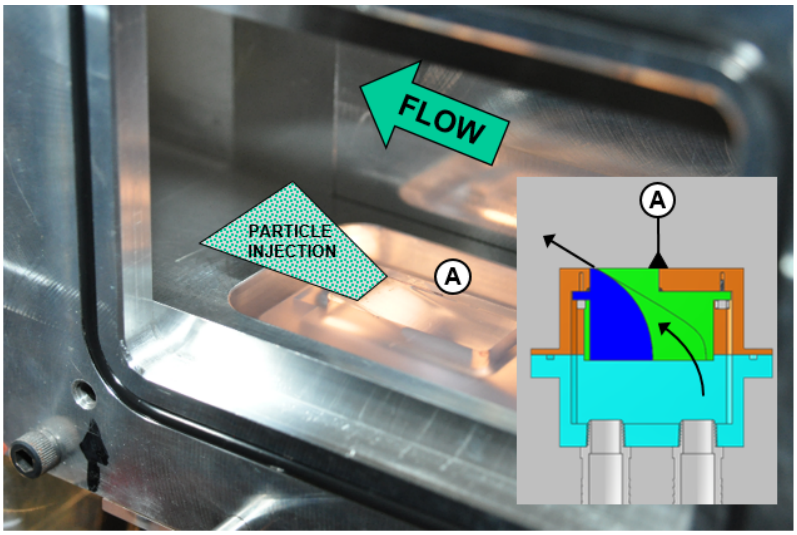

Figure 4.2: M3CT local seeding injector installed into bottom of Station 1, left view. CAD cross-section of the nozzle shown in the lower right corner. Surface A is flush with tunnel wall when installed. Flow is indicated by arrows. Particles are injected from tunnel wall.

The nozzle throat area is 0.08×12.7 mm^2 which corresponds to a volumetric flow rate of 12 L/min, well within the operating envelope of the atomizer. To ensure a

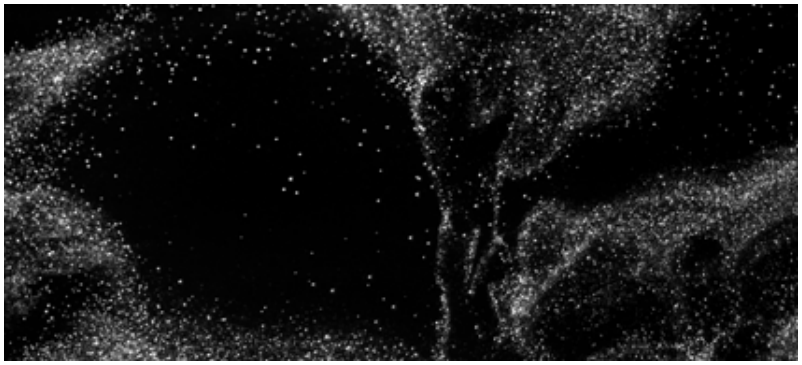

Figure 4.3: Sample PIV image showing the sparse, un-dispersed seeding particles resulting from initial attempts at global seeding. The global seeder was designed to increase seeding uniformity and particle concentration.

sufficient flow rate to the injector, the atomizer was operated at its maximum flow rate. The output of the seeder was connected to a small settling chamber upstream of the nozzle throat (light blue component in Figure 4.2). An atmospheric overflow port exhausted excess aerosol so that the plenum remained at constant pressure.

To assess the effect of the local seeder on the mean flow, a global seeder was developed. The application of global seeding is complicated by the lack of an isolated settling tank for the M3CT. Under designed conditions, ambient room air serves as the upstream reservoir. Initial attempts at global seeding simply involved placing the particle generator upstream of the nozzle inlet and have the particles become entrained in the flow. However, this resulted in distinct structures of highly concentrated un-dispersed seeding particles surrounded by large unseeded regions as seen in Figure 4.3

I designed the global seeder shown in Figure 4.4 to create a sealed isobaric seeded reservoir for the M3CT to increase seeding uniformity and concentration. The concept for the global seeder was developed with the help of Fred Heltsley (AEDC

Tenn). The reservoir consists of a thin walled pallet sized (1.4×1.1×2.5 m^3) plastic bag positioned vertically with the opening facing down. Particles were first injected into the reservoir. Then, an air pump was used to evenly mix the particles and inflate the bag to the volume necessary for a run. Particle concentration in the reservoir was controlled by the operating time for the particle atomizer during injection. The reservoir concentration was determined based on experience to maintain a high concentration of particles in the image. Rings connected to the pallet bag are constrained to vertically running wire ropes to control the bag deformation as its content empties (similar to a bellows).

The plumbing was sized by a combination of recommendations by Pope and Goin [56] and available commercial components to reduce head loss, and avoid the introduction of turbulence and temperature gradients. Head loss from the aerosol volume to settling tank was conservatively calculated as 4.1%. Pressure measurements indicated that the actual pressure loss is 1.3%, which is sufficiently low for valid comparison to prior experiments using Pitot probes and schlieren imaging [49]. Plumbing transports the aerosol to the Mach 3 nozzle through the orifice plate (if present), flow straighteners, and a contoured bell nozzle. The reservoir temperatures in Table 3.1 are slightly higher than ambient due to heating from the air pump used to inflate the bag.

Global seeding is also necessary for the low Reynolds number experiments. The orifice plates lower the tunnel reservoir pressure independently from the local injector reservoir pressure which remains at ambient. The relatively larger stagnation pressure of the local injector would increase the disturbances to the flow.

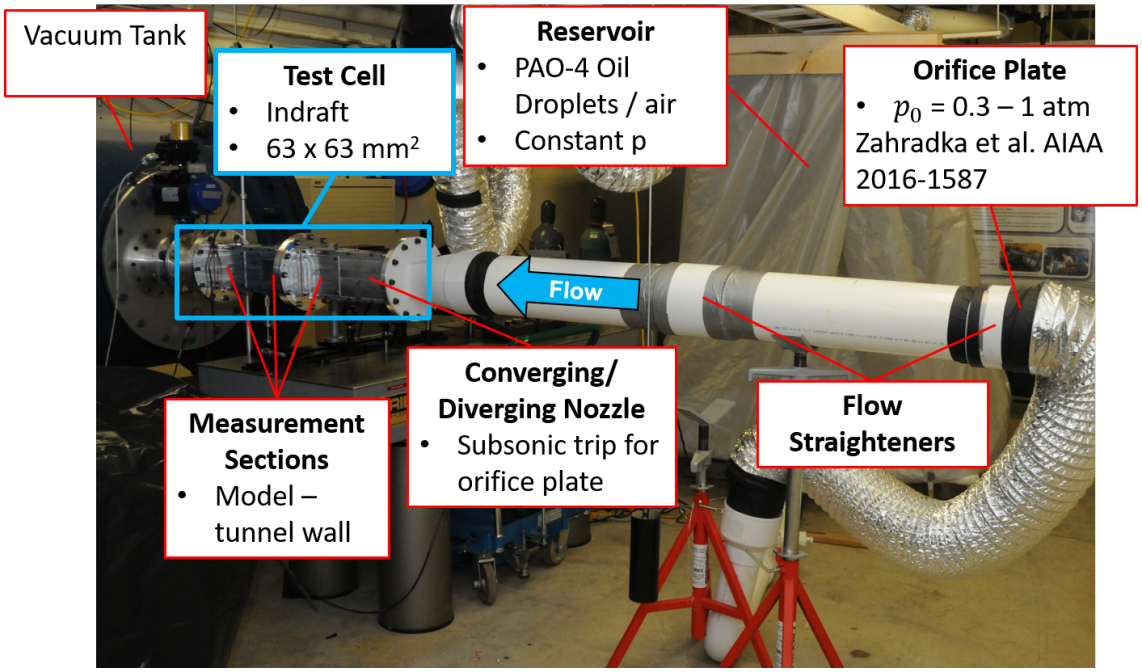

Figure 4.4: M3CT test cell showing the installation of the global seeder, flow direction is indicated by arrow. The collapsible reservoir is not visible as it is behind a safety curtain. Key features are indicated in image text boxes.

4.2.2 Tunnel 9

For Tunnel 9 the injector is integrated into the test article instead of the tunnel infrastructure which is the case for the M3CT. This configuration required additional design consideration. The injector is placed as far upstream in the model as possible in order to maximize the amount of turbulent mixing of the injected aerosol. In order to allow room for the injector, the 7° leading edge angle was locally increased to 20° by means of a protruding housing which is shown as the orange component in Figure 4.5. The difference in the housing angle compared to the rest of the leading edge is shown in Figure 4.6. The lower surface of the housing is co-radial with the HCF inner diameter. This protrusion was deemed to have little impact on the HCF performance since the induced shock would only interact with the unmeasured

internal flow.

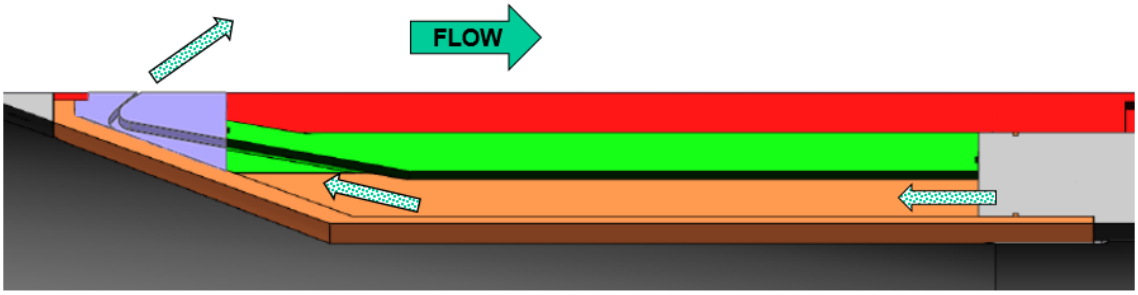

Figure 4.5: CAD cross-section of Mach 10 injector installed in the HCF leading edge. Particle aerosol flow-path is shown by speckled arrows. The aerosol must make a sharp turn in order to inject tangential to the outer mold line of the model. Tunnel flow is indicated by arrow.

The top of the injector body forms part of the HCF OML. As such, the injector including the converging/diverging nozzle is axisymmetric to be concentric with the model. Also, the injector material must be stainless steel to sustain the Tunnel 9 environment. EDM is used to achieve the complex shape and tight tolerances of the nozzle profile. The injector throat area is 0.20×38.1 mm^2 which is much larger than that of the M3CT injector. Two atomizers were used in parallel to satisfy the 94 L/min flow rate. These atomizers were operated at full flow rate with an input pressure of 3 bar and used N_2 as the carrier gas.

The injector located within the model also complicates seeding generation and delivery. The atomizers were located outside of the tunnel. Seeding supply tubing was routed into the test section, up the model support, and through a narrow 10 mm raceway within the model body in order to reach the seeding injector located at the leading edge of the model. The plumbing remained as large as possible (10 mm) to prevent pressure loss and diffusional loss of particles on the tubing walls. Great care was also taken to prevent these tubes from becoming exposed to the flow.

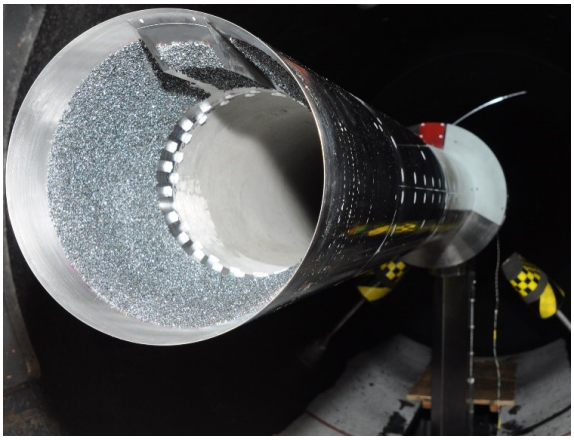

Figure 4.6: HCF leading edge showing protruding injector housing located on the top inside surface of the leading edge. The housing has a 20° angle in contrast to the 7° angle on the rest of the leading edge.

Prior to a run, the Tunnel 9 test section, including the seeding delivery plumbing, is brought to a near vacuum, <2 mm. The atomizers must be initiated prior to the start of the run in order to pressurize the injector reservoir to the target pressure of 1 - 1.5 bar. This time must be known in order to ensure adequate seeding during the run. The plumbing of the local injector is modeled as a control volume (CV) with mass flow in and mass flow out, by means of choked flow orifices at the particle generator and injector throat respectively. The injector reservoir pressure is the CV pressure, which reaches a steady state value based on the atomizer input pressure. The system is governed by the conservation of mass allowing for a change in system pressure and assuming that pressure is constant throughout the system, such that

$$V\frac{d\rho}{dt} = \frac{\dot{m}}{dt} = \dot{m_{in}} - \dot{m_{out}} \tag{4.1}$$

In the absence of the particle generator orifice diameter, a look up table is used to interpolate volumetric flow rate values based on the input pressure, converted to

mass via an assumed ambient temperature. The injector mass flow rate is based on the throat diameter

$$\dot{m} = \frac{p_0 A^*}{\sqrt{T_0}} \sqrt{\frac{\gamma}{R} \left(\frac{2}{\gamma + 1} \right)^{(\gamma+1)/(\gamma-1)}} \tag{4.2}$$

The analysis begins when the particle generator is turned on. Initial conditions of the system are constant pressure of the test section which is near vacuum. The mass flow in remains constant based on the particle generator input pressure, as long as the back pressure ratio remains sustainable. As the pressure begins to rise, the pressure upstream of the outlet mass flow is not high enough to maintain choked flow. Initially, there is a short period where the mass flow is less than choked flow but ill-defined. In my analysis I assume that this is negligible compared to the time it takes to reach steady state. Therefore choked flow is assumed to have been established throughout the analysis time interval.

In order to validate this analysis prior to installation into Tunnel 9, a representative HCF seeding delivery system was produced using the M3CT infrastructure. The injector was represented by using a standard circular chocked flow orifice of equal size, 7.74 mm^2. The 10 mm stainless steel tubing was replaced by equal volume Tygon tubing because the stainless steel tubes were already installed into the HCF. The comparison between the analytical and the M3CT experimental pressure rise is shown in Figure 4.7. The analytical solution agrees better with low pressure M3CT experimental data as shown in Figure 4.7a. The lower pressures of the M3CT and Tunnel 9 at an input pressure of 3 bar are attributed to head loss in the

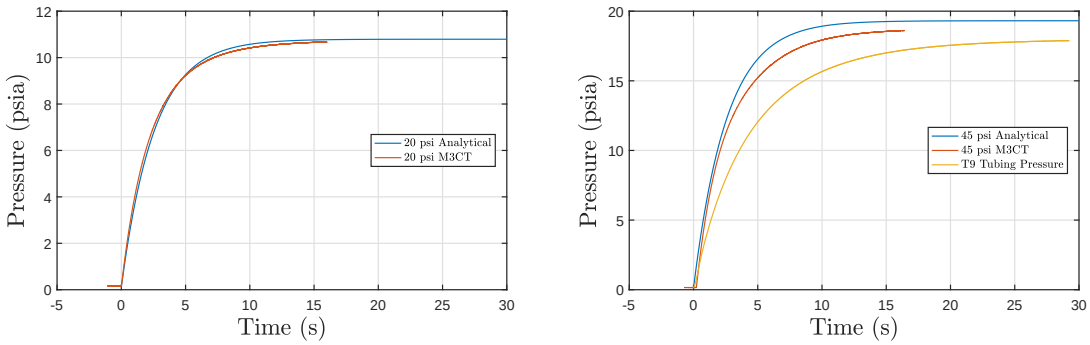

(a) 20 psi (b) 45 psi

Figure 4.7: Pressure rise of seeding supply volume as a function of time comparing the analytical solution to measurements in the M3CT and Tunnel 9. The analytical solution agrees well with experiment at low pressures. The larger deviations at 45 psi are attributed to head loss in the supply tubing which is not accounted for in the analytical solution.

supply tubing. The analytical solution must be modified to include spatial pressure differentials along the tubing to increase the agreement. This level of detail is outside the scope of the pressure rise analysis. The objective of this analysis is to obtain an approximate time until the system reaches steady state. A safety factor is added to the rise time to ensure steady state is reached prior to the tunnel start.

The atomizer valve was opened about 20 seconds before the run so that the system pressure reaches steady state prior to the good flow. The measured steady-state injector reservoir pressure was 17.9 psi which is slightly lower than the expected value, attributed to pressure loss in the tubing, but still within the target range.

4.3 Particle Response

The most crucial features of PIV particles are the ability to follow the flow and the ability to scatter enough light for image acquisition. These attributes are inversely proportional and both are functions of the particle diameter. Short particle response

times are critical for accurate tracking of high-speed flows. Particle response time relative to the flow is quantified through the Stokes number. The Stokes number must be sufficiently small for accurate particle tracking

$$St = \frac{\tau_p}{\tau_f} < 1. \tag{4.3}$$

In this definition, the flow characteristic time is defined as

$$\tau_f = \frac{\delta}{u_e}. \tag{4.4}$$

Assuming Stokes flow and a particle density much greater than the flow density, the particle response time can be expressed as [71]

$$\tau_p = \left(\frac{d_p^2 \rho_p}{18\mu}\right)(f_{Kn}), \tag{4.5}$$

The correction term f_{Kn} accounts for rarefaction effects [72] and takes the form

$$f_{Kn} = 1 + Kn_p\left(c_1 + c_2\left(e^{\frac{c_3}{Kn_p}}\right)\right), \tag{4.6}$$

where the Knudsen number is

$$Kn_p = \sqrt{\frac{\pi\gamma}{2}}\left(\frac{M_p}{Re_p}\right) \sim \frac{1}{\rho}, \tag{4.7}$$

and the coefficients are $c_1 = 2.514$ $c_2 = 0.8$ $c_3 = -0.55$. In hypersonic flows, the

value of the particle Knudsen number is typically large which significantly increases the particle response time compared to continuum flow, see Williams [61]. For the Tunnel 9 HCF test condition, the particle response time increases by approximately one order of magnitude.

For heavy particles at a low particle Reynolds number, the frequency response of the particles corresponds to a first order low pass filter with a time constant corresponding to the particle response time

$$|H_p|^2 = \left| \frac{1}{1 + i\omega\tau_p} \right|^2 . \tag{4.8}$$

The effective filter implies that the high frequency fluctuations (small scale turbulence) will be attenuated.

DNS studies with particle trajectory simulations for a free shear layer by Samimy and Lele [73] have shown that the velocity error due to the particle relaxation time is proportional to the Stokes number for values of Stokes number up to 1. Note, the Stokes number here is calculated as defined by Eq. 4.3 which is 10 times larger than that published by Samimy and Lele due to the difference in the definition of the flow response time.

The experimental cases were designed assuming the particle diameter of 0.25 μm reported in the atomizer literature. Using this diameter, the Stokes numbers for all nine cases are all >0.5. An oblique shockwave test was performed to verify the particle diameter. An oblique shockwave test is used to measure the particle lag. The flow will respond instantaneously to the shock while particles of higher inertia

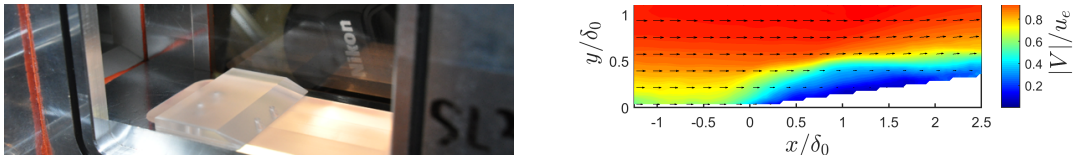

(a) (b)

Figure 4.8: M3CT ramp model. a) 24° ramp shown for physical reference. b) Average velocity magnitude contour plot of 8° ramp flowfield used for the oblique shockwave test.

will have a finite response to the change. Following the work of Melling [74] and Ragni et al. [36], the equation for a spherical particle immersed in a flow results in an exponential decay when the flow is subjected to an abrupt change, such as a shock. The exponent of the decay is the particle response and it describes the system as the velocity of the particle is reduced to that of the surrounding flow, such that

$$\ln(u_n^*) = ln\left(\frac{u_n - u_{n2}}{u_{n1} - u_{n2}}\right) = -Kt = -\frac{t}{\tau_p} \cong -\frac{x_n}{\xi_p} \tag{4.9}$$

The particle relaxation length is calculated at the point where $u_n^* = e^{-1}$. Therefore the relaxation distance ξ_p is related to the particle response time, τ_p by

$$\xi_p = \tau_p \left[u_{n1} - (u_{n1} - u_{n2})e^{-1}\right] \tag{4.10}$$

The particle response time was calculated from the measured shock normal relaxation distance behind an oblique shock wave generated by a 8° ramp shown in Figure 4.8. The shock angle was calculated from the θ-β-M equation. From this the shock normal velocity was calculated. The mean shock normal velocity contour was rotated by the shock angle in order to have rows of shock normal velocity. One row

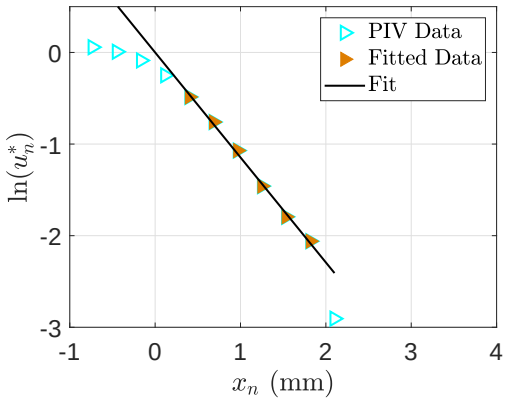

Figure 4.9: One row of shock normal velocities, u_n showing the velocity decay with shock normal distance. A line fit to these data shows the shock location and the particle relaxation distance, where the slope of the line is ξ_p.

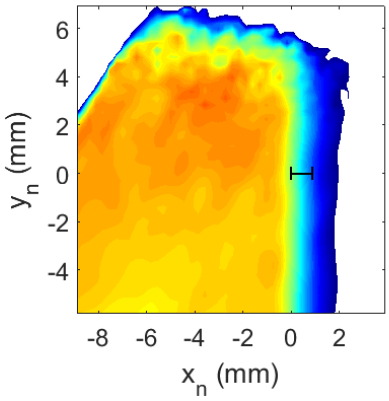

Figure 4.10: Shock normal velocity contour plot in the shock reference frame (shock normal and tangent coordinate system). Black line shows the particle relaxation distance. Notice that the probe row is near the edge of the image frame (top).

in the shock tangent direction was probed and used as a fit to Eq. 4.9. The result is seen in Figure 4.9.

The particle relaxation distance at the point it is calculated is shown with the shock normal velocity in Figure 4.10. The shock normal velocity is plotted in the shock reference frame where normal distance is on the x-axis and tangent distance is the y-axis.

The initial slip velocity after the shock is taken as the difference in the shock normal

velocities upstream and downstream of the shock $u_{n1} - u_{n2}$. The initial slip Mach and Reynolds numbers are calculated based on this initial slip velocity

$$M_{s,0} = \frac{u_{n1} - u_{n2}}{\sqrt{\gamma R T_2}} \tag{4.11}$$

$$Re_{s,0} = \frac{\rho_2 d_p u_{n1} - u_{n2}}{\mu_2} \tag{4.12}$$

where d_p is the particle diameter and the subscript 2 represents fluid properties downstream of the shock.

The particle response time is used to estimate the particle diameter. Assuming Stokes flow and a particle density much greater than the flow density the particle response time can be explicitly solved by using Eq. 4.5. The particle diameter is determined as $d_p \approx 0.5$ μm which is twice the value reported by Tichenor et al. [8, 33]. This causes the Stokes numbers to increase by roughly a factor of 2−2.5. The Stokes numbers for $d_p = 0.5$ μm are listed in Table 3.2.

These particle diameters are calculated assuming that the particle drag does not change with changing velocity and is evaluated at the initial slip velocity $u_{n,1} - u_{n,2}$. In a more recent study, Williams et al. [75] showed that for Mach 7.6 flow this static assumption of the particle drag underestimated the particle diameter by a factor of about 4. Following the study, the particle diameter was also calculated

using a quasi-steady drag solution. The particle response is given by

$$\frac{du}{dt} = -\frac{(u_{n1} - u_{n2})}{\tau_c}, \tag{4.13}$$

where the drag coefficient particle response time

$$\tau_c = \frac{4}{3}\frac{\rho d_p^2}{C_D Re_s \mu_2}. \tag{4.14}$$

The drag coefficient, C_D and the particle slip Reynolds number Re_s are both functions of time. For the experiments in the M3CT, the slip Reynolds number is always less than 45. Therefore only one formulation of the drag coefficient from Loth [72] is used, where

$$C_D = \frac{C_{D,Kn,Re}}{1 + M_s^4} + \frac{M_s^4 C_{D,fm,Re}}{1 + M_s^4}. \tag{4.15}$$

In Equation 4.15

$$C_{D,Kn,Re} = \frac{24}{Re_s}(1 + 0.15 Re_s^{0.687}) f_{Kn} \tag{4.16}$$

$$f_{Kn} = \frac{1}{\left(1 + Kn_p\left(c_1 + c_2\left(e^{\frac{c_3}{Kn_p}}\right)\right)\right)} \tag{4.17}$$

$$C_{D,fm,Re} = \frac{C_{D,fm}}{1 + (C_{D,fm}/1.63 - 1)\sqrt{Re_s/45}} \tag{4.18}$$

$$C_{D,fm} = \frac{(1 + 2s^2)\exp(-s^2)}{s^3\sqrt{\pi}} + \frac{(4s^4 + 4s^2 - 1)\mathrm{erf}(s)}{2s^4} + \frac{2}{3s}\sqrt{\pi} \tag{4.19}$$

$$s \equiv M_s \sqrt{\gamma/2}. \tag{4.20}$$

The quasi-steady particle diameter is found from solving the ODE in Equation 4.13 recalculating the slip Reynolds number, Re_s and Equation 4.15 at each time step. The particle density, $\rho = 817$ kg/m^3 is assumed to be constant. The particle diameter in Equation 4.13 is iterated until $u_n^* = 1/e$, the same criterion used to determine the particle relaxation distance and response time.

The simulated particle response after the shock is shown in Figure 4.11. The quasi-steady drag velocity is obtained from Equation 4.13 using the calculated quasi-steady particle diameter. The static particle diameter velocity is calculated from Equation 4.9 so that

$$u_n = \exp(-t/\tau_p) \tag{4.21}$$

The static solution has very good agreement with the quasi-steady solution. There are slight differences around $0.5\tau_p$ but these are minuscule. I have also calculated the boundary value problem solution to the ODE as a check on the solution method. The iterative solver and the BVP solution have very good agreement.

The reason the static solution is so close to the quasi-steady solution is that the instantaneous particle response, τ_c is nearly constant. Figure 4.12 shows the progression of the drag coefficient, slip Reynolds number, and instantaneous particle response time through the solution of Equation 4.13 normalized by the initial parameters just after the shock. The drag coefficient increases at a similar rate as the decrease in slip Reynolds number. Therefore, Equation 4.14 remains nearly con-

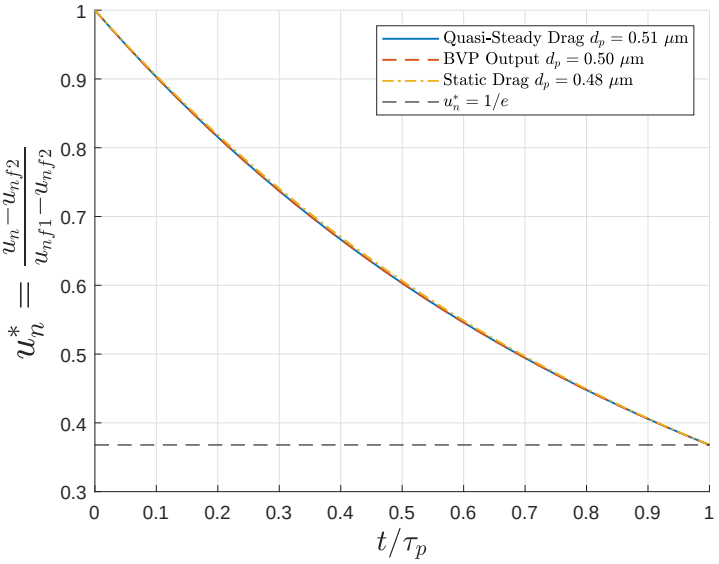

Figure 4.11: Simulated particle response profiles. The simulated constant-drag solution agrees well with the quasi-steady drag solution.

stant. It is interesting that the drag coefficient increases. However, this is predicted by Loth [72] for the M3CT flow regime.

4.4 Particle Concentration

The required seeding gas mass fraction, c_a, needed to achieve a given particle concentration, C, inside the boundary layer can be related to the local flow density, ρ, the particle concentration, C_{inj}, and seeding flow density, $\rho_{p,inj}$ both evaluated at the particle generator exit. The fraction of particles lost between the seeder and the injection point, f_1, also needs to be taken into account. The final expression takes the form

$$C = \frac{(1 - f_1)\,\rho c_a C_{inj}}{\rho_{inj}} \tag{4.22}$$

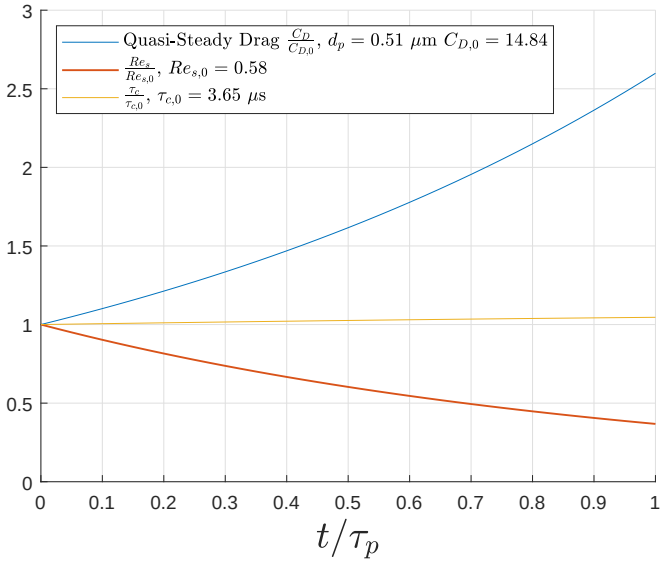

Figure 4.12: Progression of the drag coefficient, slip Reynolds number, and instantaneous particle response time through the solution of Equation 4.13 normalized by the initial parameters. The instantaneous particle response time is nearly constant due to the increasing drag coefficient and decreasing slip Reynolds number.

Eq. 4.22 shows that it is essential for the atomizer to generate high particle concentration in order to minimize the required mass fraction of injected gas inside the boundary as an increase in the injection flow rate is susceptible to increase the disturbances due to the seeding gas. It is also evident that great care must be taken to minimize the losses of particles between the atomizer and injection point. Furthermore, a decrease in the local flow density requires an increase in the local mass fraction of the seeding gas in order to keep a constant particle concentration. Since the particles are injected near the wall, the seeding gas concentration is larger at that location such that a satisfactory particle concentration can be achieved near the wall. This is not the case with a global seeding approach, because the near wall particle concentration is always lower due to the decrease in near wall density. The

mean concentration across the boundary layer can be approximately related to the injector mass flow rate as

$$C \sim \frac{(1 - f_1)\, C_{inj} \dot{V}}{U_\infty \delta W_{inj}} \tag{4.23}$$

Eq. 4.23 can also be used to estimate the required seeding gas flow rate if global seeding is used instead of local seeding. In this case, δW_{inj} is replaced by the cross-sectional area of the test cell corrected for the wall boundary layer displacement thickness. This yields a seeding gas flow rate approximately 2000 times greater for global seeding compared to local seeding. To complicate the matter, the aerosol has to be injected in the reservoir at pressures up to 1.4 bar. These considerations show the impracticality of global seeding for large scale hypersonic wind tunnels.

Accurate measurement of the particle concentration in the measurement section is critical to the development of PIV in Tunnel 9. First, it verifies the image density is appropriate for high density PIV ($10 \leq N_I \leq 25$). Furthermore, the particle concentration is used to validate the accuracy of the particle CFD simulations.

Two methods were used to calculate the particle concentration, thresholding and Gaussian elimination. Both rely on a noise floor below which pixel intensities are not considered for particle identification. This value is selected as three standard deviations over the mean pixel intensity for the measurement region of interest (ROI). Both methods also break the image into 64×64 px^2 interrogation windows in order to calculate the concentration. The image density for this interrogation window is determined by counting the particles and it is related to the concentration through the camera calibration and the laser sheet thickness.

Initially, a thresholding method was used. This method is similar to that used in DaVis 8 to predict the particle density before acquiring images. The image is made binary by assigning all pixels above the noise floor as white and all those below as black. Separated white regions represent particles and are counted to determine the concentration. Figure 4.13a shows the binary image of a sample interrogation window from the Tunnel 9 data set (colors are inverted). The identified particle centers are represented by the red circles superimposed over the binary image. The dimensional concentration calculated using thresholding had good agreement to CFD. However, this method tends to slightly under-predict the CFD. This is assumed because the thresholding method suffers if there are two particles in close proximity. The two are grouped together and counted as one bright spot.

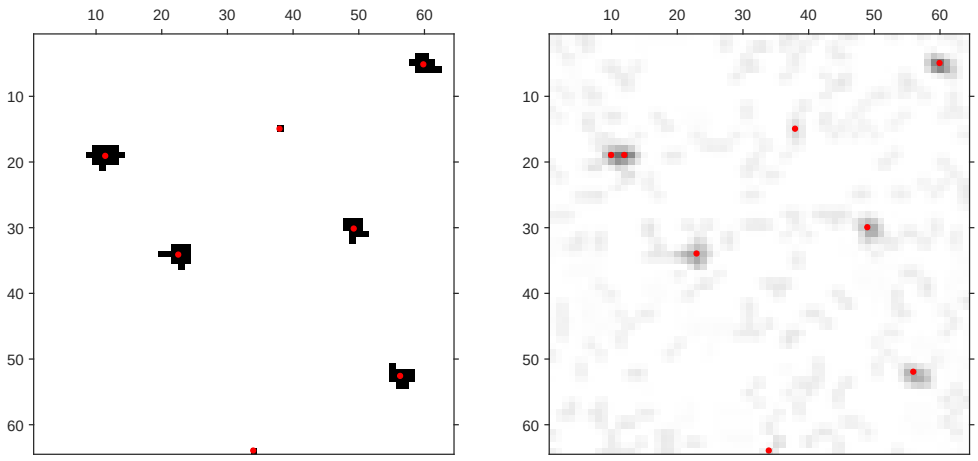

(a) Thresholding method. Binary sample interrogation window is shown with colors inverted.

(b) Gaussian elimination method. Sample interrogation is shown downsampled to 8 bit and colors inverted.

Figure 4.13: Sample particle concentration results comparing the two calculation methods for the same interrogation window. The identified particles are shown as red circles superimposed on the image. Note there are two identified particles at (10,19) and (12,19) for (b) instead of the single particle (11,19) for (a).

I developed a Gaussian elimination method to counteract this effect. Particles are

counted by iteratively identifying and removing the brightest particle in the interrogation window. Figure 4.14 illustrates the process with the same sample interrogation window as Figure 4.13a. The brightest particle in the interrogation window is identified by the highest pixel intensity. A pixel intensity distribution function is used to represent the particle. This distribution is subtracted from the interrogation window to remove the particle. The next highest peak is then identified and the process is iterated until reaching the noise floor. Unique locations of the identified particles are summed for the final count of particles in the window.

PIV imaging systems are diffraction-limited. Light scattered from a point source in an ideal diffraction limited lens has an intensity distribution defined by an Airy function. Adrian and Yao [1] shows that a Gaussian distribution accurately represents the primary peak of particle intensities while ignoring the weaker Airy disks. The distribution of intensities from a single point is given by

$$|\mathrm{h}(s)|^2 \cong |\mathrm{h}(0)|^2 \exp\left(-4\beta^2 \frac{s^2}{d_s^2}\right), \tag{4.24}$$

with $\beta^2 = 3.67$, and $|\mathrm{h}(0)|^2$ is the maximum pixel intensity at the particle center.

For the present data, Eq. 4.24 did not accurately capture the particle intensity distribution. This assumes that the particles are in focus and originate from a point source. If the particles are assumed to be slightly out of focus the representation is too narrow and misses the outer edges of the particles. Instead a Gaussian distribution is fit to the particles intensities so that the distribution function is defined

as

$$I_{i,j} = \frac{1}{\sqrt{2\pi\sigma^2}} \exp\left(-\frac{(x - x_{i,j})^2}{2\sigma^2}\right). \tag{4.25}$$

This greatly increases the computing time. However, it is found to more accurately represent the particle in the image array when verified by eye. Eq. 4.25 is fit to the five pixel intensities in the four orthogonal directions around the peak. The pixel intensity distribution is represented as the Gaussian distribution with the best fit. The particle center is omitted to improve the fit of Eq. 4.25. For a few cases the amplitude is too short in the fitted solution. As such there are multiple instances of the same particle location detected in the count.

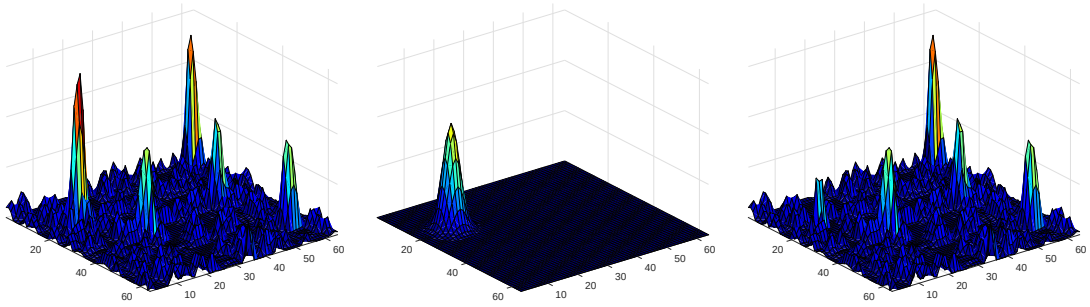

(a) Original particle pixel intensities

(b) Particle Gaussian representation

(c) First particle removed

Figure 4.14: Sequence of Gaussian elimination particle counting. The tallest peak is identified, represented as a fit to a Gaussian distribution of pixel intensities and removed. Then the process repeats for the next tallest peak. Two particles in close proximity can be counted. When the first particle is removed, a second, shorter peak is still detectable.

Figure 4.13b shows an image of the same interrogation window in Figure 4.13a with colors inverted. The superimposed red circles in Figure 4.13b are the particles identified with the Gaussian elimination method. Notice that there are now two particles identified at (10,19) and (12,19) instead of the single particle found by the

thresholding method at (11,19) in Figure 4.13a. The tallest of these two particles is the particle represented in Figure 4.14b. The two particles in close proximity appeared as a single particle through thresholding. But after removing the Gaussian representation of the taller of the two peaks, the second peak was still identifiable in Figure 4.14c although shorter. This makes sense as light scattered off both particles would contribute to the intensities of the overlapping pixels.

Chapter 5: Mach 3 Reduced Reynolds Number Experiments

5.1 Mean Velocity

The law of the wake (2.7) provides an excellent fit to the PIV data. This is evidenced by the adjusted coefficients of determination, $R^2_{adj} \rightarrow 1.0$ for all flow conditions. Figure 5.1 shows the very good fit of Coles's law of the wake to the PIV data with the minimum and maximum Reynolds numbers (Exps. 1A and 3C respectively). The log layer for Exp. 1A is small, $20 \leq y^+ \leq 50$ and data used for the fit, $y^+ > 50$ are entirely in the wake region. The higher Reynolds number of Exp. 3C extends the log layer to $20 \leq y^+ \leq 200$. As such, the fit uses about ~10 data points in the log layer. The fit of Cole's law of the wake yields equally high coefficients of determination, regardless of the different regions of the boundary layer used for the fit.

Figure 5.2 shows the PIV velocity with inner scaling for all nine flow conditions. The data sets are grouped by Reynolds number and separated by an offset of 4 and 8 added to the ordinate for the intermediate and high Reynolds number groups, respectively. The u^+_{vd} scaling collapses the PIV data very well in the log layer. For comparison, the universal log law and Spalding boundary layer equations are plotted in Figures 5.1 and 5.2.

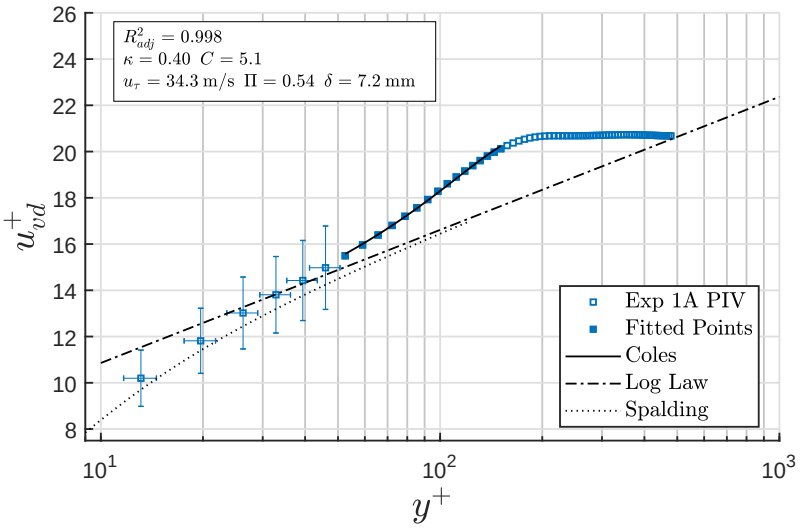

(a) Exp. 1A

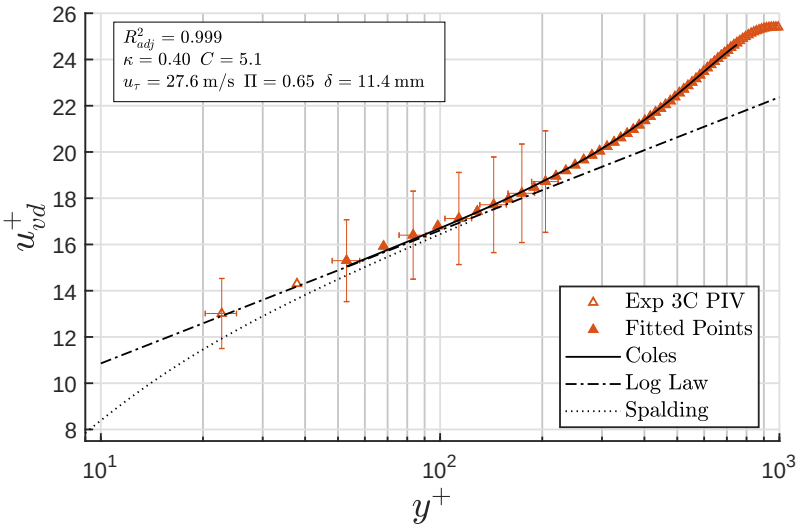

(b) Exp. 3C

Figure 5.1: Inner scaled velocity showing the excellent fit to Coles's law of the wake, Eq. 2.7, for PIV Exps. 1A and 3C. The fitted parameters u_τ, δ_c, and Π are shown in the upper left corner. The fitting region included the log layer and wake region for Exp. 3C and only the wake region for Exp. 1A. Errorbars are shown for points below the wake region.

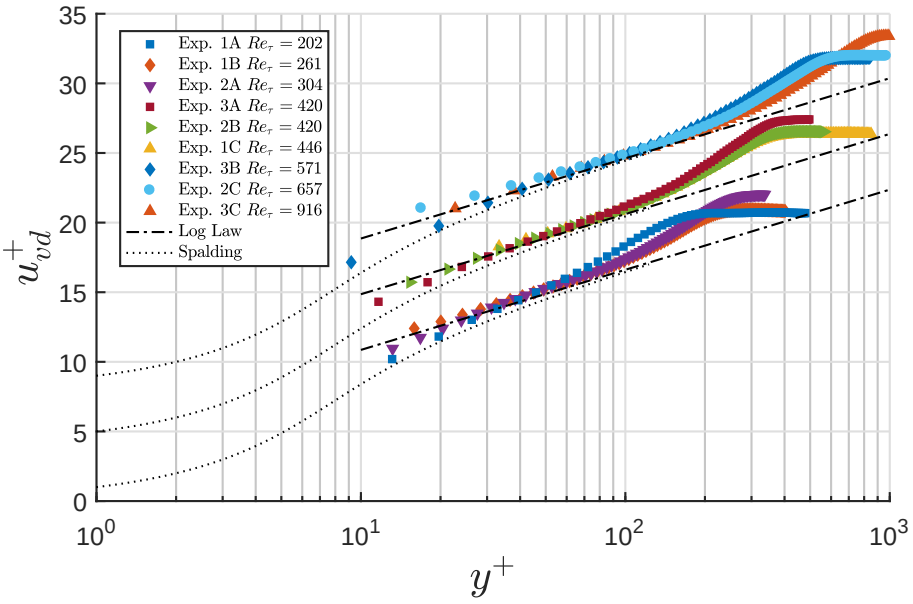

Figure 5.2: Streamwise velocity with inner scaling for all flow conditions. Experiments are grouped by Reynolds number and separated by an offset of 4 and 8 added to the ordinate for the intermediate and high Reynolds number groups. The u^+_{vd} scaling determined by Coles's law of the wake fit collapses the data very well in the log layer. The universal log law, Eq. 2.6, and Spalding, Eq. 2.7, boundary layer equations are shown for comparison.

The skin friction velocity, u_τ, calculated from the fit is within 5% of the van Driest II transformation which is recommended by Hopkins and Inouye [43] for the determination of supersonic and hypersonic skin friction. The boundary layer thickness determined by the fit δ_c is less than the 99.9% boundary layer thickness δ and is closer to the 99% boundary layer thickness δ_{99}. The wake strength parameters, Π, did not follow a Reynolds number dependence as shown by Coles [76] for an equilibrium boundary layer.

The wake strength parameter describes the maximum deviation from the log layer, where

$$\frac{2\Pi}{\kappa} = \frac{u_e^*}{u_\tau} - \left[\frac{1}{\kappa}\log\frac{u_\tau \delta}{\nu_w} + C\right] \tag{5.1}$$

Coles demonstrated that, for an equilibrium boundary layer, $2\Pi/\kappa$ reaches an asymptotic value of 2.75 ($\Pi = 0.55$) for high Reynolds numbers. For $Re_\theta < 6,000$, he shows that $2\Pi/\kappa$ rapidly decays from 2.75 to zero at $Re_\theta = 500$. Although he notes an uncertainty of 5-10% for a 1% uncertainty on the mean velocity. The present wake strength parameters did not decay at low Reynolds numbers and exceeded the asymptotic value at Sta. 3. A number of factors influence the wake strength parameter, outlined by Coles [76] and Fernholz and Finley [77], including upstream history, tripping devices and pressure gradients. Most relevant for the present data is the slight adverse pressure gradient (APG) that exists due to the growth of the boundary layer along the channel. An APG increases the wake strength parameter, see White [78] for an empirical correlation between the wake strength parameter, Π, and the Clauser equilibrium parameter, β. Similarly, a favorable pressure gradient lowers the wake strength parameter, also predicted by White and demonstrated by Tichenor et al. [9]. Lapsa et al. [21] reported similarly high values for Π and attributed the increase to upstream history of the pressure gradient of the nozzle expansion. These parameter appear to be a point of debate in the literature. It requires much more study which is outside of the scope of this dissertation.

5.2 Spatial Resolution

The spatial resolution, defined as

$$SR = \delta / D_I, \tag{5.2}$$

relates the boundary layer thickness to the interrogation window size D_I (in object plane). A high spatial resolution implies a large number of velocity vectors in the boundary layer. The spatial resolution also gives an indication of the extent of spatial averaging of the velocity gradient across the interrogation window.

The spatial resolution was investigated in two ways. First, via vector processing where the camera magnification was held constant and the interrogation window size was varied. Second, optically, where the interrogation window size was held constant and the camera magnification was varied.

5.2.1 Vector Processing

The initial analysis was conducted with a rather coarse interrogation window size (128 px 50% overlap), for computational speed. A second, finer data set (96 px 75% overlap) was computed to increase vector resolution and verify there was no loss of information due to velocity averaging in the coarse interrogation windows. In general, the interrogation window size has little effect on the data, as demonstrated in the fluctuating velocity profiles. The post processing results are similar to Exp 2C, shown in Figure 5.3. The magnitudes of the streamwise and wall-normal fluctuating velocity profiles are slightly lower for the coarse grid compared with the fine grid. The effect is small as the differences are less than 7% which is well within the measurement uncertainties. The lower magnitudes are attributed to spatial averaging of finer scale fluctuations over the larger windows.

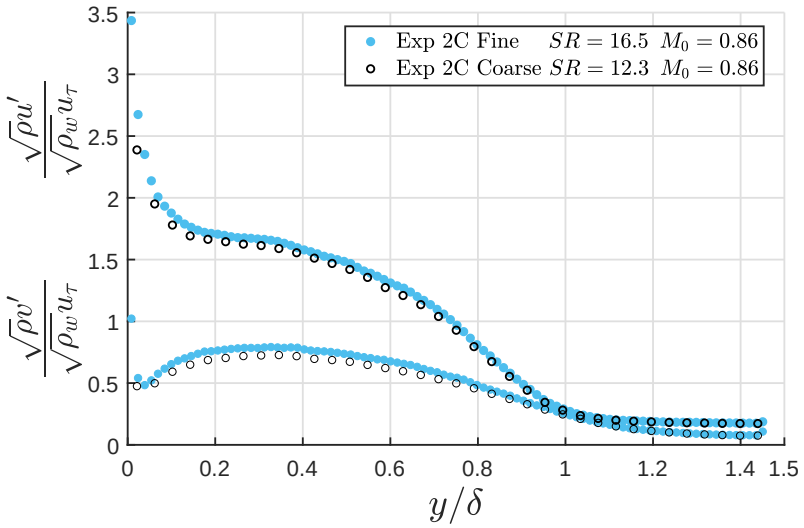

Figure 5.3: Streamwise and wall-normal Morkovin scaled fluctuating velocity profiles comparing the effect of vector processing spatial resolution. There is excellent agreement between the coarse and fine grid resolutions. The coarse grid fluctuating velocity magnitudes are less than the fine but are within 7%.

5.2.2 Magnification

PIV measurements for each of the nine flow conditions were repeated four times with different lens magnifications. All magnifications were processed using 96 px 75% overlapping windows. The data for each flow condition listed in Table 3.2 are selected based on lowest uncertainty (see Sec. 2.2.7) among the camera magnifications, particularly near the wall. The experiment with the highest magnification typically has the lowest uncertainty. Exp. 1A is the exception, where the second highest magnification has the lowest uncertainties.

The streamwise and wall-normal fluctuating velocity magnitudes increase with increasing camera magnification. Figure 5.4 shows the typical trend exemplified by the four experiments for condition Exp. 1B. The reduced magnitudes are attributed to combined effects of decreased spatial averaging, particle image diameter and particle

shift. Contributions of individual effects must be studied further.

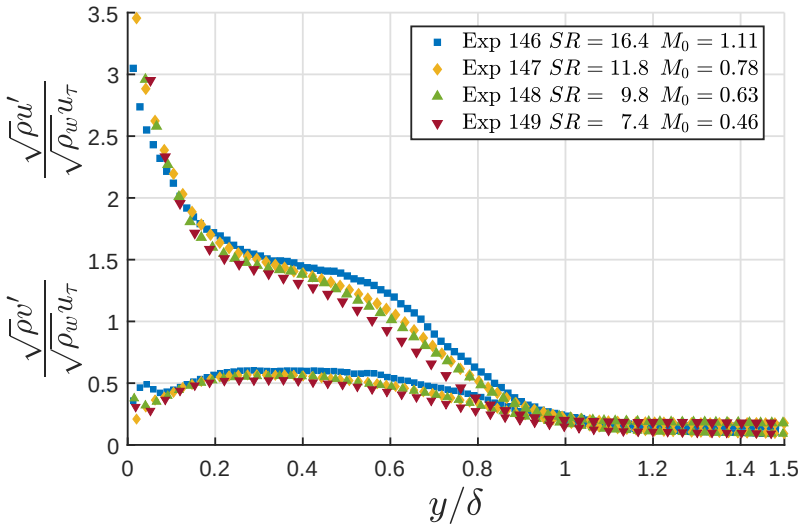

Figure 5.4: Streamwise and wall-normal Morkovin scaled fluctuating velocity profiles showing increasing fluctuating velocity magnitudes with increasing camera magnification. All four experiments have the same conditions as Exp. 1B.

5.3 Velocity Fluctuations and Reynolds Shear Stress

Fluctuating velocity and Reynolds shear stress profiles are compared against experimental data and DNS from the literature listed in Table 6.2. Two outer length scales δ_{999} (represented as δ for brevity) and δ_{99} are used in the comparison literature to normalize the wall-normal distance. It is important to use the same scaling when comparing profiles to visualize trends in the data because δ is approximately 15% larger than δ_{99}. Data from Ekoto et al. [19], Eléna and LaCharme [22], Mustafa et al. [26], Martin [28], and Klebanoff [18] used δ as the length scale. Piponniau [20], Pirozzoli and Bernardini [12], and Duan et al. [29] used δ_{99}. Experimental data from Lapsa et al. [21], at the $x/\delta_0 = 40.0$ measurement location used a boundary layer calculated from a fit of the Coles law of the wake. As mentioned in Section

5.1, δ_c was similar to δ_{99}. Therefore, these data are included on the δ_{99} plot. The data presented in this paper are primarily scaled by δ. The data are rescaled by δ_{99} on a separate plot for comparison. Comparison to the krypton tagging velocimetry (KTV) data from Mustafa et al. [26] is particularly interesting as these data were acquired in the same wind tunnel at Exp 2A conditions.

5.3.1 Streamwise Fluctuating Velocity

Figure 5.5 presents the Morkovin scaled streamwise fluctuating velocity profiles as a function of y/δ for the nine cases listed in Table 3.2. The streamwise fluctuating velocity profiles for $y/\delta > 0.2$ are all within the limits established by Eléna and LaCharme [22] and the standard deviation for the nine experimental cases are within approximately 10%. Exps. 1C and 3C display the same trend but have the largest deviation from the mean. The outer scaling (y/δ) is not expected to collapse the data in the near-wall region ($y/\delta < 0.1$) as demonstrated by Pirozzoli and Bernardini [12]. As seen in the DNS data presented in Figure 5.6b, the outer scaling (y/δ) does not collapse data from varying Reynolds number in the near-wall region ($y/\delta < 0.1$). In addition, the increased deviations near the wall (between 15-25%) could be attributed to higher measurement uncertainty due to large velocity gradients, laser reflection, and lag from increased particle response time.

Figure 5.6a compares the mean of the nine experimental cases to experimental data from the literature and DNS from Martin [28]. Good agreement is seen among the different data sets. Notably, the data from Mustafa et al. [26] has excellent

Table 5.1: Key parameters from comparison literature data

			M_e	Re_τ	Re_θ	H	C_f
Ekoto et al. 2007 [19]		PIV	2.86	∼4,500	60,000	—	—
Eléna and LaCharme. 1988 [22]		LDV	2.32	∼975	4,700	3.47	2.15×10^{-3}
Piponniau 2009 [20]		PIV	2.28	1,080	5,100	3.54	2.00×10^{-3}
Lapsa et al. 2011 [21]		PIV	2.75	717	6,600	1.4	1.90×10^{-3}
Mustafa et al. 2017 [26]		KTV	2.77	∼350	1,750	—	—
Martin 2007 [28]		DNS	2.32	∼700	4,450	—	—
Pirozzoli and	a	DNS	2.00	251	1,122	3.08	3.19×10^{-3}
Bernardini 2011 [12]	b			497	2,377	2.98	2.67×10^{-3}
	c			1,116	6,046	2.91	2.11×10^{-3}
Duan et al. 2011[29]		DNS	2.97	487	3,028	5.09	2.17×10^{-3}

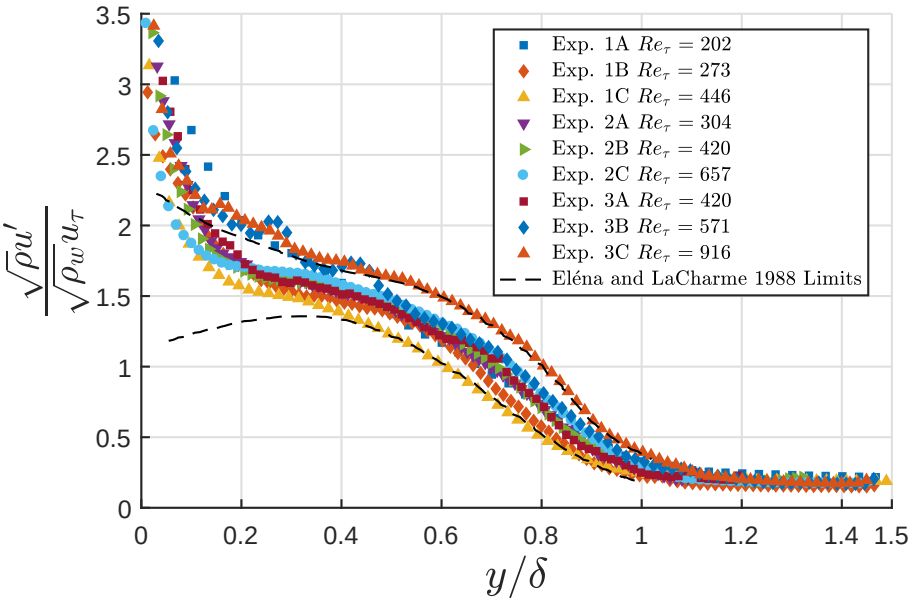

Figure 5.5: Morkovin scaled streamwise fluctuating velocity profiles showing low standard deviation between the nine experimental cases.

agreement with the current PIV experiments.

There is also very good agreement between the PIV data and literature scaled by δ_{99}, as shown in Figure 5.6b. This plot includes DNS data over a wide range of Re_τ from Pirozzoli and Bernardini [12] and Duan et al. [29]. As previously mentioned the outer scaling successfully collapses the DNS away from the near-wall region ($y/\delta > 0.15$).

Figure 5.7 compares the inner scaled DNS data from Pirozzoli and Bernardini [12] to the PIV cases at similar Re_τ. Outside of the viscous sublayer ($y^+ > \sim 10$), the inner scaled wall-normal distance y^+ illustrates the effect of Reynolds number on the streamwise fluctuating velocity. The PIV data are distributed in between the DNS as expected based on the Reynolds number, particularly Exp. 2B. Exp. 1B agrees well with Pirozzoli and Bernardini (a) above $y^+ \approx 100$. Similarly, Exp. 3C has good agreement to Pirozzoli et al. (c) for $y^+ < 300$. The increased deviations

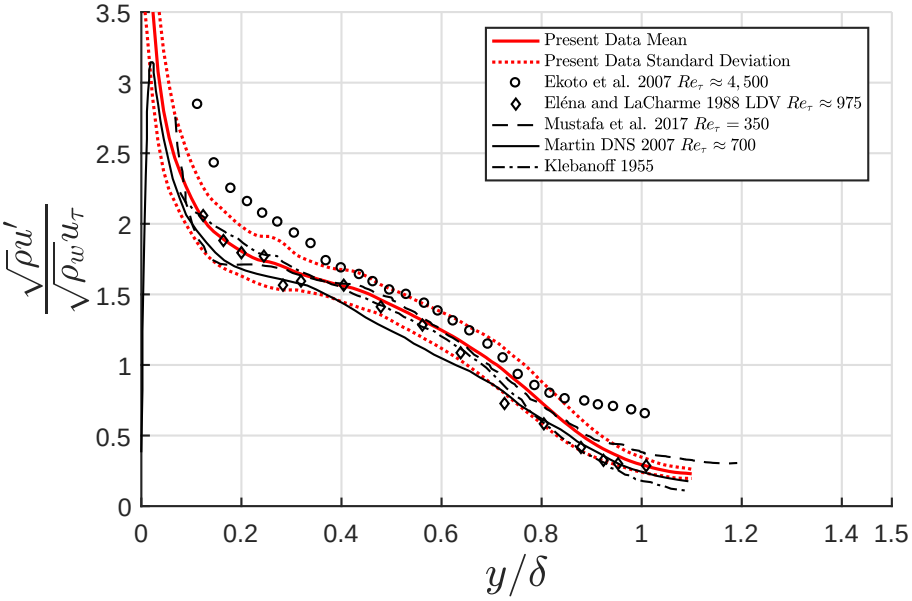

(a) Scaled by δ

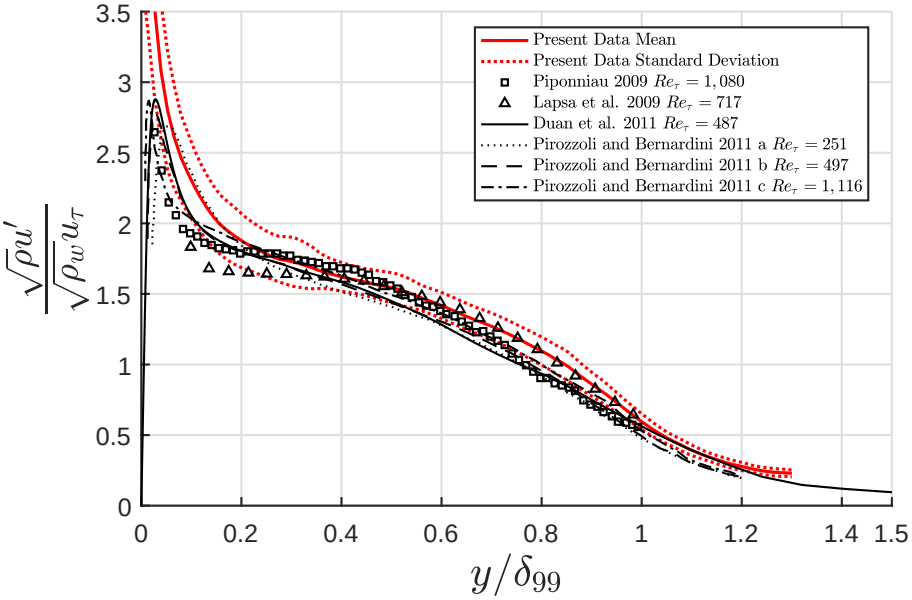

(b) Scaled by δ_{99}

Figure 5.6: Streamwise Morkovin scaled fluctuating velocity profiles compared to experimental and DNS literature data.

between the PIV data and DNS from the literature near the wall ($y^+ < 100$) could be attributed to higher measurement uncertainties, laser reflection, and particle lag.

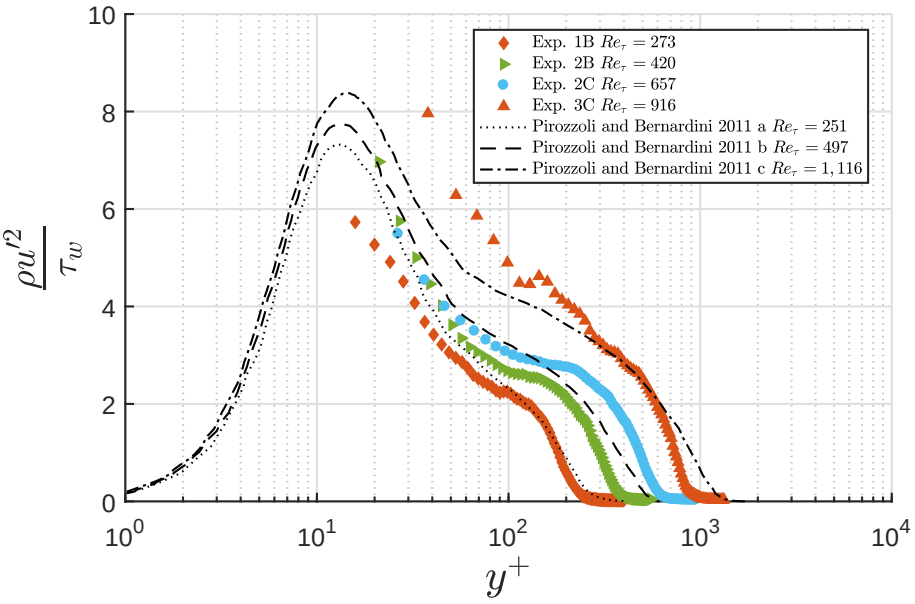

Figure 5.7: Streamwise fluctuating velocity profiles with inner scaling emphasizing effect of Reynolds number. Overall, the PIV data are distributed as expected compared to DNS data from Pirozzoli et al. [12].

5.3.2 Wall Normal Fluctuating Velocity

Figure 5.8 presents the Morkovin scaled wall-normal fluctuating velocity profiles as a function of y/δ for the nine cases listed in Table 3.2. In addition, HWA data from Klebanoff [18] are presented for comparison. The standard deviation is larger (approximately 20%) for the wall-normal component compared to the streamwise component. All cases show lower peak magnitudes than Klebanoff with the mean approximately 30% lower throughout the boundary layer. Exp 3C shows the best agreement with Klebanoff. This experiment has the lowest Stokes number ($St = 0.26$). In contrast, Exp 1A with the largest Stokes number ($St = 1.09$) has the worst

agreement with Klebanoff.

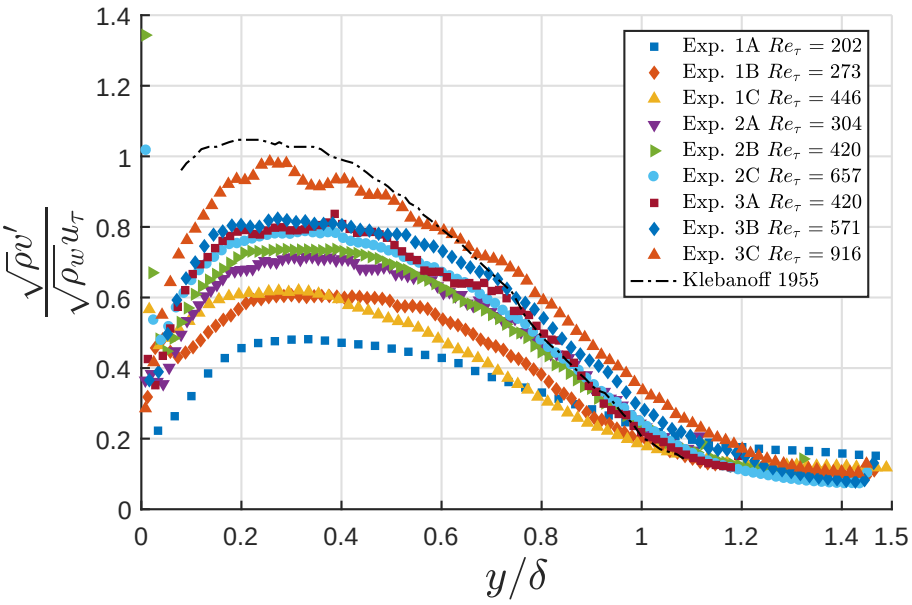

Figure 5.8: Morkovin scaled wall-normal fluctuating velocity profiles showing increased standard deviation between the nine experimental cases compared to the streamwise component.

The effect of the Stokes number on the accuracy of the wall-normal component is investigated in Figure 5.9 which presents the relative error between the nine PIV cases and HWA data from Klebanoff [18] at $y/\delta = 0.2$. The relative error to Klebanoff, $\epsilon(x)$, is defined as

$$\epsilon(x) = \frac{(x)_{Klebanoff} - (x)_{PIV}}{(x)_{Klebanoff}}, \tag{5.3}$$

where in this case (x)=v'. The plot shows a linear increase of the relative error with Stokes number. The linear relationship exists through $y/\delta < 0.9$. Such a trend is not found for the streamwise component. Attenuated values of the wall-normal fluctuating velocity have been attributed to particle lag by Lowe et al. [38], Williams [61], and Brooks et al. [50]. However, prior to the current study, no

detailed study characterizing the effect of the Stokes number on the attenuation of the wall-normal fluctuating velocities has been preformed experimentally. Data points from Piponniau and Lapsa et al. are also included in Figure 5.9. In order to compare to Klebanoff, the y/δ_{99} profiles were scaled by 85% which is the average decrease from δ to δ_{99} in the current data. These points display a similar trend as the current data, although are not included for the determination of the linear trend line.

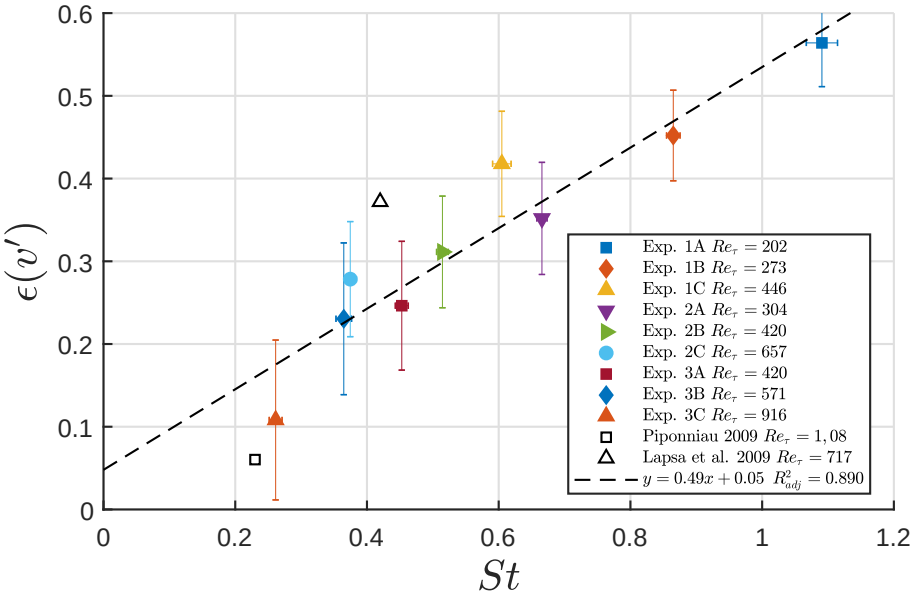

Figure 5.9: Relative error in wall-normal Morkovin scaled fluctuating velocity between the nine PIV cases and Klebanoff HWA data [18] at $y/\delta = 0.2$. There is a linear trend with the Stokes number. Particle lag was shown to reduce the v' magnitude by Lowe et al. [38], Williams [61], and Brooks et al. [50].

Figure 5.10 compares the mean of the nine experimental cases to experimental data and DNS from the literature. In Figure 5.10a, the mean values are approximately 30% lower than the HWA data from Klebanoff [18] and the DNS from the literature. As for the streamwise component, the DNS from Pirozzoli and Bernardini [12] show that the outer scaling successfully collapses the wall-normal component away from

the near-wall region ($y/\delta > 0.15$). This collapse strengthens the notion that the large standard deviation in the wall-normal fluctuations among the nine experimental cases is indeed due to the large range of Stokes numbers. The effect of the Stokes number is also displayed in PIV data from Piponniau [20] and Lapsa et al. [21]. Piponniau reports a Stokes number of $St = 0.23$ whereas Lapsa et al. have a Stokes number of $St = 0.42$. The higher Stokes number from Lapsa et al. has the same effect on the fluctuating velocity magnitudes as the current data. Furthermore, the closest matching Stokes number cases, Exp. 3C with $St = 0.26$ and Exp. 2C with $St = 0.37$, are included in Figure 5.10b. There is excellent agreement between PIV data with similar Stokes numbers.

5.3.3 Reynolds Shear Stress

Figure 6.4c presents the Morkovin scaled Reynolds shear stress profiles as a function of y/δ for the nine cases listed in Table 3.2. Again, the HWA data from Klebanoff [18] are presented for comparison. The standard deviation of the nine cases is approximately 25% which is slightly higher than the wall-normal fluctuating velocity. However, the mean values agree better with the Klebanoff data. The mean stress at $y/\delta = 0.2$ is approximately 20% lower than Klebanoff.

Figure 5.12 shows the relative error between the nine PIV cases and HWA data from Klebanoff at $y/\delta = 0.2$. Experiment 3C is excluded from this plot. The amount of amplification in Exp 3C may indicate increased noise and not accurately represent the effect of the particle response. The Reynolds stress profiles do not

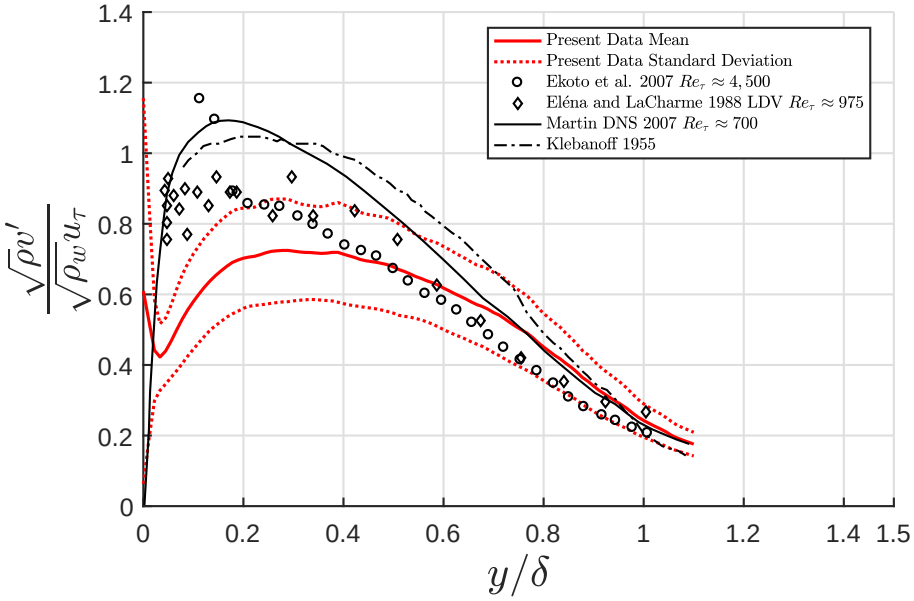

(a) Scaled by δ

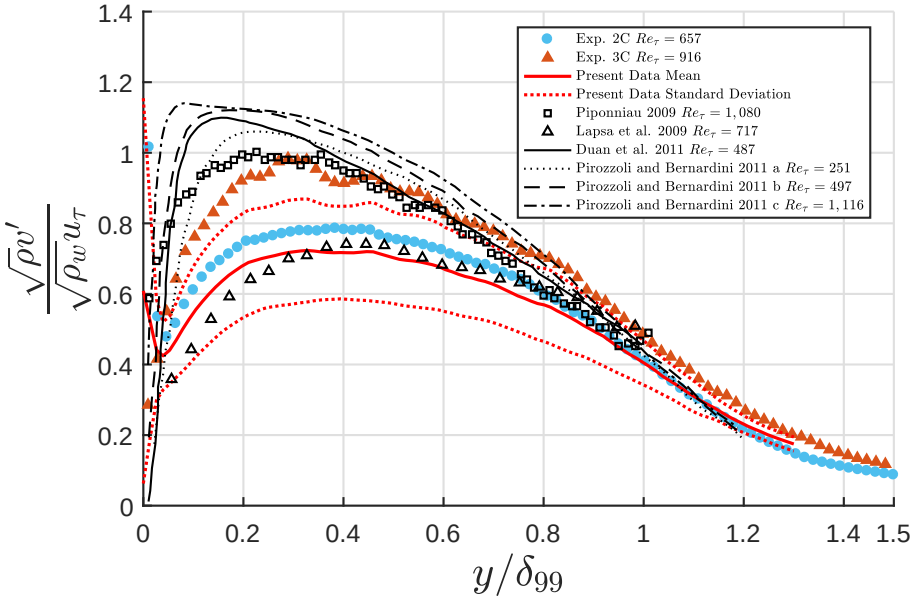

(b) Scaled by δ_{99}

Figure 5.10: Wall-normal Morkovin scaled fluctuating velocity profiles compared to experimental and DNS literature data.

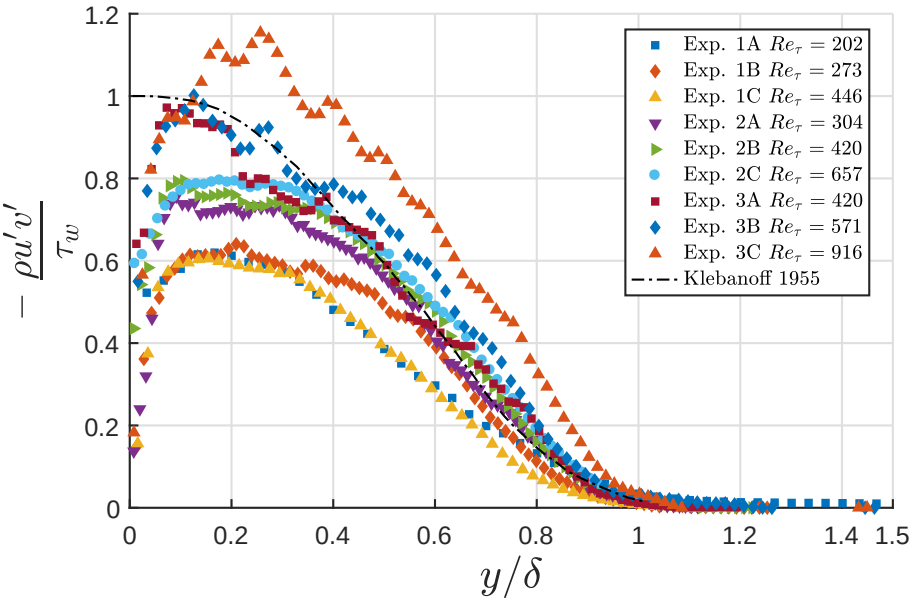

Figure 5.11: Morkovin scaled Reynolds shear stress comparing flow conditions and Klebanoff [18] data.

exhibit as strong of a dependence on Stokes number as the wall-normal fluctuating velocity. There is still a visible trend but the coefficient of determination is lower for the Reynolds stress than for the wall-normal component. In addition, the linear relationship exists only for $y/\delta < 0.4$. The reason for the abnormally high error in Exp. 1C is unknown. The relationship could be complicated by the fact that the Reynolds stress is the product of u' which is insensitive to the Stokes number and v' which is sensitive.

Figure 5.13 compares the mean of the nine experimental cases to experimental data and DNS from the literature. The agreement with experimental data from the literature shown in Figure 5.13a is assumed coincidental as these profiles are consistently lower than the DNS throughout the boundary layer. In Figure 5.13b, the mean Reynolds stress shows good agreement with DNS data from the literature and experimental data from Piponniau [20] for $y/\delta > 0.5$. As the wall is approached,

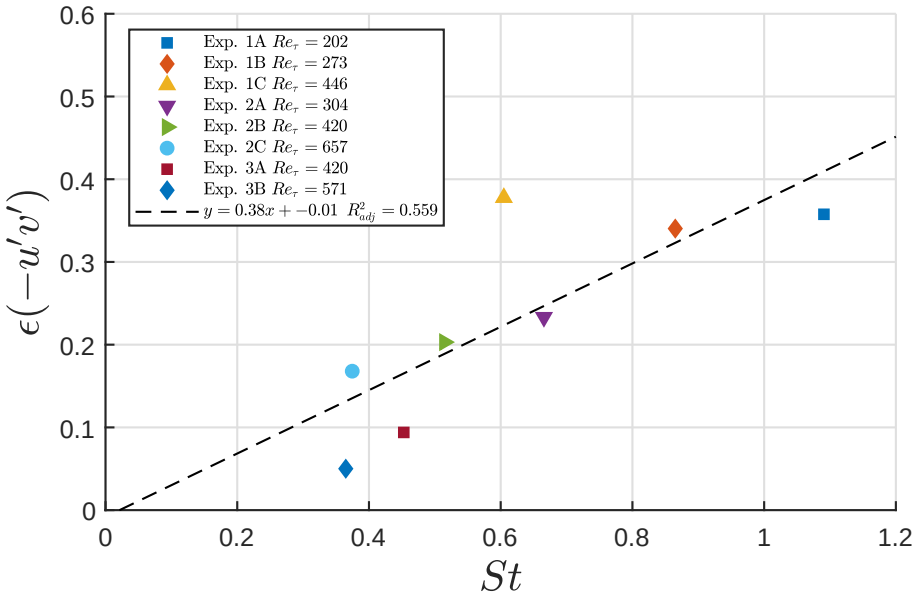

Figure 5.12: Relative error in Morkovin scaled Reynolds shear stress between the nine PIV cases and Klebanoff HWA data [18] at $y/\delta = 0.2$.

the mean measured stress begins to undershoot these data.

5.4 Spectral Density and Analysis of Large Scale Motion Structures

The wavenumbers for which the PSD is accurately resolved using PIV was found to be limited by two factors, particle response and interrogation window resolution. The limit based on the interrogation window resolution was determined based on a similar concept as the Nyquist frequency, where

$$k_{\text{cutoff,w}} = \frac{2\pi}{2D_I}. \tag{5.4}$$

For lower spatial resolutions this becomes the limiting wavenumber.

The particle response limit was determined using the method outlined by Mei [79].

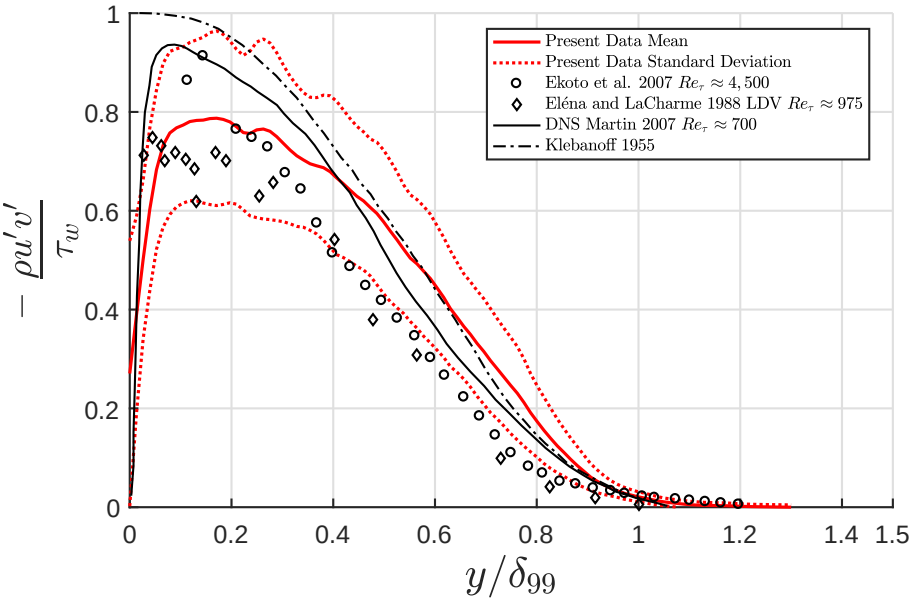

(a) Scaled by δ

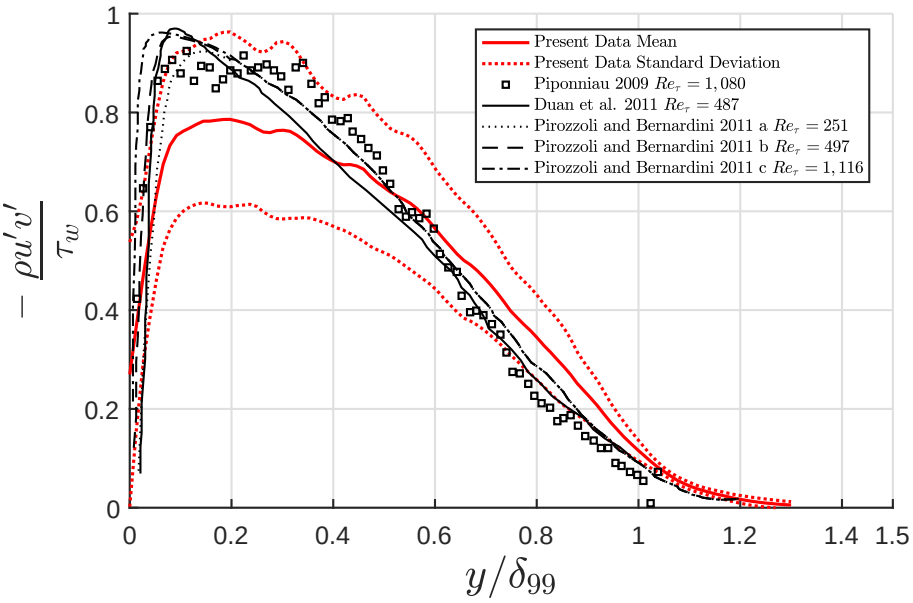

(b) Scaled by δ_{99}

Figure 5.13: Reynolds shear stress profiles compared with literature data.

The particle response function is assumed to be defined by

$$H_p(\omega) = \frac{1 + \epsilon - i\epsilon - i\frac{2}{3}\epsilon^2}{1 + \epsilon - i\epsilon - i\frac{4}{9}\left(\overline{\rho} + \frac{1}{2}\right)\epsilon^2} \tag{5.5}$$

where

$$\epsilon = \left(\frac{\omega d_p^2}{8\nu_f}\right)^{1/2} = \left(\frac{9}{4}\frac{\omega\tau_p}{\overline{\rho}}\right)^{1/2} \tag{5.6}$$

and

$$\overline{\rho} = \frac{\rho_p}{\rho_f}. \tag{5.7}$$

The Knudsen number corrected particle response time, τ_p, was used in Eq. 5.5 instead of the shorter Stokes flow particle response. The useful range of the particle response function for PIV is between

$$\frac{1}{2} < |H_p|^2 < 1. \tag{5.8}$$

The cutoff frequency, ω, was calculated by solving Eq. 5.5 for $|H_p|^2 = 0.5$. The cutoff wavenumber was determined from Taylors frozen turbulence hypothesis [80], assuming a convection velocity of 85% of the freestream

$$k_{\text{cutoff,p}} = \frac{\omega}{0.85u_e}. \tag{5.9}$$

The large ratio of densities, $\overline{\rho} \approx \mathcal{O}(10^4)$, was the driving factor for the particle response wavenumber cutoff. The limiting wavenumber is taken as the minimum of the interrogation resolution and particle response cutoff wavenumbers.

Figure 5.14 shows the streamwise and wall-normal PSD with Morkovin scaling at $y/\delta = 0.3$ for Sta. 1 and 2. Experiments at Sta. 3 have been omitted from this comparison due to the reduced usable FOV required to exclude disturbances from the wind tunnel diffuser. Wave numbers within the measurable limit are shown in color, while those above the limit are grayed out. The increased steepness of the slope in the grayed out sections of Figure 5.14 is indicative of the particle lag and spatial averaging. The streamwise power spectra density in the measurable data region adheres to a $k^{-5/3}$ decay. The wall-normal decay is closer to k^{-1}, indicating there is more energy at higher wavenumbers that has not been measured. This could explain why the wall-normal component has a greater sensitivity to particle lag as discussed by Lowe et al. [38].

Figure 5.15 shows correlation coefficient contour and the streamwise correlation coefficient for experiment 2A at $y/\delta = 0.2$. The data agree well with the KTV measurements from Mustafa et al. [26]. Exp. 2A is used for this comparison because it used the same orifice plate and measurement location as the KTV data. The PIV data also agrees well with DNS data from Duan et al. [29]. The extent of the correlation was similar in streamwise and wall-normal directions. In addition, the calculated angle of 9.6° agrees well with ∼9.5° angles presented by Peltier et al. [81] at Mach 5 for the smooth wall case.

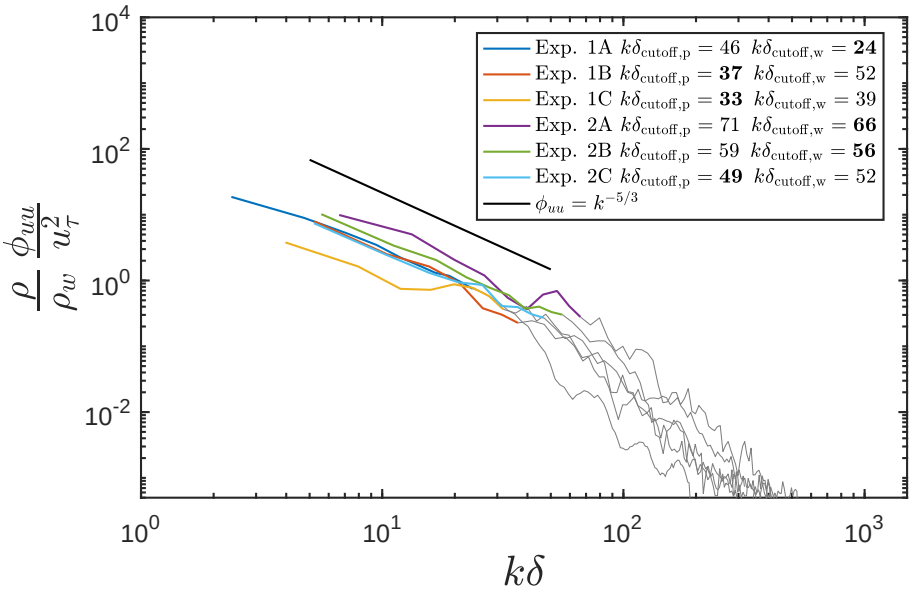

(a) Streamwise fluctuating velocity

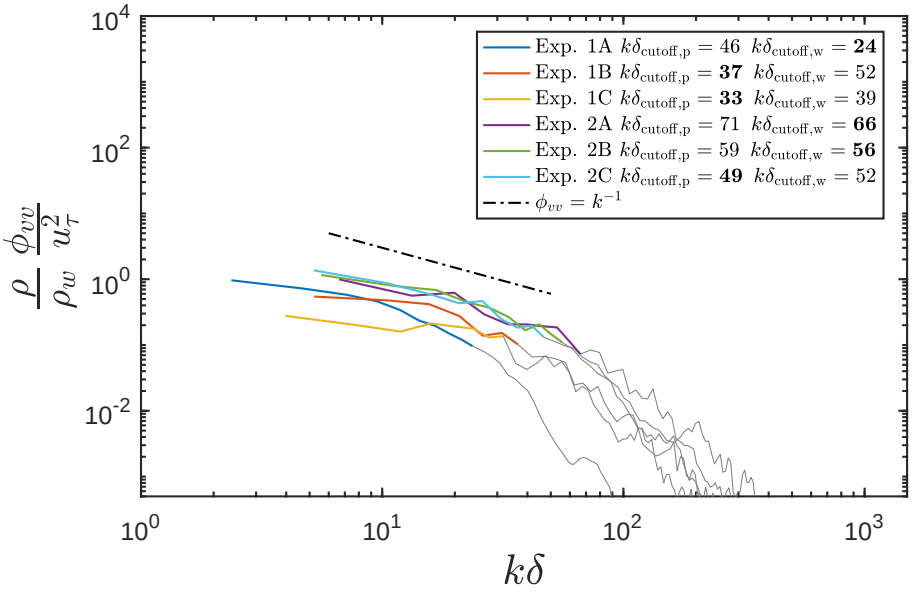

(b) Wall-normal fluctuating velocity

Figure 5.14: Power spectral density of the velocity fluctuations at $y/\delta = 0.3$ showing the energy content at a given wavenumber. The wavenumber is limited by the minimum cutoff value between the particle response and the interrogation window resolution, with values below the limit shown in color, and above grayed out. Measured energy content is larger for higher cutoff wavenumber experiments. Experiments at Sta. 3 omitted.

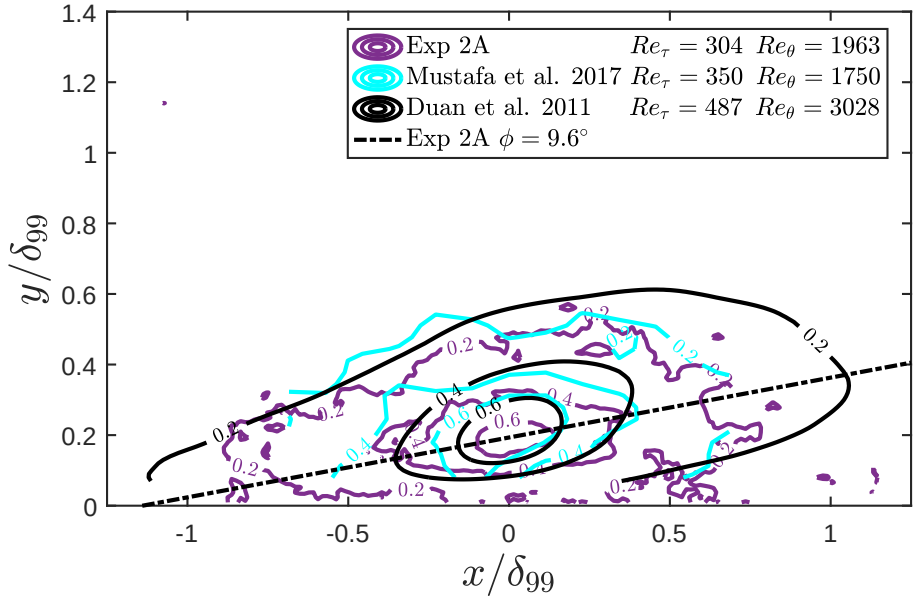

(a) Correlation Contour

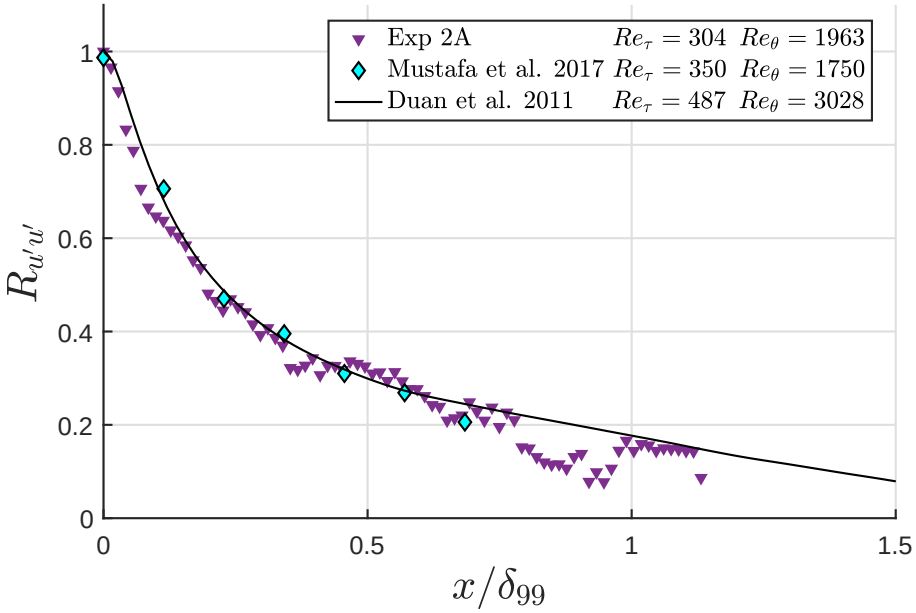

(b) Streamwise Correlation

Figure 5.15: Two-point spatial correlation R_{uu} vs. downstream streamwise distance at $y/\delta = 0.2$ showing excellent agreement of the PIV data to KTV data [26] measured on the same wind tunnel and DNS data from Duan et al. The dash-dot line shows the structure angle of 9.6° [29]

Chapter 6: Characterization of Local Injection

The flow conditions used for the local injection experiments are listed in Table 6.1. The data averaging and analysis is the same as described in Sections 3.1 and 3.3. Two measurement locations were used in the M3CT with local injection experiments duplicated with global seeding. The TBL measurement location is used for Tunnel 9. As described earlier it is unfeasible to have comparison global seeding data for Tunnel 9.

6.1 Concentration

Figure 6.1 shows a normalized comparison of experimental concentrations calculated with the Gaussian elimination and thresholding methods to those calculated by CFD. There is remarkable agreement in the particle concentration distribution between PIV and CFD. However, the PIV measured concentrations are higher than the CFD. At the peak PIV concentration, this increase is by a factor of 3.1, 2.7, and 1.7 for the M3CT Stations 2 and 3, and Tunnel 9, respectively. The cause of this discrepancy is not immediately clear. One possible reason is that the laser sheet scatters light from particles over a thicker region than what is measured by the burn pattern. This would decrease the PIV concentration because the volume

Table 6.1: Local injection PIV flow conditions

Tunnel	Exp No.	Station	Seeding	M_e	u_e (m/s)	Re_m (1/m)	δ (mm)	θ (mm)	u_τ (m/s)	Re_θ	Re_τ	St	$C_f \times 10^3$
M3CT	154	2	Global	2.8	604	8.5×10^6	8.2	0.56	29.8	4763	637	0.39	1.98
M3CT	179	2	Local	2.8	598	8.7×10^6	8.4	0.56	30.2	4923	661	0.38	2.03
M3CT	118	3	Global	2.7	594	9.0×10^6	11.3	0.78	28.4	6980	927	0.26	1.89
M3CT	019	3	Local	2.7	597	8.8×10^6	11.3	0.78	27.9	6867	914	0.26	1.83
Tunnel 9	184	—	Local	9.4	1465	18.5×10^6	25.8	0.61	61.8	11608	913	0.93	0.72

used for the concentration would increase. However, there exists enough of an order of magnitude estimation to allow for future injector design.

Both methods calculated the correct trend, according to CFD. The Gaussian elimination method calculated a higher particle concentration than the thresholding method for much of the boundary layer at all measurement locations. This is particularly true above the peak concentration location. The difference in concentration at $y/\delta = 0.8$ is 8.0%, 4.6%, and 5.8% for M3CT Sta. 2, Sta. 3, and Tunnel 9, respectively. Closer to the wall, the thresholding method tends to calculate a higher concentration than the Gaussian elimination. This may be attributed to increased noise in this region due to laser reflections.

The Gaussian elimination method was not anticipated to yield vastly different results from the thresholding method. At these image densities, the probability of overlapping particles in the image is low, particularly for local seeding. The Gaussian elimination method has greater merit at higher image densities.

6.2 Mean Velocity and Turbulence Statistics

6.2.1 Mean Velocity

Figure 7.6 shows the PIV velocity with van Driest transformed inner scaling for all test cases listed in Table 6.1. The data sets are grouped by Reynolds number and separated by an offset of 4 added to the ordinate for the higher Reynolds number group. The Tunnel 9 data is plotted with the M3CT Station 3 data due to the closely matched Re_τ. The u^+_{vd} scaling collapses the PIV data very well in the log

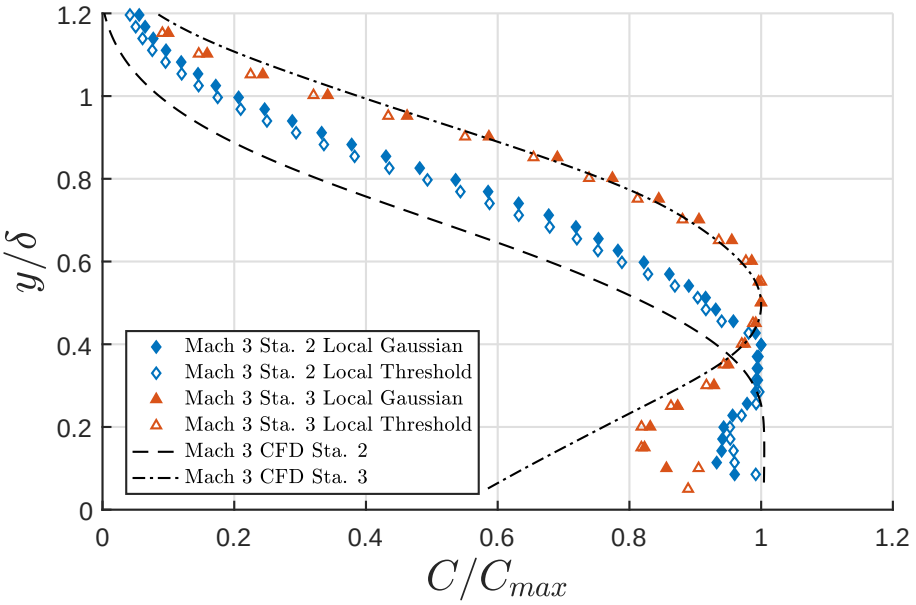

(a) M3CT

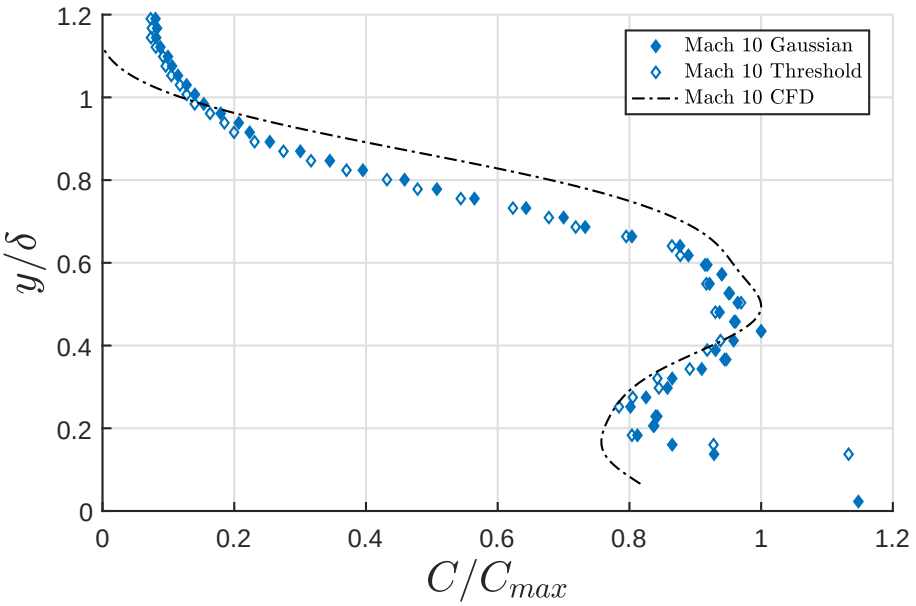

(b) Tunnel 9

Figure 6.1: Dimensional particle concentration calculated using the Gaussian elimination and thresholding methods compared to CFD solution.

layer. There is also good agreement in the wake region between local and global seeding for the M3CT Station 2 and 3 data sets. The wall normal extent of the wake region for Tunnel 9 matches the M3CT Station 3 which is expected from the similarity in the Reynolds number. However, the shape is slightly different. For comparison, the universal log law and Spalding boundary layer equations are plotted in Figure 7.6.

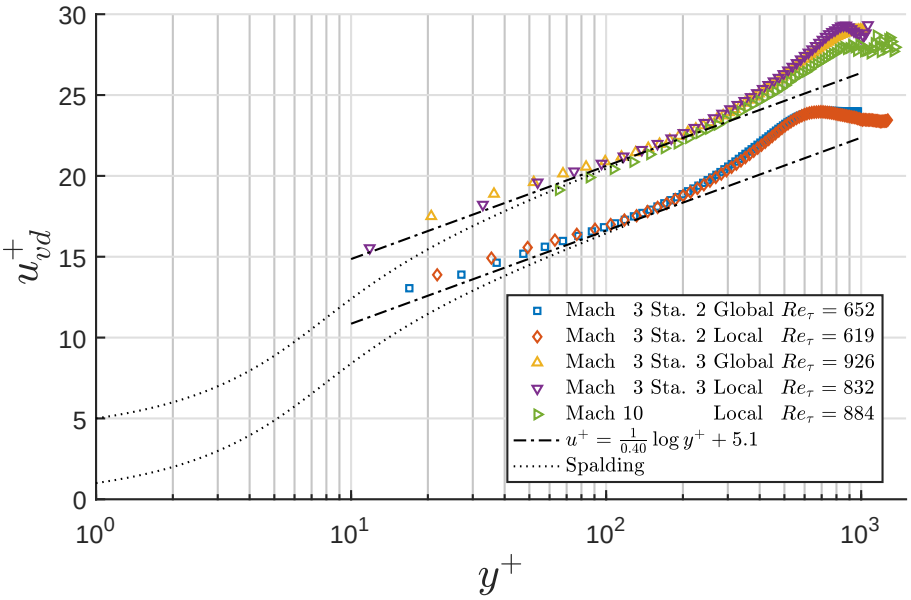

Figure 6.2: van Driest streamwise velocity with inner scaling. Good agreement exists between local and global seeding.

Figure 6.3 shows a detailed comparison between local and global seeding for the M3CT at Station 2. The profiles are normalized by the freestream velocity and the boundary layer thickness in Figure 6.3a and using inner scaling in Figure 6.3b. At $y/\delta = 0.12$ the local profile begins to decrease away from the global profile which is expected and is predicted by CFD. This is attributed to the injection of lower momentum fluid affecting the boundary layer. The maximum deviation is 0.6% at $y/\delta = 0.5$. The second feature is shown in detail in the subplots in Figure 6.3. At

the boundary layer edge, the local profile overshoots the global and then sharply decreases. The decrease is believed to be due to particle biasing, discussed in Section 6.4.

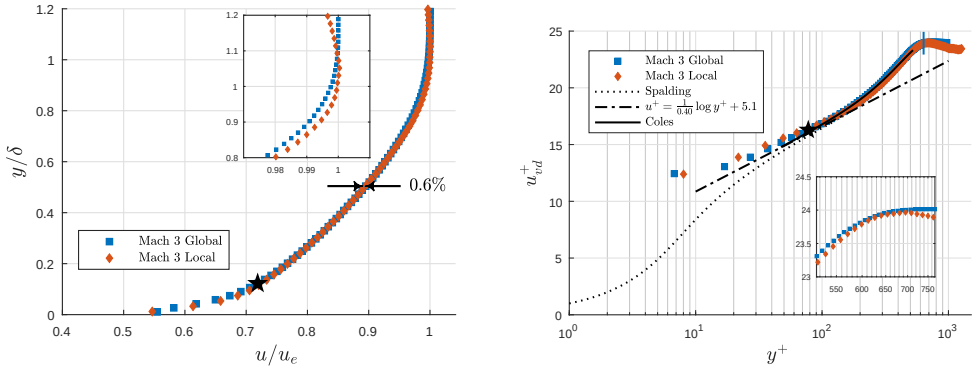

(a) Normalized streamwise velocity (b) Inner scaled streamwise velocity

Figure 6.3: Normalized streamwise velocity profiles. The stars in (a) and (b) represent the location where the local profile deviates from the global. The maximum deviation is 0.6% at $y/\delta = 0.5$. The subplots in (a) and (b) show the decrease in measured velocity using local injection at the boundary layer edge, $0.8 \leq y/\delta \leq 1.2$. The blue line in (b) shows the location of the boundary layer thickness.

Due to the behavior of the mean streamwise velocity at the boundary layer edge for local seeding data sets, the 99% or 99.9% boundary layer thickness is not accurately defined. Instead, the boundary layer thickness is determined from a fit of Coles's law of the wake [15] to the PIV data.

The reliability of this fit to calculate the skin friction velocity and the boundary layer thickness is determined by calculating these parameters for the M3CT Station 2 global data. The skin friction velocity, u_τ, calculated from the fit is within 5% of the van Driest II transformation which is recommended by Hopkins and Inouye [43] for the determination of supersonic and hypersonic skin friction. The boundary layer thickness determined by the fit, δ_c, is less than the 99.9% boundary layer thickness,

δ_{999}, and is closer to the 99% boundary layer thickness, δ_{99}.

6.2.2 Turbulence Statistics

Figure 6.4 presents the Morkovin scaled turbulence statistics (u', v', $-u'v'$) as a function of y/δ for the five cases listed in Table 6.1. Only the streamwise fluctuating velocity u' is presented for the Mach 10 case because the data quality is greatly reduced for the wall normal component. These turbulent statistics profiles are compared against experimental data and DNS from the literature listed in Table 6.2. A few outer length scales (boundary layer thickness) are used in literature to normalize the wall normal distance. It is important to use the same scaling when comparing profiles to visualize trends in the data because these scales can differ by approximately 15%. Experimental data from Lapsa et al. [21], at the $x/\delta_0 = 40.0$ measurement location used a boundary layer calculated from the same fit of the Coles law of the wake as previously presented for Tunnel 9 data. Piponniau [20], Pirozzoli et al. [12], and Duan et al. [29] used δ_{99}. These literature data are included in Figure 6.4 because the boundary layer from from the fit of Coles' law of the wake was most similar to δ_{99} for the M3CT global data sets.

The PIV data have very good agreement with the literature data for the streamwise fluctuating velocity. In particular, the M3CT local data has excellent agreement with the corresponding global data for $y/\delta < 0.8$. However, all local data sets exhibit the same rapid increase in fluctuating velocity magnitudes high in the boundary layer. These deviations occur at $y = 0.9$, 0.8, and 0.6 for the M3CT Station 2, Station 3,

Table 6.2: Key parameters from comparison literature data

			M_e	Re_τ	Re_θ	H	C_f
Piponniau 2009 [20]		PIV	2.28	1,080	5,100	3.54	2.00×10^{-3}
Lapsa et al. 2011 [21]		PIV	2.75	717	6,600	1.4	1.90×10^{-3}
Pirozzoli et al. 2011 [12]	a	DNS	2.00	251	1,122	3.08	3.19×10^{-3}
	b			497	2,377	2.98	2.67×10^{-3}
	c			1,116	6,046	2.91	2.11×10^{-3}
Duan et al. 2011[29]		DNS	2.97	487	3,028	5.09	2.17×10^{-3}

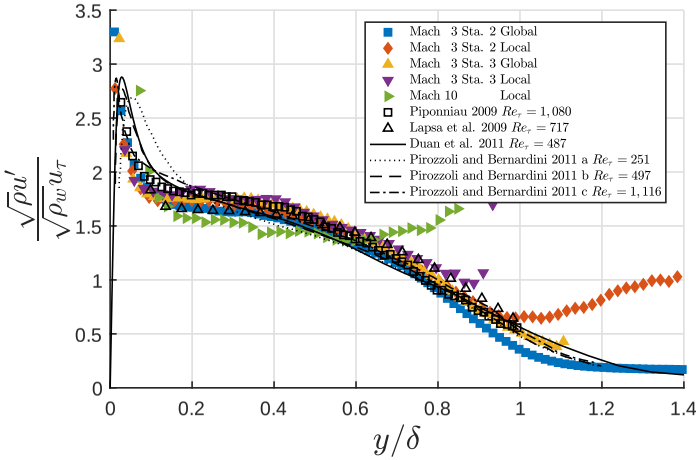

(a) Streamwise fluctuating velocity u'

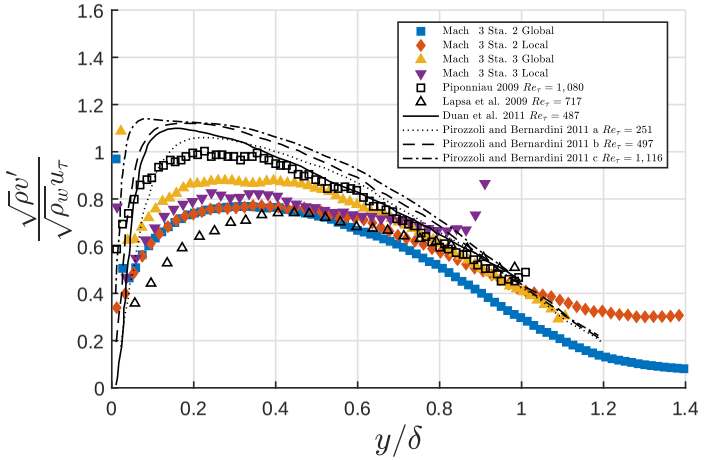

(b) Wall normal fluctuating velocity v'

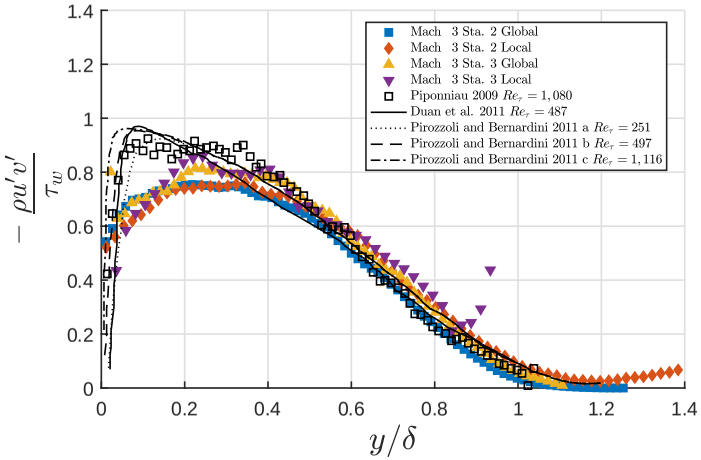

(c) Reynolds shear stress $-u'v'$

Figure 6.4: Morkovin scaled turbulence statistics comparing local seeding to global seeding and data from the literature. All the local data show a stark deviation from the global data at $y = 0.9$, 0.8, and 0.6 for the M3CT Station 2, Station 3, and Tunnel 9 respectively.

and Tunnel 9 respectively. This phenomenon seems to be an artificial effect of the local seeding and is investigated further in Section 6.4.

Figure 6.4b presents the Morkovin scaled wall-normal fluctuating velocity profiles as a function of y/δ for the M3CT. There is excellent agreement between local and global seeding at Station 2 for $y/\delta < 0.5$. Above this the local data shows a gradual increase in magnitude compared to the global data as opposed to the sharper increase shown in the streamwise component. There is good agreement between local and global data at Station 3. The local data had slightly lower magnitudes throughout the profile. The wall-normal component at Station 3 again shows the sharp increase around $y/\delta = 0.8$ which was seen in the streamwise component. The wall-normal fluctuating velocity magnitudes for the present data is lower than most of the literature data, excluding those from Lapsa et al. [21]. This was shown in a Section 5.3.2 to be due to effects of the particle response.

The Morkovin scaled Reynolds shear stress is for the M3CT as a function of y/δ is shown in Figure 6.4c. Again, there is good agreement shown between local and global seeding at the two stations. Local seeding data at Station 3 shows the sharp increase around $y/\delta = 0.8$ as shown in the streamwise and wall-normal components. The Reynolds stress magnitude for the local seeding data at Station 2 has good agreement with global data until about $y/\delta = 1.2$, then begins to increase. PIV data from the M3CT has good agreement with experimental and DNS data from the literature for $y/\delta > 0.4$. As the wall is approached, the PIV measured stress begins to undershoot these data.

6.3 Impact of Local Injection

The local injection has little impact on the measured velocity for the majority of the Mach 3 boundary layers. The boundary layer thickness increased by 2.4% and 0.2% for Stations 2 and 3, respectively. The RANS CFD solutions also show this increase when comparing the baseline boundary layer to the boundary layer with particle injection. The injection caused the CFD boundary layer to thicken by 2.9% on average between Stations 2 and 3. The coefficient of friction increased by 2.6% for Station 2 decreased by 3.3% for Station 3. These flow parameters show that there is negligible impact on both inner and outer scales of the boundary layer. The deviation of the local injection values from the global seeding are within the measurement uncertainty.

Figure 6.5 shows the relative error between local injection and global seeding in the mean velocity and fluctuating statistics for the M3CT. The relative error is of the same order as the measurement uncertainties for the majority of the boundary layer. The relative error for these quantities at Station 2 are within the combined measurement uncertainty for $0.05 < y/\delta < 0.7$. At Station 3, this is extended to $0.05 < y/\delta < 0.8$. The further extent of agreement may be attributed to a wider dispersion of particles due to increased distance from the injection point. The increased relative error near the wall is likely due to increased measurement error in this region.

A clear difference between global and local seeding is the distribution of particles throughout the boundary layer. Figure 6.6 compares the normalized local and

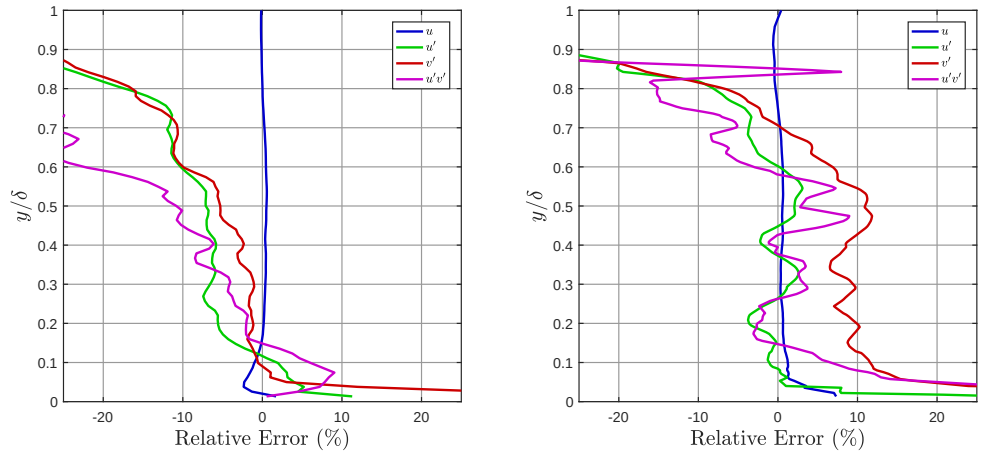

(a) Station 2 (b) Station 3

Figure 6.5: Relative error between local injection and global seeding for the M3CT. The relative error is within the measurement uncertainty for $y/\delta < 0.7$ and 0.8 for Stations 2 and 3, respectively, except for $y/\delta < 0.05$.

global seeding particle concentration profiles for the M3CT at Station 2. The global seeding particle distribution is nearly symmetrical to the local seeding about the mid-concentration point. Local seeding is able to deliver a much higher particle concentration near the wall, given equal maximum particle concentrations. However, the current injector design is only able to achieve about 1/4 of the maximum concentration from the global seeding. Further investigation into injector nozzle design and particle generation methods are necessary to increase the maximum concentration.

The normalized mean flow density is also included in Figure 6.6. This plot shows that the global seeding particle concentration distribution roughly scales with the mean flow density. For Mach 3 this means that the particle concentration near the wall is roughly a third of the maximum concentration in the freestream. However, if global seeding were to be used in Tunnel 9 the particle concentration near the wall

would only be a fifth.

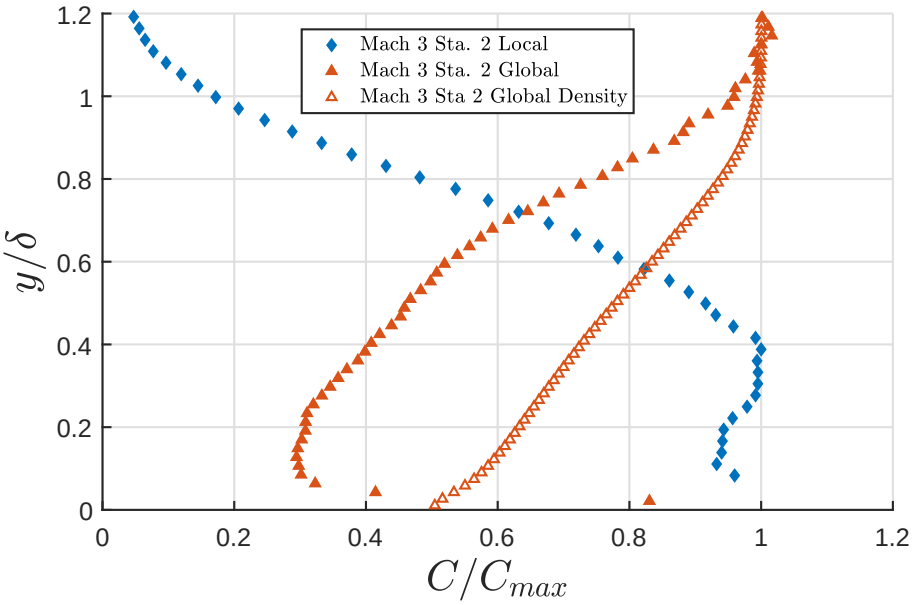

Figure 6.6: Normalized local and global seeding particle concentration profiles for the M3CT at Station 2. The has a more uniform profile in the boundary layer. The normalized density profile shows that the global seeding particle concentration has the same trend as the local flow density.

6.4 Particle Biasing

Particle biasing is the phenomenon that the distribution of particles affects the PIV measurement. Generalizing the local seeding particle distribution in a turbulent boundary layer, there is a high concentration of particles in the lower half with the concentration decreasing to zero as the freestream is approached, shown previously in Figure 6.1. The turbulent statistics shown in Figure 6.4 are due to turbulent mixing. Low momentum fluid is ejected higher in the boundary layer and likewise high momentum fluid is swept lower in the boundary layer. For local seeding, there is a high concentration of low momentum particles in the boundary layer to be ejected up. But there are much fewer to no particles in the freestream to be swept

back into the boundary layer to be measured. Figure 6.7 shows the number of valid vectors calculated by DaVis after post processing filters for the three local seeding cases. The reduced number of valid vectors calculated near the freestream may be attributed to the absence of particles from the freestream. The location of the drop-off in valid vectors correlates to the location of the increased magnitudes in turbulent statistics in Figure 6.4.

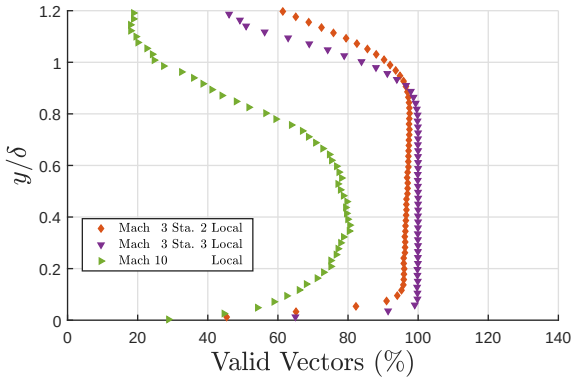

Figure 6.7: Percent of valid vectors calculated by DaVis after post processing filters. The location of the valid vector drop-off correlates to the increase of turbulent statistic magnitudes in Figure 6.4.

It is assumed that the majority of the missing velocity vectors are high momentum fluid from the freestream. This is supported by the probability density function (PDF) of velocity vectors. Figure 6.8 presents the PDF of the M3CT Station 2 local and global seeding data to compare the distribution of velocity vectors at $y/\delta = 0.2$, 0.7, and 1.2. The PDF is scaled by the percentage of valid vectors and the velocity is scaled by the mean and standard deviation of the global data. The data is fit to a stable distribution in order to show the skewness while minimizing binning effects of histograms. Figure 6.8c shows that in the freestream, the global data has a normal distribution. However, the local data exhibits negative skew and the mean velocity

(represented by the vertical lines in Figure 6.8) is shifted to the left. The global data has nearly 100% valid vectors whereas the local data only has approximately 60%. It is assumed that the remaining 40% of the vectors would fill in the PDF to the right, reducing the skewness and shifting the mean velocity back towards that of the global data.

However, existence of skewness in the PDF does not indicate particle biasing within the boundary layer where an amount of negative skewness is expected. This is due to the intermittency of the boundary layer, as demonstrated by Klebanoff [18]. From $0.4 \leq y/\delta \leq 1.2$ the turbulent boundary layer is no longer fully turbulent, but has and on/off behavior of turbulence and non-turbulence at a given wall location. The average thickness of the boundary layer was calculated in Section 6.2.1, but at any given point the boundary layer edge may fluctuate between $y/\delta = 0.4$ and 1.2.

Townsend [17] proposed this is due to large scale motion (LSM) coherent turbulent structures (or "main eddies") convecting with the flow creating bulges in the boundary layer. Figure 6.9 shows a sample of a single PIV velocity frame from the Tunnel 9 data set. The colors represent streamwise velocity and the quiver plot shows the velocity fluctuations. The intermittency is visible in this local seeding frame. Coherent turbulent structures eject low momentum fluid above the boundary layer thickness and the unseeded freestream is swept down to $y/\delta = 0.6$ around $x/\delta = -1$.

The intermittency may be seen in the shape of the PDF presented in Figure 6.8. At $y/\delta = 0.2$, the turbulence is fully isotropic and the PDF has a normal distribution. However, at $y/\delta = 0.7$ the intermittency causes a negative skew in the PDF. At the

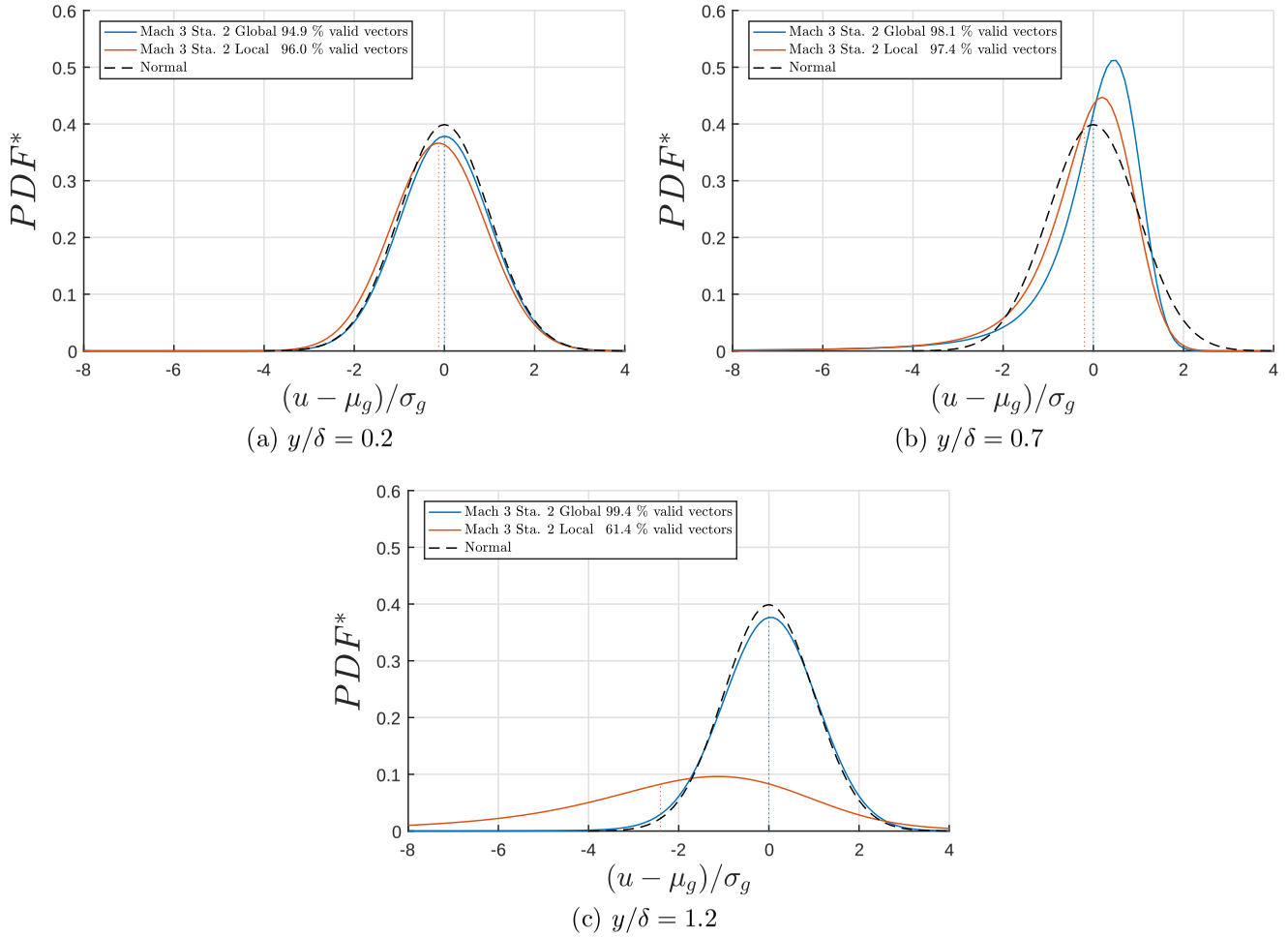

(a) $y/\delta = 0.2$ (b) $y/\delta = 0.7$

(c) $y/\delta = 1.2$

Figure 6.8: Stable distribution of streamwise velocity for the M3CT Station 2 global and local seeding. The normal distribution shown for reference and mean velocity is indicated by the vertical colored lines. (a) Normal distribution in the isotropic turbulence region. (b) Expected negative skew in intermittent region. (c) Negative skew and increased standard deviation in the local data indicating particle biasing.

edge of the intermittency region, $y/\delta = 1.2$, the global data returns to a normal distribution due to the low turbulence level in the freestream. The local seeding data retains a high level of negative skew which is attributed to particle biasing.

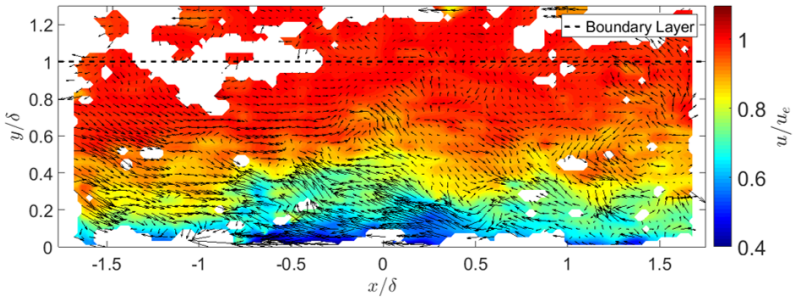

Figure 6.9: Instantaneous sample PIV frame from the Tunnel 9 data set. Streamwise velocity is shown by the contour colors and the quiver plot shows the velocity fluctuations from the mean. The intermittency of the boundary layer is visible.

The degree of intermittency is expressed through the intermittency factor

$$\gamma = 3.0 \Big/ \frac{\overline{u'^4}}{\overline{u'^2}^2} \,. \tag{6.1}$$

The intermittency factor is the ratio of the flatness in the isotropic turbulent region to that in the intermittency region. Since the isotropic turbulence region is nearly Gaussian, the flatness $F_u \approx 3$. Figure 6.10 presents the intermittency factor as a function of y/δ. Klebanoff showed that the decay of γ with y/δ resembles that of a Gaussian integral curve defined as

$$\gamma = \frac{1}{2}(1 - \mathrm{erf}\zeta), \tag{6.2}$$

where

$$\zeta = 5\left(\frac{y}{\delta} - 0.78\right). \tag{6.3}$$

All the PIV data show good agreement with the Gaussian integral curve. The global data from the M3CT show an increase in γ near the boundary layer edge representing the return to a normal distribution in the freestream. The local data from M3CT Station 2 and Tunnel 9 maintain a low γ into the freestream. The intermittency factor shows little indication of the particle biasing effects seen in the turbulence statistics shown in Figure 6.4, particularly the deviation in the Tunnel 9 data around $y/\delta = 0.6$.

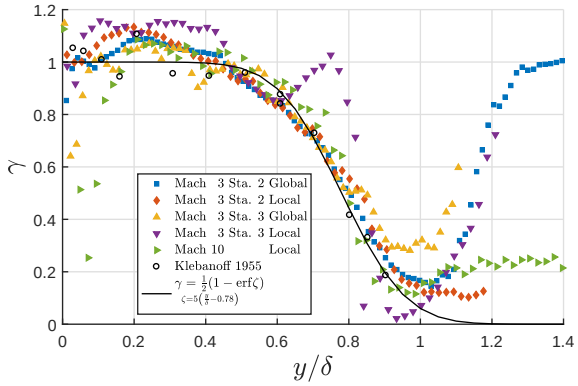

Figure 6.10: Comparison of the intermittency factor plots of local seeding to global. All data sets exhibit the Gaussian integral curve decay with wall normal distance. The global data intermittency returns to near zero above $y/\delta = 1.2$.

The plot of the skewness shown in Figure 6.11 reveals more about the particle biasing due to local seeding. The incompressible data from Antonia and Luxton [82] are shown for reference to the expected behavior of skewness throughout a turbulent boundary layer. The M3CT global data both show increasing negative skewness until the boundary layer edge where the skewness returns to near zero. However, the M3CT and Tunnel 9 local data all show erratic behavior of the skewness around the respective deviation points in Figure 6.4. The skewness seems to give an indication of the extent of reliable turbulent statistical data available from local seeding.

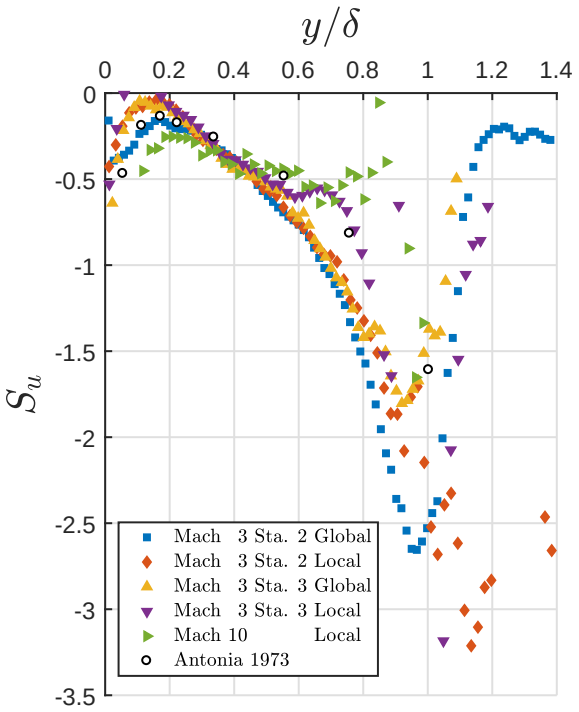

Figure 6.11: Comparison of the skewness plots of local seeding to global. The behavior of the skewness become erratic for the local seeing data at the point the turbulence statistics begin to deviate in Figure 6.4. Incompressible data from Antonia and Luxton [82] shown as a reference for the expected behavior.

Chapter 7: Mach 10 PIV

7.1 Injector Modifications

During the checkout runs for the HCF it became apparent that the tunnel was running off-condition. The Mach number measured by using a Pitot probe measured lower than targeted. One of the proposed reasons for this reduced Mach number was the protruding seeding injector housing in the HCF leading edge. The stronger shock from the 20° injector housing may have caused the boundary layer on the opposite side of the inner channel of the HCF to separate. This would cause the center flow to unstart and essentially block all flow through the center of the HCF. Due the large outer diameter of the HCF, the test article is required to be hollow in order to allow enough mass flow rate to sustain the Mach 10 flow. Other causes were proposed in addition to the seeding housing. However, Tunnel 9 was only reserved for the HCF for a short period of time. I decided to modify the seeding hardware to fit into the 7° leading edge angle. Even though this was not the ultimate cause, at the time, modifying the hardware would provide the highest probability of successfully performing PIV on the desired flowfield in the time allotted.

Figure 7.1 shows a comparison between the original design and the modified design to fit into the 7° leading edge. There are several features which are required for the

operation of the injector. I designed modifications to these components to retain the mating surfaces while packaging inside the 7° angle. Modified components are shown in the same color as in the original design. The leading edge is aligned and the images are shown with the same scale.

(a) Original Design

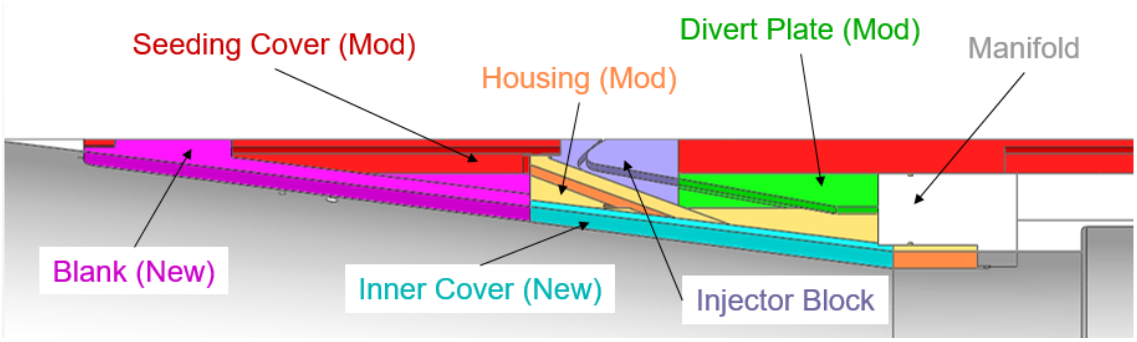

(b) 7° Modifications

Figure 7.1: Comparison of modified HCF seeding injector to the original design. Components were modified to package inside the 7° leading edge angle to avoid a stronger shock from the original 20° housing design. Mating features on the original hardward were retained.

The injector location was pushed back 115 mm downstream of the original placement. At this location the thickness of the leading edge could accommodate the height of the injector block. This required the cover plate to be modified to interface with the new injector location. However, the radius on the shoulder of the injector block did not match the inner radius at the new cover plate location, as seen in Figure 7.2. I programmed a CNC mill to machine the injector block shoulder down to have a flat interface. A matching feature was then CNC milled into

the cover plate. The next major modification was to the injector housing. The 20° angle at the front of the housing also formed the lower profile for the injector nozzle. This face must be retained since it mated to the axisymmetric nozzle. The middle of the housing was machined away and the front angle was bonded to the rear of the housing as shown in Figure 7.2. This modified design retained as much of the original mounting features as possible. A new cover plate was manufactured from sheet metal and bent to match the 7° axisymmetric leading edge inner surface. A new blanking plug was printed from high temperature resin to fill the original hole in the cover plate for the injector block and form the inner surface of the leading edge. Aluminum tape is used on the inner and outer surfaces of the leading edge to minimize gaps or steps exposed to the hypersonic flow. Figure 7.3 shows the comparison of the HCF leading edge before and after the injector housing modifications.

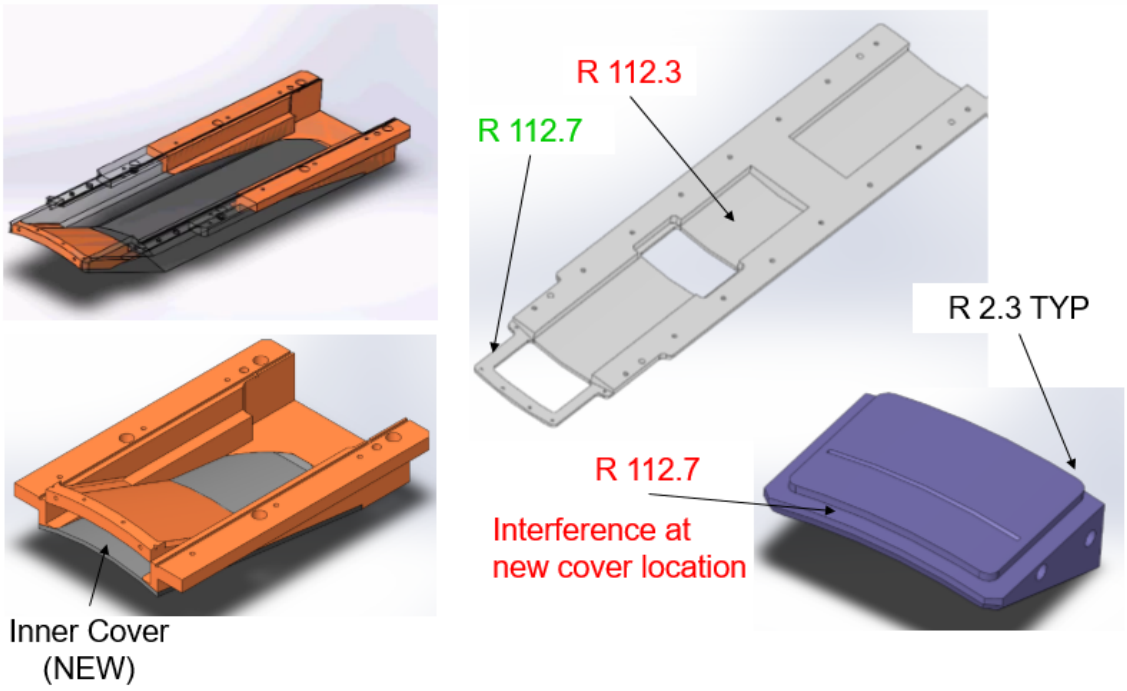

Figure 7.2: Modifications to mating components necessary to package the local injector in the 7° leading edge.

7.2 HCF Movement

The position of the HCF in the images varied as though the test article was oscillating up and down during the run. The position of the wall must be constant in all images for ensemble averaging. The wall is identified in the images as a line of nearly saturated pixel intensities. I small search region is identified as 30 pixels around the brightest row of pixels in the image. The wall is then identified as the brightest pixel in each column of this search region. In the event of multiple bright pixels in a column, the column is skipped. The angle of the line is calculated from a linear regression of these bright pixels. The edges of the images are unused in this fit due to increased uncertainty in this region from lower laser intensity.

The images were then rotated about the wall location at the streamwise center of the image. The new pixel intensities were calculated using bicubic interpolation. The images were cropped from the top so that they were all the same dimensions. I programmed the Matlab graphical user interface (GUI) which is shown in Figure 7.4 in order to aide in this image correction. By using the GUI I was able to verify that every image was rotated correctly. A similar approach was used for the ramp in the STBLI images. However, now two lines were identified and the images were rotated about the intersection point (ramp corner).

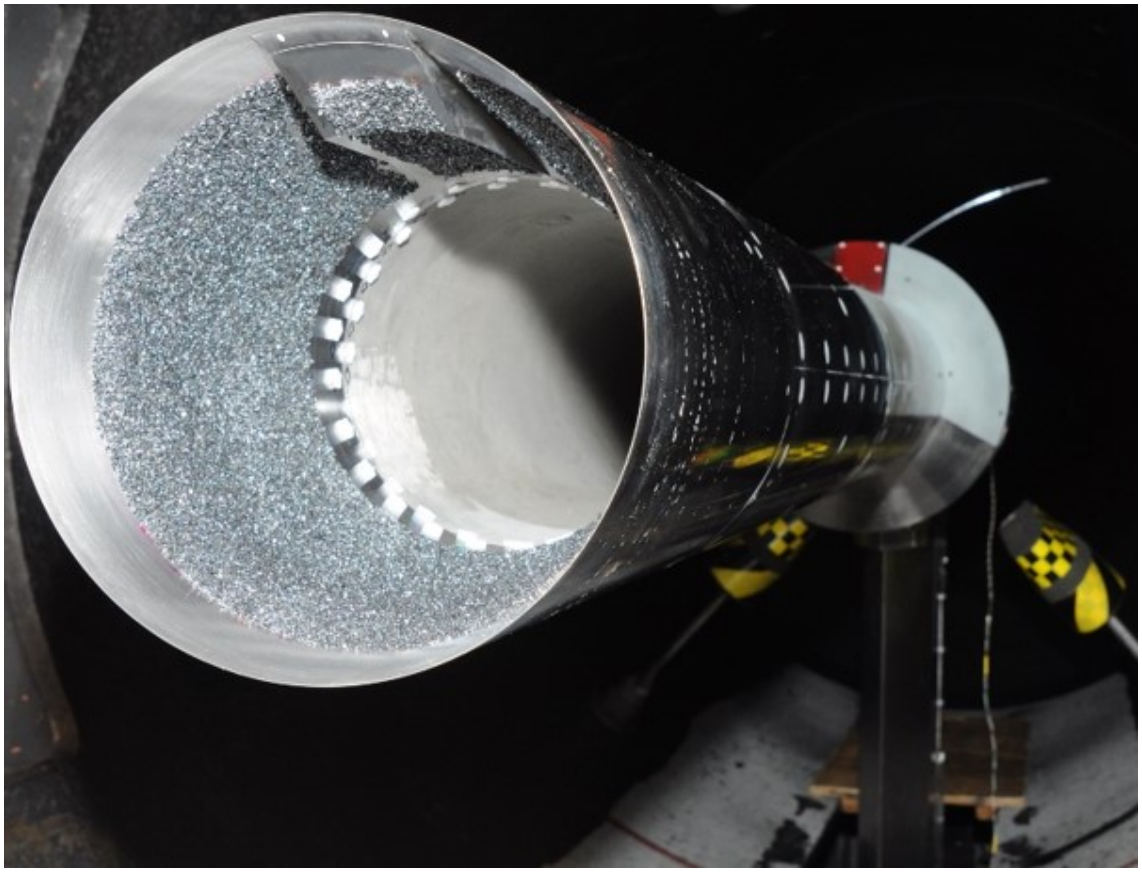

(a) Original Design

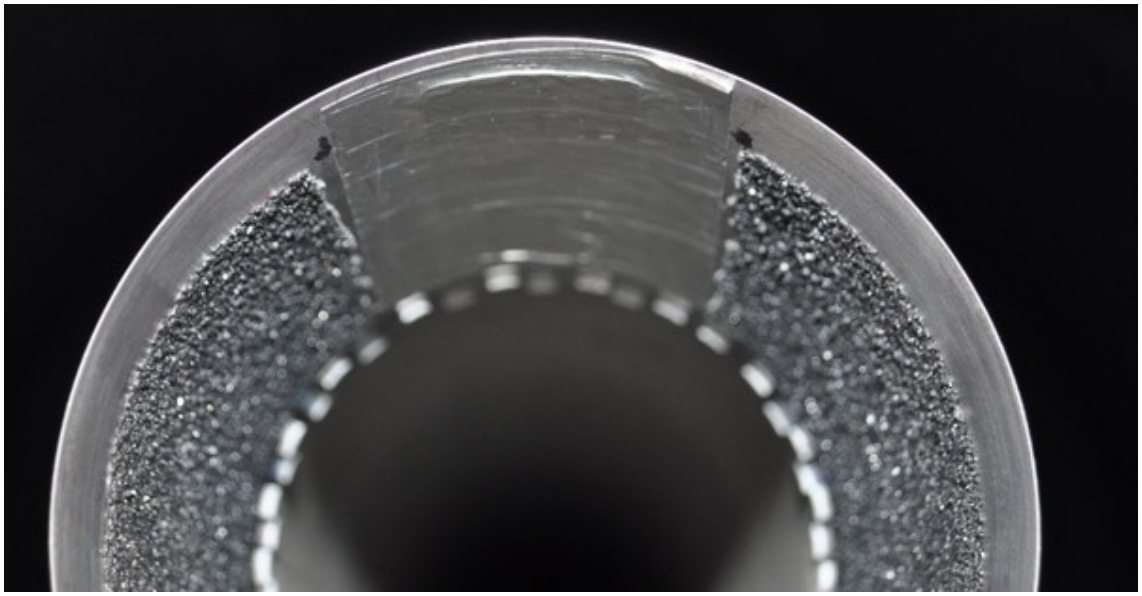

(b) 7° Modifications

Figure 7.3: Pictures of the HCF leading edge before and after the injector housing modifications.

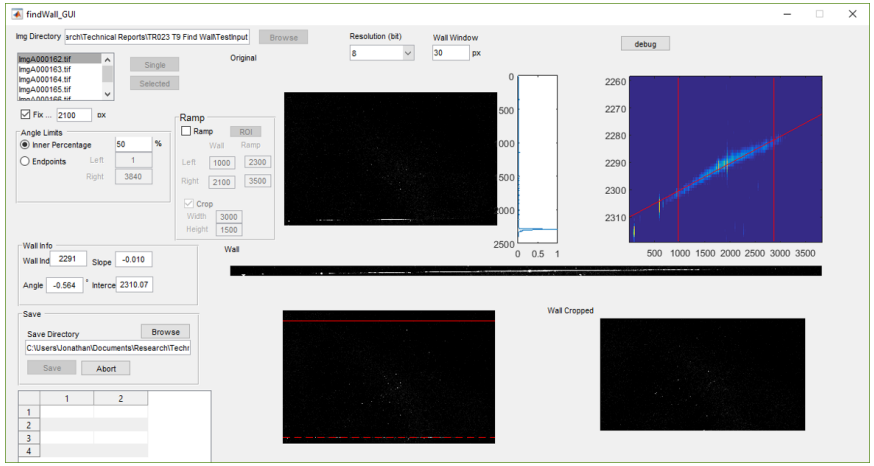

(a) TBL

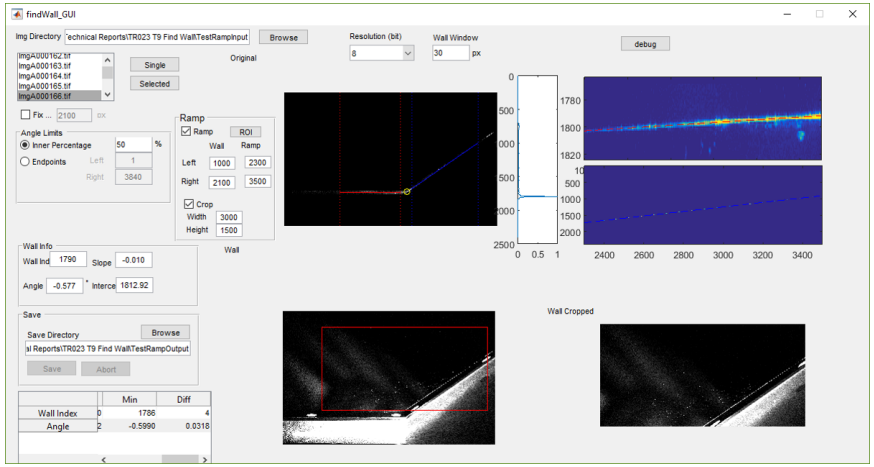

(b) TBL

Figure 7.4: Matlab GUIs programmed in order to aide in the identification and correction of HCF test article movement in the PIV images.

7.3 Particle Concentration

Adequate particle concentration in the boundary layer is critical to the successful application of PIV in Tunnel 9. Furthermore, the particle distribution calculated from the CFD particle tracking codes must be validated in order to continue the development of local injector profiles. Figure 7.5 shows the normalized Mach 10 TBL particle concentration profile compared against the CFD results. The PIV particle concentration is calculated based on a thresholding method. The threshold was determined as three standard deviations over the mean pixel intensity for the measurement region of interest (ROI).

As expected with local injection, there is a high concentration of particles in the lower half of the boundary layer which diminish towards the boundary layer edge. The particle distribution profile in the boundary layer has great agreement with the CFD solution used to develop the injector nozzle geometry. The peak PIV image density is 80 for the first pass interrogation window size and 5 for the final window size.

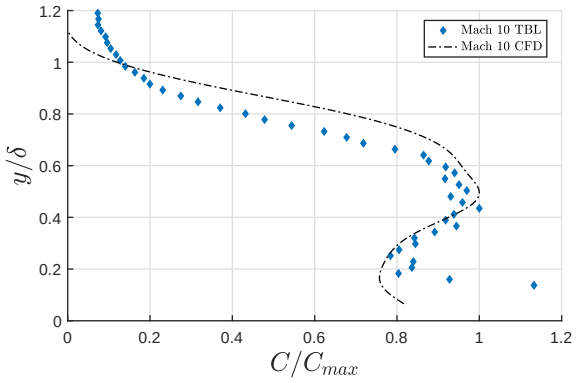

Figure 7.5: Dimensional particle concentration calculated using the Gaussian elimination method compared to CFD solution.

Particle distributions for the STBLI measurement location where analyzed qualitatively. Upstream of the compression corner the particle distribution is very similar to that displayed by the TBL. However, after the compression corner, the particles are squeezed closer to the wall with a lower concentration. This is attributed to the streamlines compressing after the shock and particles impacting the wall of the ramp due to inertia.

7.4 Turbulent Boundary Layer

Mean velocities were ensemble averaged for the 360 image pairs (two tunnel runs) and over a streamwise distance of 0.5δ for a total of about 7,500 realizations at each y/δ location.

Figure 7.6 shows the PIV measured TBL velocity profile with van Driest transformed inner scaling. Tunnel 9 TBL data has excellent agreement to the reference adiabatic incompressible zero pressure gradient (ZPG) log law ($\kappa = 0.41$ and $C = 5.1$) equation. This indicates that the van Driest transformation accurately collapses cold wall turbulent boundary layers when the skin friction velocity is determined as described previously. This same conclusion was found by Duan et al. [83]. The Tunnel 9 data also agrees well with Mach 3 data with a similar Re_τ measured in a previous study [84]. There is excellent agreement in the wake region.

The PIV data exhibits an apparent decrease in velocity near the boundary layer edge. In Section 6.4, I showed that this decrease is an artificial effect of the local seeding injection referred to as particle biasing. The distribution of particles seen in

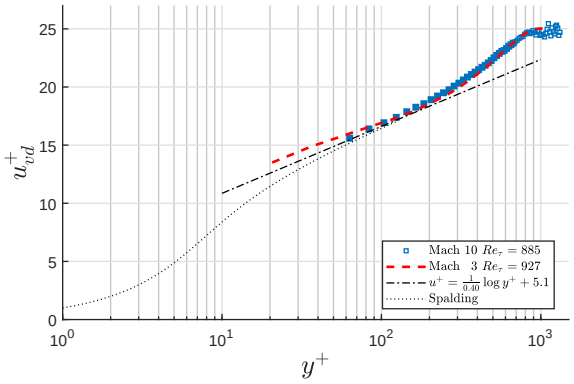

Figure 7.6: van Driest streamwise velocity with inner scaling. The cold wall hypersonic data has good agreement to incompressible adiabatic TBL theory [14] and Mach 3 adiabatic TBL data from a previous study [84].

Figure 7.5 produces a disproportionately high concentration of low momentum near-wall particles. Without an equal number of high momentum freestream particles, the velocity statistics have increased negative skew. Data points used for the fit of Eq. 2.9 (show as filled symbols from $50 \leq y^+ \leq 700$) are well below the particle biasing effects.

7.4.1 Mean Streamwise Fluctuating Velocity

Figure 7.7 presents the Morkovin scaled streamwise fluctuating velocity profiles as a function of y/δ compared to data from the literature. These literature data sets are Mach 3 adiabatic PIV measurements from Lapsa et al. [21], Mach 2 adiabatic DNS from Pirozzoli and Bernardini [12], Mach 5 cold wall ($T_w/T_r = 0.35$) DNS from Duan et al. [83] and Mach 7 adiabatic DNS from Duan et al. [29]. There is good agreement between the current data and data from the literature for y/δ<0.6. The density weighted scaling successfully collapses the hypersonic profile with supersonic data. Particle biasing artificially increases the fluctuating velocity magnitudes for

y/δ>0.6.

Table 7.1: Key parameters from comparison literature data

		M_e	Re_τ	Re_θ	T_w/T_r
Lapsa et al. 2011 [21]	PIV	2.75	717	6,600	1
Pirozzoli and Bernardini 2011 [12]	DNS	2.0	1,116	6,046	1
Duan et al. 2010 [83]	DNS	4.97	625	2,300	0.35
Duan et al. 2011 [29]	DNS	6.89	392	1,586	1

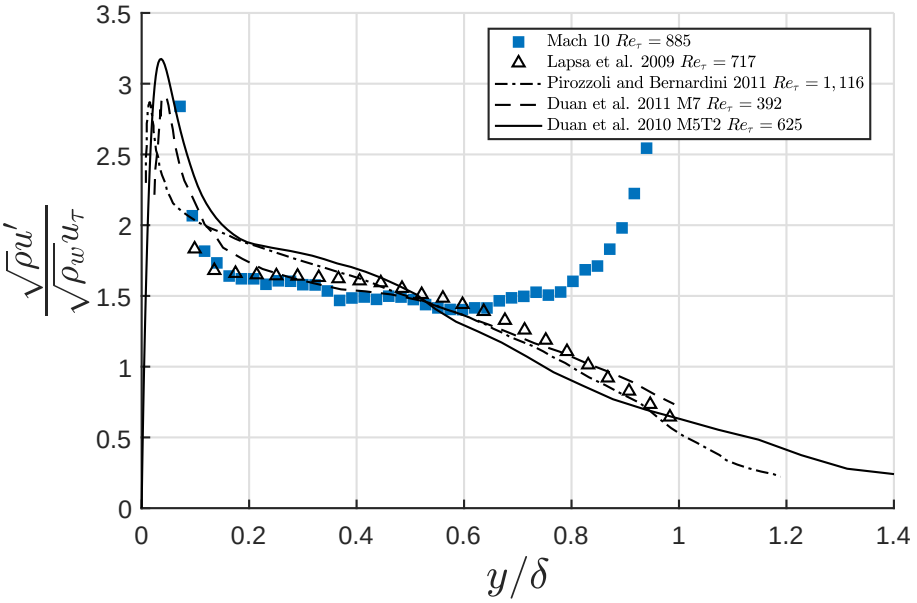

Figure 7.7: Streamwise Morkovin scaled fluctuating velocity profiles compared to experimental and DNS literature data.

7.4.2 Large Scale Motion Structure Angle

Figure 7.8 shows a contour plot of the spatial correlation coefficient at $y/\delta = 0.2$. A coarser velocity vector set (128×128 px^2 windows with 50% overlap) is used for in Figure 7.8 for a better visualization of the structure. The finer solution suffers from the lack of streamwise averaging and does not exhibit as smooth correlation isocontours. The structure angle describes the upstream lean of the coherent hairpin

turbulence packets as described by Perry and Chong [45]. The angle is calculated from the rotation of ellipses that are fitted to isocontour levels of the correlation coefficient. The rotation angle shown is the average for isocontour levels of $R_{uu} = [0.4,\ 0.5]$. The calculated angle of 9.6° agrees well with ∼9.5° angles presented by Peltier et al. [81] at Mach 5 for the smooth wall case.

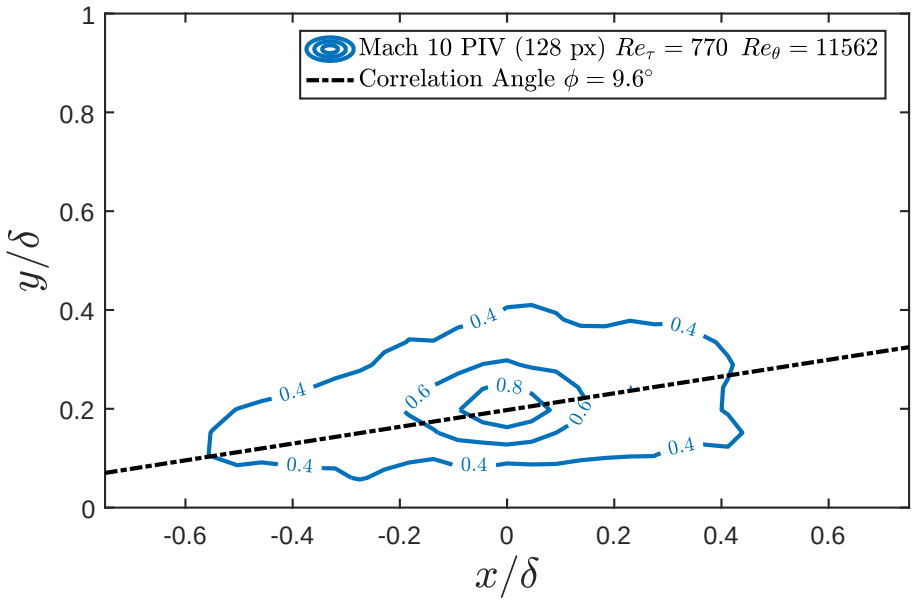

Figure 7.8: Two-point spatial correlation R_{uu} vs. streamwise distance at $y/\delta = 0.2$. The dash-dot line shows the structure angle of 9.6° [29]

7.5 Shock Turbulent Boundary Layer Interaction

Mean velocities for the STBLI flowfield were ensemble averaged for 540 image pairs over three tunnel runs with no streamwise averaging. Figure 7.9 shows the mean velocity magnitude normalized by flow parameters at the TBL (δ_0 and u_{e0}). A similar boundary layer to the TBL measurement location is visible upstream of the interaction. The streamlines are compressed downstream of the compression corner yielding a much thinner boundary layer along the ramp compared with the incoming

boundary layer. There is a separated region at the compression corner with a length on the order of δ_0. This is somewhat smaller than the separated region predicted by Helm and Martin [85]. The decrease in separated length may be due to 3-D effects of the axisymmetric geometry. The dashed lines in Figure 7.9 show examples of wall normal profiles used in subsequent figures.

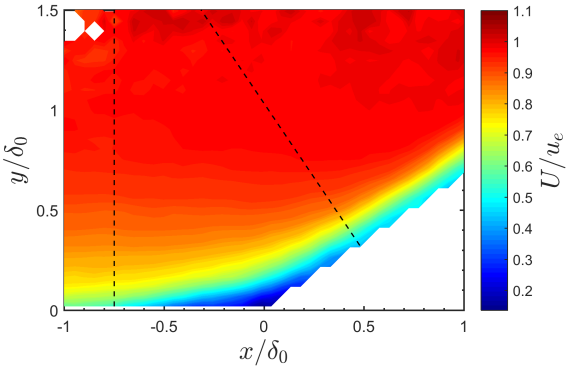

Figure 7.9: Normalized mean velocity magnitude contour plot of the STBLI. A separated region and compression of the boundary layer after the corner is visible. The dashed lines are two examples of the velocity profile locations, for $x/\delta = -0.75$ and $x/\delta = 0.5$, used in Figures 7.10 and 7.11.

Figure 7.10 shows a comparison of mean wall-tangent velocity profiles at x/δ_0 locations upstream of the compression corner. The TBL measurement location presented in Section 7.4 is shown for reference. The profile at the compression corner is wall-normal to the upstream cylinder. There is a broadening on the velocity profiles as the corner is approached. However, the boundary layer height does not change appreciably.

Figure 7.11 shows the mean wall-tangent velocity profiles at x/δ_0 locations downstream of the compression corner. The freestream velocity decreases to around 1,210 m/s. This is consistent with flow through an approximately 40.5° oblique shock wave. The boundary layer thickness progressively decreases to the thinner

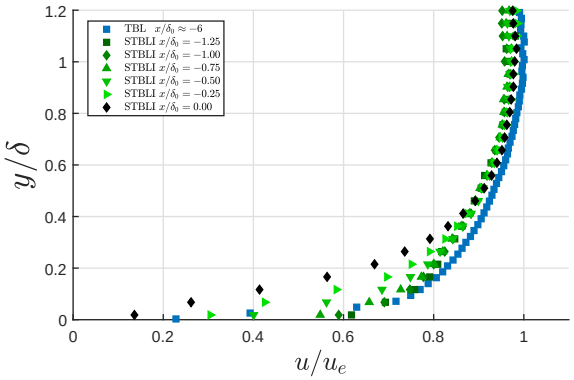

Figure 7.10: STBLI mean wall-tangent velocity profiles at several x/δ locations upstream of the compression corner.

boundary layer height along the ramp surface.

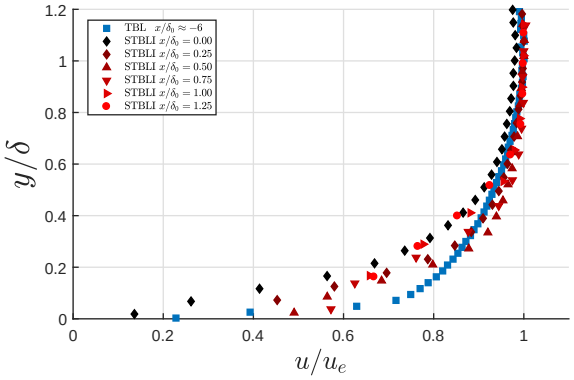

Figure 7.11: STBLI mean wall-tangent velocity profiles at several x/δ locations downstream of the compression corner.

Figure 7.12 shows the wall-tangent fluctuating velocity profiles for the same x/δ_0 locations used for Figure 7.10. The fluctuating velocity near the wall is shown to increase in magnitude as the compression corner is approached. There is also an increase in the overall fluctuating velocity magnitudes compared to the TBL profile particularly near the boundary layer edge. This increase may be due to the reduced number of samples used for the statistics because streamwise averaging is not performed on the STBLI.

Figure 7.13 shows the wall-tangent fluctuating velocity profiles for the same x/δ_0

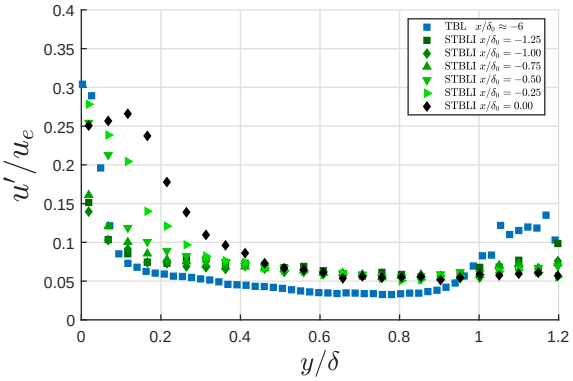

Figure 7.12: STBLI wall-tangent fluctuating velocity profiles at several x/δ locations upstream of the compression corner.

locations used for Figure 7.11. The downstream profiles all exhibit similar behavior as the profile at the compression corner. There is a high level of fluctuations throughout the boundary layer along the ramp.

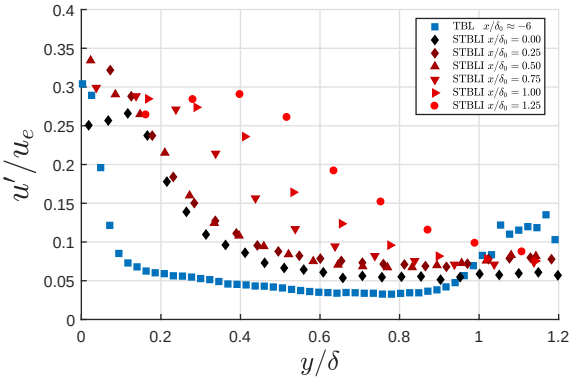

Figure 7.13: STBLI wall-tangent fluctuating velocity profiles at several x/δ locations downstream of the compression corner.

Chapter 8: Conclusions

PIV measurements were performed in a Mach 3 turbulent boundary layer at Reynolds numbers within a range characteristic of DNS calculations and lower than many experiments reported in literature. Multiple reservoir pressures and measurement locations create an overlapping parameter space so that flow parameters are isolated from experimental setup and method. The van Driest transformed inner scaled velocity shows excellent agreement to a ZPG adiabatic turbulent boundary layer data. The post processing spatial resolution (pixels per interrogation window) has a small effect on the fluctuating velocity profiles. However, fluctuating velocity magnitudes increase with camera magnification.

Streamwise fluctuating velocity profiles agree with the literature including low Reynolds number DNS. The wall-normal fluctuating velocity shows a larger variation between experiments compared to the streamwise component. This variation seems to be due to the particle lag. There is a linear variation is found between the measurement error and the Stokes number. This agrees with previous studies that show the wall-normal fluctuating velocity is susceptible to particle lag [38, 61, 50]. The error between the wall-normal component and Klebanoff HWA data [18] is about 10% for $St \approx 0.25$ whereas it exceeds 50% for $St \approx 1$. Energy content at higher wavenumbers

is found to exceed the measurable range of PIV due to the effects of particle lag and spatial resolution acting as low pass filters. The flatter spectrum of the wall-normal fluctuating velocity seems to cause this component to be more susceptible to these effects than the streamwise component. The structure angle of coherent turbulent hairpin structures and the extent of the streamwise spatial correlation agree well with that reported in the literature [29, 81] including the KTV data from Mustafa et al. [26] performed at the same facility.

Local seeding for PIV has been successfully demonstrated to measure Mach 3 and Mach 10 turbulent boundary layers. The seeding injectors introduce particles in the high-speed section of the flow by increasing the injected fluid momentum through a converging/diverging supersonic nozzle exiting tangentially to the wall (model surface for Tunnel 9). Two methods were used to determine the particle concentration throughout the boundary layer, including a new Gaussian elimination method. The measured concentration confirms the qualitative trend of high concentration in the boundary layer which tapers off sharply towards the freestream. All local injector normalized concentration profiles have excellent agreement with CFD. However, the peak measured concentration is larger than CFD by a factor of 3.1, 2.7, and 1.7 for the M3CT Stations 2 and 3, and Tunnel 9, respectively. This agreement is within an acceptable range to continue use for injector nozzle design development.

The local seeding data has good agreement with global seeding for mean velocity and turbulent statistics profiles with a few exceptions. At the freestream, the mean velocity decreases sharply away from the global values. The magnitudes of the turbulent statistics increase sharply at some point in the upper half of the boundary

layer, $y/\delta = 0.6$, 0.9, and 0.8 for Tunnel 9, and the M3CT Stations 2 and 3, respectively. This is attributed to the effects of particle biasing. The distribution of particles within the boundary layer, namely the lack of particles in the freestream, skew the velocity probability density functions to artificially increase the turbulent statistics. The location of this deviation in turbulence statistics may be indicated by the sharp drop-off in the valid velocity vectors by DaVis and the increased erratic behavior of the skewness.

PIV has been used for the first time at Mach 10 to measure the velocity in a turbulent boundary layer and shock turbulent boundary layer interaction generated by a large hollow cylinder flare test article at Tunnel 9 at a freestream unit Reynolds number of $16 \times 10^6/m$. The large size of the HCF creates a thick, 25.8 mm boundary layer 1.83 m downstream of the leading edge with a momentum thickness Reynolds number of 11,600. To provide seeding for the large-scale model, a local particle seeding system is used which features a supersonic converging/diverging nozzle located in the leading edge of the model. The injector accelerates the aerosol to minimize flow disturbance. Turbulent mixing disperses the particles for a high relatively uniform image density for $y/\delta < 0.6$. Mean streamwise velocity shows good adherence to the log law with similar constants to a ZPG boundary layer $\kappa = 0.4$ and $C = 5.1$. Streamwise velocity fluctuations agreed well with the literature for the majority of the boundary layer. Above $y/\delta = 0.6$ the fluctuations are artificially increased due to particle biasing. The STBLI exhibits expected behavior of a TBL upstream of the interaction, a separated region at the corner and thinning of the boundary layer downstream of the interaction. The separated region is smaller than expected,

possibly attributed to 3-D effects of the axisymmetric geometry. The freestream velocity downstream of the interaction is consistent with flow through a 40.5° oblique shock.

Chapter 9: Recommended Future Studies

The present research has demonstrated PIV as a viable measurement technique for Tunnel 9. However, this is a starting point from which the measurement should be refined. There are several studies which may be conducted in order to increase the amount of data measured and better characterize the particle response.

Only one Mach 10 high-speed local injector profile was tested. The data show that the particles did not disperse far enough into the boundary layer for reliable measurements above $y/\delta = 0.6$. New injector profiles should be developed in order to increase particle concentration at the boundary layer edge and improve particle concentration uniformity. With the current design of the HCF test article, nozzle profiles are easily interchanged. Experiments in this dissertation have shown that CFD may be used to develop new nozzle profiles with an order of magnitude accuracy. Further, new injector profiles may be manufactured at relatively low cost. Two injectors are manufactured for roughly the cost of one day of test occupation in Tunnel 9.

Accurate particle concentration measurements are crucial to the future development of high-speed local injector nozzle profiles. The particle concentration in the measurement section must be accurately represented by the CFD codes used to de-

sign the local injectors. The particle concentration measurements using the current techniques (thresholding and Gaussian elimination) have excellent agreement to the CFD codes when the data are normalized. However, the dimensional agreement may be improved. Several factors were identified which could contribute to this disparity.

The laser sheet thickness was measured by a using burn pattern. There exists some ambiguity as to if this is the sheet thickness which should be used for determining the particle concentration. A better characterization of the laser sheet may be done by using a beam profiler to determine the distribution of light intensity across the sheet thickness (assumed to be Gaussian). In addition, the particle concentration from the atomizer is assumed to be accurate to the published values in the product literature. Further, I have assumed that particle concentration loss along the supply tubing is minimal. The particle concentration at the local injector plenum was not measured. The uncertainty in the measurement section particle concentration may be greatly reduced if this concentration is measured.

The oblique shock wave analysis used to determine the particle diameter may be improved. First, the study can be extended to include two ramp angles (8° and 16°). This way the particle density and diameter can be determined simultaneously by solving Eq. 4.13 simultaneously for the two cases using an Euler scheme as shown by Williams et al. [75]. Second, the PIV experimental setup may be optimized to only analyze the shock response. The FOV for the study used also included the STBLI region at the ramp corner. This caused the FOV for the shock to be sub-optimal. Also, the ramp may be re-manufactured to improve the flowfield. The

ramps manufactured are too small for this boundary layer. The ramp height was on the order of the boundary layer thickness.

The particle diameter may be measured directly by using an instrument such as a scanning mobility particle sizer. This would measure the diameter of the particles directly at the atomizer outlet. This measurement should be used in conjunction with the shock wave test to verify if the effective diameter of the oil particles vary in the flow. The particle diameter can be thoroughly characterized with this measurement and a comparison of the particle diameters determined from the oblique shock test using Eqs. 4.3 and 4.13.

There is a limit to particle response time which may be achieved using oil droplets or solid oxide particles (TiO_2 or Al_2O_3). Nanoparticles have much shorter particle response times and may become a viable alternative to conventional oil and solid oxide particles for PIV. Schwyn et al. [86] introduced a mature method of nanoparticle generation where a spark discharge generator (SDG) was used to generate gold particles in a nitrogen carrier gas. These nanoparticles consisted of small, <10nm primary particles made of electrode material agglomerated to form fractal strings of large optical diameter but low density as much of the volume is composed of the carrier gas. Schwyn et al. determined that this type of generator can be used with any conducting electrodes. Tabrizi et al. [87] investigated effects of varied parameters of a similar SDG design, in particular comparing size and concentration values of gold particles using nitrogen and argon as carrier gas. Ghaemi et al [11] used Al_2O_3 particles as seeding particles in a supersonic ramp configuration to compare nanoparticle response time against theoretical. These researchers found the parti-

cle response time of the nanoparticle response time was an order of magnitude less than the compact agglomerate response time. One complication could be the low concentration output of market available SDG.

My development of PIV at Tunnel 9 occurred simultaneously with two other velocimetry methods: krypton tagging velocimetry (KTV) [25] and femtosecond laser electronic excitation tagging (FLEET)[88]. Both of these techniques are molecular tagging velocimetry (MTV) methods. The velocity is measured by imaging the fluorescence of electrically excited molecules. In contrast, PIV images Mie scattering of particles entrained in the flow. MTV and PIV are both touted as non-intrusive measurement techniques. While less intrusive than traditional measurements of Pitot probes and hot wire anemometry probes, MTV and PIV are not truly non-intrusive. PIV requires the introduction of nanoparticles in the flow. KTV requires the introduction of krypton gas which is generally heavier than the working fluid. KTV and FLEET both add a large amount of excitation energy to the flow. The elimination of the need to introduce high-inertia particles seems to give MTV a clear advantage over PIV. However, all three techniques have a place in Tunnel 9.

PIV has the advantage of easily obtaining two-component velocity measurements. Measuring two-components of velocity allows for more data points for comparison with numerical solutions as well as allows for the determination of Reynolds shear stresses. Two component-velocity may be extended to three-component through the development of stereo-PIV. Further, each measurement location is spatially correlated with high spatial resolution. This snapshot of velocity gives further insight into the flow physics. This allows for the determination of parameters beyond mean

and fluctuating velocity. Turbulent structures may be identified through the spatial correlation coefficient. Also, the distribution of turbulent kinetic energy in relation to the disturbance size may be determined from the calculation of a power spectra density. These advantages come at the cost of a complex seeding delivery system. The atomizer plumbing to the sting may be retained for future model testing. However, each new model requires a unique injector because the injector is integral to the model. The difficulty of seeding injection may be alleviated by global seeding or subsonic nozzle injection. These two methods were initially ruled out for the application of PIV at Tunnel 9 based on particle concentration limitations of traditional generation methods. Global seeding or subsonic nozzle injection may be revisited if a method to generation high concentration of particles is developed. A solution may come in the form of a solid mass which ablates particles into the flow. Or, perhaps an inert gas may be injected which condenses or deposits in the freestream to form particles suitable for the use in PIV. However, many models may be easily converted to incorporate a local seeding injector block to more quickly implement PIV in future test series.

The MTV techniques used at Tunnel 9 require significantly less infrastructure to provide the tracer molecules. KTV injects a relatively small amount (1%) of krypton gas into the reservoir prior to the run. FLEET uses nitrogen gas as the tracer molecule which is the working fluid of Tunnel 9. Also, a line written by these techniques is able to be read multiple times in order to get streamwise spatial correlation. However, MTV is primarily a single component velocity measurement technique. Two-component velocity measurements require a cross to be written in

the molecules. This limits the wall-normal spatial resolution of wall-normal velocity to the number of lines written into the flow. Although, a single component velocity measurement is still extremely useful, particularly in the validation of numerical techniques.

The flowfield of study may play a large role in determining the most valuable measurement technique. MTV techniques may be used for flows with one dominant velocity component, such as a turbulent boundary layer. Further, MTV is well-suited for flows where the particle response is unacceptably high, perhaps for more rarefied flows such as Mach 18+. In contrast, PIV is useful in flows with highly two or three dimensionality or even flow reversal such as a STBLI. However, certain flows with recirculation areas become difficult to seed for PIV. Beresh et al. [89] showed that the low seeding concentration in the flow behind a wall-mounted hemisphere at Mach 2.0 rendered certain areas in the wake unmeasurable with PIV. In such cases FLEET has a unique advantage in Tunnel 9 as the tracking molecules will be present in all flow areas. PIV and KTV may have interesting applications in flows with transpiration. With these techniques there are options to seed the entire flow, only the transpiration flow, or only the core flow. New insights may be gained by only seeding one flow in a mixing flowfield.

Chapter 10: Publications

10.1 Journal Articles

1. Brooks, J.M., Gupta, A.K., Smith, M.S., and Marineau E.C. Particle image velocimetry measurements of Mach 3 turbulent boundary layers at low Reynolds numbers *Experiments in Fluids* 59: 83, 2018 https://doi.org/10.1007/s00348-018-2536-x

2. Brooks, J.M., Gupta, A.K., Smith, M.S., Marineau E.C. and Tatum K. High-Speed Local Particle Injection for Particle Image Velocimetry *Submitted to AIAA Journal*

3. Brooks, J.M., Gupta, A.K., Smith, M.S., and Marineau E.C. Mach 10 PIV Flow Field Measurements of a Turbulent Boundary Layer and Shock Turbulent Boundary Layer Interaction *Submitted to AIAA Journal*

10.2 Conference Papers

1. Brooks, J.M., Gupta, A.K., Helm, C., Martin, M.P., Smith, M.S., and Marineau E.C. Mach 10 PIV Flow Field Measurements of a Turbulent Boundary Layer and Shock Turbulent Boundary Layer Interaction. In *33rd AIAA Aerodynamic*

Measurement Technology and Ground Testing Conference, Denver, Colorado, USA, 2017. AIAA 2017-3325.

2. Brooks, J.M., Gupta, A.K., Smith, M.S., and Marineau E.C. PIV Measurements of Mach 2.7 Turbulent Boundary Layer with varying Reynolds Numbers. In *54th AIAA Aerospace Sciences Meeting*, San Diego, California, USA, 2016. AIAA 2016-1147.

3. Brooks, J.M., Gupta, A.K., Smith, M.S., and Marineau E.C. Development of Particle Image Velocimetry in a Mach 2.7 Wind Tunnel at AEDC White Oak. In *53rd Aerospace Sciences Meeting*, Kissimmee, Florida, USA, 2015. AIAA 2015-1915.

4. Brooks, J.M., Gupta, A.K., Smith, M.S., and Marineau E.C. Development of Non-Intrusive Velocity Measurement Capabilities at AEDC Tunnel 9. In *52nd AIAA Aerospace Sciences Meeting*, National Har- bor, Maryland, USA, 2014. AIAA 2014-1239.

Bibliography

[1] Ronald J. Adrian and Chung-Sheng Yao. Pulsed laser technique application to liquid and gaseous flows and the scattering power of seed materials. *Appl. Opt.*, 24(1):44–52, Jan 1985.

[2] John F Lafferty, Joseph J Coblish, Eric Marineau, Joseph D Norris, Inna Kurtis, Daniel R Lewis, Michael Smith, and Michael Marana. The Hypervelocity Wind Tunnel No. 9; Continued Excellence Through Improvement and Modernization. In *53rd Aerospace Sciences Meeting*, Kissimmee, Florida, USA, 2015. AIAA 2015-1340.

[3] F. F J Schrijer, F. Scarano, and B. W. Van Oudheusden. Application of PIV in a Mach 7 double-ramp flow. *Experiments in Fluids*, 41(2):353–363, 2006.

[4] Owen J Williams and Alexander J Smits. Application of PIV to the Measurement of Hypersonic Turbulence. In *16th Int Symp on Apllications of Laser . . .*, Lisbon, Protugal, 2012.

[5] Anne-Marie Schreyer, Dipankar Sahoo, and Alexander J Smits. Experimental Investigations of a Hypersonic Shock Turbulent Boundary Layer Interaction. In *49th AIAA Aerospace Sciences Meeting including the New Horizons Forum and Aerospace Exposition*, Orlando, Florida, USA, 2011. AIAA 2011-0481.

[6] Dipankar Sahoo, Matthew J Ringuette, and Alexander J Smits. Experimental Investigation of a Hypersonic Turbulent Boundary Layer. In *47th AIAA Aerospace Sciences Meeting Including The New Horizons Forum and Aerospace Exposition*, Orlando, Florida, USA, 2009. AIAA 2009-0780.

[7] Dipankar Sahoo, Michael Papageorge, and Alexander J Smits. PIV Experiments on a Rough-wall Hypersonic Turbulent Boundary Layer. In *40th AIAA Fluid Dynamics Conference*, Chicago, Illinois, USA, 2010. AIAA 2010-4471.

[8] Nathan R Tichenor, Raymond A. Humble, and Rodney D. W. Bowersox. Influence of Favorable Pressure Gradients on a Mach 5 . 0 Turbulent Boundary

Layer. In *49th AIAA Aerospace Sciences Meeting including the New Horizons Forum and Aerospace Exposition*, Orlando, Florida, USA, 2011. AIAA 2011-0748.

[9] Nathan Ryan Tichenor. *Characterization of the Influence of a Favorable Pressure Gradient on the Basic Structure of a Mach 5 . 0 High Reynolds Number Supersonic Turbulent Boundary Layer Characterization of the Influence of a Favorable Pressure Gradient on the Basic Structure of.* Doctor of philosophy, Texas A&M University, 2010.

[10] J L Wagner, K B Yuceil, N T Clemens, and Reynolds Number. PIV Measurements of Unstart of an Inlet-Isolator Model in a Mach 5 Flow. In *39th AIAA Fluid Dynamics Conference*, San Antonio, Texas, USA, 2009. AIAA 2009-4209.

[11] S Ghaemi and F Scarano. Nanostructured tracers for laser-based diagnostics in high-speed flows. *Meas. Sci. Technol.*, 105403, 2010.

[12] S. Pirozzoli and M. Bernardini. Turbulence in supersonic boundary layers at moderate Reynolds number. *Journal of Fluid Mechanics*, 688(2011):120–168, 2011.

[13] Sergio Pirozzoli and Matteo Bernardini. Probing high-Reynolds-number effects in numerical boundary layers. *Physics of Fluids*, 021704(25):1–7, 2013.

[14] H. H. Fernholz and P. J. Finley. A Critical Commentary on Mean Flow Data for Two-Dimensional Compressible Turbulent Boundary Layers. Technical Report AGARDograph No. 253, Advisory Group for Aerospace Research and Development, Neuilly sur Seine, 1980.

[15] Donald Coles. The law of the wake in the turbulent boundary layer. *Journal of Fluid Mechanics*, 1:191–226, 1956.

[16] E. R. van Driest. Turbulent Boundary Layer in Compressible Fluids. *Journal of Aeronautical Sciences*, 18(3):145–160, 1951.

[17] A. A. Townsend. The structure of the turbulent boundary layer. *Mathematical Proceedings of the Cambridge Philosophical Society*, 47:375–395, 1951.

[18] P. S. Klebanoff. Characteristics of Turbulence in a Boundary Layer with Zero Pressure Gradient. Technical Report NACA-TR-1247, National Advisory Committee for Aeronautics, Springfield, Virginia, USA, 1955.

[19] Isaac W Ekoto, Rodney D W Bowersox, and Larry Goss. Planar Measurements of Supersonic Boundary Layers with Curvature Driven Pressure Gradients. In *45th AIAA Aerospace Sciences Meeting and Exhibit*, Reno, Nevada, USA, 2007. AIAA 2007-1137.

[20] Sebastien Piponniau. *Instationnarites dans les decollements compressibles : cas des couches limites soumises‘ a ondes de choc*. Docteur, Universite de Provence - Aix-Marseille, 2009.

[21] Andrew P. Lapsa and Werner J A Dahm. Stereo particle image velocimetry of nonequilibrium turbulence relaxation in a supersonic boundary layer. *Experiments in Fluids*, 50(1):89–108, 2011.

[22] Max Elena and Jean-Paul LaCharme. Experimental study of a supersonic turbulent boundary layer using a laser Doppler anemometer. *Journal of Theoretical and Applied Mechanics*, 7(2):175–190, 1988.

[23] A. J. Smits, K. Hayakawa, and K. C. Muck. Constant temperature hot-wire anemometer practice in supersonic flows - Part l: The normal wire. *Experiments in Fluids*, 1(2):83–92, 1983.

[24] Alan L. Kistler. Fluctuation Measurements in a Supersonic Turbulent Boundary Layer. *Physics of Fluids*, 2(3):290–296, 1959.

[25] D. Zahradka, N. J. Parziale, M. S. Smith, and E. C. Marineau. Krypton tagging velocimetry in a turbulent Mach 2.7 boundary layer. *Experiments in Fluids*, 57(5):1–14, 2016.

[26] M. A. Mustafa, M. B. Hunt, N. J. Parziale, M. S. Smith, and E. C. Marineau. Krypton Tagging Velocimetry (KTV) Investigation of Shock-Wave / Turbulent Boundary-Layer Interaction. In *55th AIAA Aerospace Sciences Meeting*, Grapevine, Texas, USA, 2017. AIAA 2017-0025.

[27] Owen J. H. Williams, D. Sahoo, M. Baumgartner, and Alexander J. Smits. Experiments on the structure and scaling of hypersonic turbulent boundary layers. *Journal of Fluid Mechanics*, 834:237–270, 2018.

[28] M. Pino Martin. Direct numerical simulation of hypersonic turbulent boundary layers. Part 1. Initialization and comparison with experiments. *Journal of Fluid Mechanics*, 570:347–364, 2007.

[29] L. Duan, I. Beekman, and M.P. Martin. Direct numerical simulation of hypersonic turbulent boundary layers . Part 3 . Effect of Mach number. *J. Fluid Mech.*, 672:245–267, 2011.

[30] F. F. J. Schrijer, F Scarano, B W Van Oudheusden, and W J Bannink. Application of PIV in a Hypersonic Double-Ramp Flow. In *AIAA/CIRA 13th International Space Planes and Hypersonics Systems and Technologies*. AIAA 2005-3331, 2005.

[31] Anne-Marie Schreyer, Dipankar Sahoo, and Alexander J Smits. Turbulence Measurements with PIV in a Hypersonic Shock Boundary Layer Interaction. In *41st AIAA Fluid Dynamics Conference and Exhibit*, Honolulu, Hawaii, 2011. AIAA 2011-3429.

[32] Stephan Priebe and M. Pino Martin. Direct Numerical Simulation of a Hypersonic Turbulent Boundary Layer on a Large Domain. In *41st AIAA Fluid Dynamics Conference and Exhibit*, hon, 2011. AIAA 2011-3432.

[33] N R Tichenor, R A Humble, and R D W Bowersox. Reynolds Stresses in a Hypersonic Boundary Layer with Streamline Curvature - Driven Favorable Pressure Gradients. In *42nd AIAA Fluid Dynamics Conference and Exhibit*, New Orleans, Louisiana, USA, 2012. AIAA 2012-3059.

[34] Scott J Peltier, Raymond A Humble, and Rodney D W Bowersox. The Influence of Favorable Pressure Gradients upon the Coherent Motions in a Mach 5 Turbulent Boundary Layer. In *42nd AIAA Fluid Dynamics Conference and Exhibit*, New Orleans, Louisiana, USA, 2012. AIAA 2012-3060.

[35] F. L. Crosswy. Particle Size Distributions of Several Commonly Used Seeding Aerosols. Technical Report N86-11441, Calspan Corporation/AEDC Division, Arnold Air Force Station, Tennessee, USA, 1985.

[36] D Ragni, F Schrijer, B W Van Oudheusden, and F Scarano. Particle tracer response across shocks measured by PIV. *Experiments in Fluids*, pages 53–64, 2011.

[37] P Dupont, S Piponniau, A Sidorenko, and J F Debiève. Investigation by Particle Image Velocimetry Measurements of Oblique Shock Reflection with Separation. *AIAA Journal*, 46(6):6–11, 2008.

[38] K. Todd. Lowe, Gwibo Byun, and Roger L. Simpson. Supersonic Turbulent Boundary Layer Statistics. In *52nd AIAA Aerospace Sciences Meeting*, National Harbor, Maryland, USA, 2014. AIAA 2014-0233.

[39] C. B. A. Millikan. A critical discussion of turbulent flows in channels and circular tubes. In *Pages 386-392 of: Proceedings of the Fifth International Congress of Applied Mechanics*, 1938.

[40] Alfred Walz. *Boundary Layers of Flow and Temperature*. MIT Press, 1969.

[41] D. B. Spalding. A Single Formula for the Law of the Wall. *Journal of Applied Mechanics*, 28(3):455–458, 1961.

[42] J. E. Lewis, R. L. Gran, and T. Kubota. An experiment on the adiabatic compressible turbulent boundary layer in adverse and favourable pressure gradients. *J. Fluid Mech.*, 51(4):657–672, 1972.

[43] Edward J. Hopkins and Mamoru Inouye. An Evaluation of Theories for Predicting Turbulent Skin Friction and Heat Transfer on Flat Plates at Supersonic and Hypersonic Mach Numbers. *AIAA Journal*, 9(6):993–103, 1971.

[44] Mark V. Morkovin. Effects of compressibility on turbulent flows. In A. J. Favre, editor, *Mecanique de la Turbulence*, pages 367–380. Centre National de la Recherche Scientifique (CNRS), 1962.

[45] A. E. Perry and M. S. Chong. On the mechanism of wall turbulence. *Journal of Fluid Mechanics*, 119:173–217, 1982.

[46] L H Benedict and R D Gould. Towards better uncertainty estimates for turbulence statistics. *Experiments in Fluids*, 22:129–136, 1996.

[47] Hugh W. Coleman and W. Glenn Steele. *Experimentation, Validation, and Uncertainty Analysis for Engineers*. John Wiley & Sons, Inc., Hoboken, New Jersey, USA, 2009.

[48] Alexander J. Smits and Jean-Paul Dussage. *Turbulent Shear Layers in Supersonic Flow*. Springer, New York, New York, USA, 2nd edition, 2006.

[49] Jonathan M Brooks, Ashwani K Gupta, Michael S. Smith, and Eric C. Marineau. Development of Non-Intrusive Velocity Measurement Capabilities at AEDC Tunnel 9. In *52nd AIAA Aerospace Sciences Meeting*, National Harbor, Maryland, USA, 2014. AIAA 2014-1239.

[50] Jonathan M. Brooks, Ashwani K Gupta, Michael S Smith, and Eric C Marineau. Development of Particle Image Velocimetry in a Mach 2.7 Wind Tunnel at AEDC White Oak. In *53rd Aerospace Sciences Meeting*, Kissimmee, Florida, USA, 2015. AIAA 2015-1915.

[51] W.J. Devenport and J.A. Schetz. Boundary layer codes for students in java. In *1998 ASME Fluids Engineering Division Summer Meeting*, Washington, DC, USA, 1998. FEDSM98-5139.

[52] W. J. Devenport, J. A. Schetz, and Yu Wang. Heat Transfer Codes for Students in Java. In *5th ASME/JSME Thermal Engineering Joint Conference*, San Diego, California, USA, 1999. AJTE99-6229.

[53] Wendy I Grosser. Factors Influencing Pitot Probe Centerline Displacement in a Turbulent Supersonic Boundary Layer. Technical Report 107341, National Aeronautics and Space Administration, Cleveland, Ohio, USA, 1997.

[54] J. D. Anderson. *Modern Compressible Flow With Historical Perspective*. McGraw Hill, Boston, Massachusetts, USA, 2003.

[55] H. W. Liepmann and A. Roshko. *Elements of Gasdynamics*. Dover Publications, Inc., Mineola, New York, USA, 2001.

[56] A. Pope and K. L. Goin. *High-Speed Wind Tunnel Testing*. John Wiley & Sons, Inc., New York, New York, USA, 1965.

[57] Integrated Design Tools. *OS10-V3-4K Specification Shee*. Tallahassee, Florida, USA, 2016.

[58] Litron Lasers North America. *Lasers for PIV Applications*. Bozeman, Montana, USA, 2010.

[59] Integrated Design Tools. *Y7-S1 Specification Sheet*. Tallahassee, Florida, USA, 2018.

[60] New Wave Research, Inc. *Gemini PIV Nd:YAG Laser Systems*. Fremont, California, USA, 2003.

[61] Owen J H Williams. *Density effects on turbulent boundary layer structure: from the atmosphere to hypersonic flow*. Doctoral dissertation, Princeton University, 2014.

[62] Daniel R. Cadel, Dongyun Shin, and K. Todd Lowe. A Hybrid Technique for Laser Flare Reduction. In *54th AIAA Aerospace Sciences Meeting*, San Diego, California, USA, 2016. AIAA 2016-0788.

[63] Hugh R. Carlon and Mark A. Guelta. SAFE REPLACEMENT MATERIALS FOR DOP IN "HOT SMOKE" AEROSOL PENETROMETER MACHINES. In *Chemical Research, Development & Engineering Center*, Aberdeen, Maryland, USA, 1992. CRDEC-TR-333.

[64] Marcus Casper, Soren Stephan, Jan Windte, Peter Scholz, Rolf Radespiel, Sven Scharnowski, and Christian J. Kahler. Hypersonic PIV in a Ludwieg Tube Wind Tunnel at Mach 5.9. In *28th Aerodynamic Measurement Technology, Ground Testing, and Flight Testing Conference*, New Orleans, Louisiana, USA, 2012. AIAA 2012-3197.

[65] D. Torres and M. Trujillo. KIVA-4: An unstructured ALE code for compressible gas flow with sprays. *J. Computational Physics*, 219:943–975, 2006.

[66] N. J et al. Georgiadis. Wind-US Code Physical Modeling Improvements to Complement Hypersonic Testing and Evaluation. In *47th AIAA Aerospace Sciences*, Orlando, Florida, USA, 2009. AIAA 2009-0193.

[67] J. E. Kersey. *Simulation of Shock Attenuation by Particles and Droplets*. Master of science, Illinois at Urbana-Champaign, 2007.

[68] E. Loth and V. Lee. Local Adaptive Timestepping for Lagrangian Particle Tracking. In *45th AIAA Aerospace Sciences Meeting and Exhibit*, Reno, Nevada, USA, 2007. AIAA 2007-0335.

[69] R. B. Bond, R. H. Nichols, and G. D. Power. Extension of Kestrel to General Thermochemical Models, Part I. In *46th AIAA Thermophysics Conference*, Washington, District of Columbia, USA, 2016. AIAA 2016-4435.

[70] S.A. Morton and R. L. Meakin. HPCMP CREATETM-AV Kestrel Architecture, Capabilities, and Long Term Plan for Fixed-Wing Aircraft Simulations. In *54th AIAA Aerospace Sciences Meeting*, San Diego, California, USA, 2016. AIAA 2016-0565.

[71] R. J. Adrian and J. Westerweel. *Particle Image Velocimetry*. Cambridge University Press, New York, 2011.

[72] E Loth and I Introduction. Compressibility and Rarefaction Effects on Drag of a Spherical Particle. *AIAA Journal*, 46(9):2219–2228, 2008.

[73] K. Samimy and S. K. Lele. Motion of particles with inertia in a compressible. *Physics of Fluids A: Fluid Dynamics*, 3(8):1915–1923, 1991.

[74] A. Melling. Tracer particles and seeding for particle image velocimetry. *Measurement Science and Technology*, 8:1406–1416, 1997.

[75] Owen J. H. Williams, Tue Nguyen, Anne-Marie Schreyer, and Alexander J. Smits. Particle response analysis for particle image velocimetry in supersonic flows. *Physics of Fluids*, 27:076101, 2015.

[76] D.E. Coles. The Turbulent Boundary Layer in a Compressible Fluid. Technical Report R–403–PR, The Rand Corporation, Santa Monica, California, 1962.

[77] H. H. Fernholz and P. J. Finley. A Further Compilation of Compressible Boundary Layer Data with a Survey of Turbulence Data. Technical Report AGARDograph No. 263, Advisory Group for Aerospace Research and Development, Neuilly sur Seine, 1981.

[78] Frank M. White. *Viscous Fluid Flow*. McGraw-Hill, Inc., New York, 1974.

[79] R Mei. Velocity fidelity of flow tracer particles. *Experiments in Fluids*, 22:1–13, 1996.

[80] G. I. Taylor. The spectrum of turbulence. *Proceedings of the Royal Society of London, Series A, Mathematical and Physical Sciences*, 164(919):476–490, 1937.

[81] Scott Peltier, Raymond A. Humble, and Rodney D. W. Bowersox. PIV of a Mach 5 Turbulent Boundary Layer over Diamond Roughness Elements. In *42nd AIAA Fluid Dynamics Conference and Exhibit*, New Orleans, Louisiana, USA, 2012. AIAA 2012-3061.

[82] R. A. Antonia. Some small scale properties of boundary layer turbulence. *The Physics of Fluids*, 16(8):1198–1206, 1973.

[83] L. Duan, I. Beekman, and M. P. Martin. Direct numerical simulation of hypersonic turbulent boundary layers. Part 2. Effect of wall temperature. *J. Fluid Mech.*, 655:419–445, 2010.

[84] Jonathan M. Brooks, Ashwani K Gupta, Michael S Smith, Eric C Marineau, and Kenneth Tatum. High-Speed Local Particle Injection for Particle Image Velocimetry. Unpubished Manuscipt, 2018.

[85] Clara Helm and M Pino Martin. New LES of a Hypersonic Shock / Turbulent Boundary Layer Interaction. In *54th AIAA Aerospace Sciences Meeting*, San Diego, California, USA, 2016. AIAA 2016-0346.

[86] S. Schwyn, E. Garwin, and A. Schmidt-Ott. Aerosol Generation by Spark Discharge. *Journal of Aerosol Science*, 19(5):639–642, 1988.

[87] N.S. Tabrizi, M. Ullman, V.A. Vons, U Lafont, and A. Schmitt-Ott. Generation of nanoparticles by spark discharge. *Journal of Nanoparticle Research*, (11):315–332.

[88] Laura E. Dogariu, Arthur Dogariu, Richard B. Miles, Mike S. Smith, and Eric C. Marineau. Non-intrusive Hypersonic Freestream and Turbulent Boundary-Layer Velocity Measurements in AEDC Tunnel 9 using FLEET. In *2018 AIAA Aerospace Sciences Meeting*, Kissimmee, Florida, USA, 2018. AIAA 2018-1769.

[89] Steven J. Beresh, John F. Henfling, and Russell W. Spillers. Pulse-Burst PIV of the Supersonic Wake of a Wall-Mounted Hemisphere. In *47th AIAA Fluid Dynamics Conference*, Denver, Colorado, USA, 2017. AIAA 2017-3119.